

ABSTRACT

LONG, QIAN. Hierarchical Approaches for Coordinating Distribution-Level Control with Smart Inverters and Microgrids. (Under the direction of David Lubkeman).

With the high penetration of distributed energy resources (DERs) and microgrids in distribution systems, the paradigm of voltage control needs to be reconsidered. The intermittency of the DERs results in more frequent and larger voltage variations, which are beyond the capability of conventional voltage control schemes using distribution-level control devices, such as switched capacitors (SCs), on-load tap changers (OLTCs) and step voltage regulators (SVRs). As DERs bring new challenges to voltage control of distribution systems, they also provide opportunities to address voltage issues. Most of the DERs, such as photovoltaic (PV) systems and energy storage systems (ESS), have the potential of mitigating the impact of voltage fluctuations through power electronics interfaces (i.e. smart inverters), at a fast and high granular level. The features of using DERs for voltage control also apply to microgrids, which are control clusters of DERs. Based on the local inverter Volt-Var control specified by the IEEE 1547-2018 standard, this research focuses on the design of a hierarchical voltage control framework that includes multiple levels of control and optimization.

The dissertation first discusses the primary control at the component level and presents a new hybrid algorithm for model parameterization of microgrid components. The model parameterization method guarantees the model fidelity, which is critical to the study of control interactions between multiple DERs in microgrids and distribution systems. This algorithm is developed using a heuristic-based global search algorithm and an optimization-based local algorithm and proves its effectiveness given limited field measurements from simple field tests.

This method forms the modeling basis for investigating the secondary control and the tertiary control that are explored further in this dissertation.

Following the discussion of modeling, a secondary control strategy is designed for microgrids. This secondary controller allows the microgrid to automatically regulate reactive power support and respond to voltage disturbances similar to a smart inverter with the local Volt-Var control. Meanwhile, reactive power sharing is guaranteed among the DERs in the microgrid zone. The proposed controller is a distributed control that is added on top of the primary control of each microgrid component. It can be applied to multi-microgrid architecture and the transient performance is evaluated using a two-microgrid case study.

The dissertation also presents the tertiary control level, which is a Volt-Var optimization model that optimally coordinates utility control devices that are acting in a larger time interval, such as SCs, OLTCs and SVRs, with fast-responding smart inverters. The problem is initially formulated as mixed-integer nonconvex programming and eventually transformed into a sequence of mixed-integer linear programming via a successive linearization technique. The stochastic framework of this Volt-Var optimization that considers the uncertainty of solar irradiance is also developed in this study.

© Copyright 2020 by Qian Long

All Rights Reserve

Hierarchical Approaches for Coordinating Distribution-Level Control with Smart Inverters
and Microgrids

by
Qian Long

A Dissertation submitted to the Graduate Faculty of
North Carolina State University
in partial fulfillment of the
requirements for the degree of
Doctor of Philosophy

Electrical Engineering

Raleigh, North Carolina
2020

APPROVED BY:

Dr. David Lubkeman
Committee Chair

Dr. Ning Lu

Dr. Srdjan Lukic

Dr. Yunan Liu

DEDICATION

To my parents, Zhongping Kuang and Jianjun Long

To my grandparents, Yumei Liu and Jihong Kuang

BIOGRAPHY

Qian Long was born in Jingzhou, Hubei Province, China. He received his B.S. degree in Electrical Engineering and Automation from China Agricultural University, Beijing, China, in 2014 and his M.S. degree in Electrical Engineering from North Carolina State University, Raleigh, NC, USA in 2016. He is currently pursuing the Ph.D. degree in the Department of Electrical and Computer Engineering at North Carolina State University, Raleigh, USA. His research interests are in the areas of modeling, operation, control and optimization of hybrid energy systems.

ACKNOWLEDGMENTS

I have been grateful throughout this journey because there is so much support and help I have received from such great people. My sincerest gratitude firstly goes to my advisor Dr. Lubkeman, who has constantly guided me with great patience and unconditional support for the past five years. He has kept showing me the richness and the depth of power engineering, and through every discussion, he truly inspires me to maintain curiosity and motivation for the research. I appreciate his significant investment in helping me grow as a professional in the power and energy industry. I'm also very grateful to work with Dr. Ning Lu and to receive many of her guidance during my doctoral study. She has offered me generously invaluable suggestions and opportunities, and I have so much respect for her genuine care for the students. I also thank Dr. Srdjan Lukic and Dr. Yunan Liu for their service on my doctoral committee and their insightful comments on my research.

I want to thank all my friends and colleagues at FREEDM Systems Center. It is a great fortune to work with these talented and hard-working researchers, and I appreciate their advice and support in this journey. I can not ask for a better working environment like that.

Last but not least, I would like to thank my family for their love and support. Especially, I'm thankful to my wife Shengnan Li for her love and sacrifice, to my grandparents Yumei Liu and Jihong Kuang for taking good care of me during my childhood, and to my parents Zhongping Kuang and Jianjun Long for always standing beside me.

TABLE OF CONTENTS

LIST OF TABLES	ix
LIST OF FIGURES	x
LIST OF ABBREVIATIONS	xiii
Chapter 1. Introduction	1
1.1 Overview of Voltage Control in Distribution Systems.....	3
1.2 Hierarchical Voltage Control for Microgrids and Distribution Systems	6
1.2.1 Primary Control Level	6
1.2.2 Secondary Control Level	16
1.2.3 Tertiary Control Level	17
1.3 Proposed Hierarchical Approaches.....	20
Chapter 2. Model Parameterization for Microgrid Simulation Using Hybrid Box-Constrained Levenberg-Marquardt Algorithm	23
2.1 Literature Review.....	23
2.2 Modeling Methodologies	26
2.2.1 Diesel Generator Model.....	26
2.2.2 Model Parameters	28
2.3 Diesel Generator Model Parameterization Problem Formulation	29
2.3.1 Problem Formulation	29

2.3.2 Nonlinear Least Squares for Dynamic Systems.....	31
2.4 Hybrid Box-Constrained Levenberg-Marquardt Algorithm.....	33
2.4.1 Levenberg-Marquardt Algorithm.....	33
2.4.2 Box-Constrained Levenberg-Marquardt Algorithm	34
2.4.3 Heuristic Algorithm for Initial Solution Search.....	36
2.4.4 Overview of Model Parameterization Method	37
2.5 Case Studies	39
2.5.1 Benchmark Case	39
2.5.2 Model Parameterization for a Small Diesel Generator	42
2.6 Conclusion	45
 Chapter 3. A New Distributed Voltage Controller for Enabling Volt-Var Support of Microgrids in Grid-Connected Operation.....	
3.1 Literature Review.....	46
3.2 Secondary Voltage Controller Design	48
3.2.1 Proportional Voltage Controller Design	48
3.2.2 Distributed Implementation of Proportional Voltage Control	51
3.3 Small Signal Analysis.....	53
3.4 Simulation Results	57
3.4.1 Voltage Regulation and Reactive Power Sharing.....	58
3.4.2 Comparison with Unity Power Factor Control	60

3.4.2 The Impact of Control Gains on Dynamic Performance	61
3.5 Conclusions.....	62
Chapter 4. Volt-Var Optimization of Distribution Systems for Coordinating	
Utility Voltage Control with Smart Inverters	63
4.1 Literature Review.....	63
4.2 Voltage-Load Sensitivity Matrix	66
4.3 Optimization Model.....	70
4.3.1. Problem Formulation	70
4.3.2. Successive Linear Programming.....	73
4.4 Simulation Results	74
4.5 Conclusions.....	79
Chapter 5. Stochastic Volt-Var Optimization for Coordinating Distribution-Level	
Control with Smart Inverters	80
5.1 Literature Review.....	80
5.2 Forecast Error Characterization	82
5.2.1. Stochastic Modeling for Forecast Errors	82
5.2.2. Scenario Reduction.....	84
5.3 Stochastic Volt-Var Optimization Model.....	86
5.4 Case Studies	89
5.5 Conclusion	94

Chapter 6. Summary and Future Work.....	95
6.1 Summary of Current Work	95
6.2 Future Work Proposal.....	96
REFERENCES.....	97

LIST OF TABLES

Table 1.1. Voltage and reactive/active power control function requirements for DER normal operating performance categories [5].....	14
Table 2.1. Diesel generator model parameters.....	29
Table 2.2. Diesel generator benchmark model parameters and test results	40
Table 2.3. Extracted parameters of diesel generator model.....	45
Table 3.1. Control parameters.....	56
Table 3.2. Test system parameters	58
Table 4.1. Summary of daily voltage ranges	78
Table 4.2. Volt-Var curve slope settings (unit: Q p.u./V p.u.).....	78
Table 4.3. Number of tap operations	78
Table 5.1. Discrete distribution for solar irradiance forecast error.....	90
Table 5.2. Capacitor switching number for all cases	93
Table 5.3. Objective cost comparison.....	94

LIST OF FIGURES

Figure 1.1. An example voltage profile with 30% PHEVs compared to 0% PHEV [2]	2
Figure 1.2. An example distribution feeder with SCs and substation OLTCs from Pullman, WA [6]	3
Figure 1.3. The control structure of three-phase grid-supporting power converters under CCM	9
Figure 1.4. The control structure of three-phase grid-supporting power converters under VCM	12
Figure 1.5. Equivalent circuit of power converter connecting to a distribution network	12
Figure 1.6. An example of Volt-Var characteristics [5]	15
Figure 1.7. An example of active power-reactive power characteristics [5]	15
Figure 1.8. An example of secondary control for islanded microgrids	16
Figure 1.9. An example of ADMS architecture [33]	18
Figure 1.10. An example of a DMS-based model-driven VVO solution [33]	19
Figure 1.11. A general architecture of DERMS [33]	20
Figure 1.12. The architecture of the proposed hierarchical voltage control framework	22
Figure 2.1. Diesel engine model diagram	27
Figure 2.2. Excitation system model diagram	27
Figure 2.3. Synchronous generator model one-line diagram	28
Figure 2.4. Schematic of the proposed model parameterization method	38
Figure 2.5. Diesel engine parameter convergence in Case 4	41
Figure 2.6. Excitation system parameter convergence in Case 4	41
Figure 2.7. Synchronous generator parameter convergence in Case 4	42

Figure 2.8. Optimal fit for load step-up test.....	44
Figure 2.9. Optimal fit for load step-down test.....	44
Figure 3.1. Radial distribution feeder with interconnection of microgrids.....	48
Figure 3.2. Schematic of DPVC control architecture	53
Figure 3.3. Eigenvalue traces of closed-loop systems with the increment of control parameters	56
Figure 3.4. Eigenvalues of closed-loop systems with different time constants of reactive power control loops	56
Figure 3.5. (a) Microgrid PCC voltage magnitude with and without control (b) Ratio of reactive power output to available reactive power capacity	60
Figure 3.6. Comparison of voltage profiles for a cloud cover transient event.....	61
Figure 3.7. (a) MG1 PCC voltage magnitude (b) MG1 ESS reactive power output	61
Figure 4.1. A typical Volt-Var curve of a smart inverter.....	67
Figure 4.2. A simplified example of a 4-bus distribution system.....	67
Figure 4.3. Circuit diagram of the 47-bus distribution feeder	75
Figure 4.4. Three-day load profile and PV irradiance profile in p.u.	77
Figure 4.5. Three-day profile of min/max voltage in the system.....	77
Figure 4.6. Three-day schedule of the OLTC tap position	78
Figure 5.1. Solar irradiance forecast error	83
Figure 5.2. Sampled scenario set (green) and reduced scenario set (orange).....	84
Figure 5.3. Circuit diagram of the 47-bus distribution feeder	90
Figure 5.4. Normalized substation load profile: real power (blue) and reactive power (orange).....	90

Figure 5.5. Voltage profile at bus 1 and bus 23 in Case 1	91
Figure 5.6. Tap operation schedule in Case 1	92

LIST OF ABBREVIATIONS

ADMS	Advanced Distribution Management Systems
AMI	Advanced Metering Infrastructure
CCM	Current-Controlled Mode
CVR	Conservation Voltage Reduction
DER	Distributed Energy Resources
DERMS	Distributed Energy Resource Management Systems
DMS	Distribution Management Systems
DSO	Distribution System Operator
ESS	Energy Storage Systems
EV	Electric Vehicles
FLISR	Fault Location, Isolation and Service Restoration
GIS	Geographical Information Systems
HIL	Hardware-in-the-Loop
OLTC	On-Load Tap Changers
OMS	Outage Management Systems
PCC	Point of Common Coupling
PLL	Phase-Locked Loop
PV	Photovoltaic
SC	Switched Capacitors
SCADA	Supervisory Control and Data Acquisition
SOC	State of Charge
SVR	Step Voltage Regulators

VCM	Voltage-Controlled Mode
VLSM	Voltage-Load Sensitivity Matrix
VVO	Volt-Var Optimization

CHAPTER 1. INTRODUCTION

The primary service voltage of distribution systems should always be maintained at any location within the range of $\pm 5\%$ of the nominal value, which is specified by the ANSI C84.1 standard [1]. As the load level increases at distribution circuits, the systems may experience undervoltage issues without proper voltage regulation, especially at the furthest location from the substation. Most of the utilities regulate voltages in distribution systems utilizing OLTCs and SCs given the predicted load demand. Since the load demand change was low and could be forecasted with sufficient accuracy, these incremental control actions, which are small and slow, were able to keep the service voltage within an acceptable range.

An increasing adoption of EVs and DERs in distribution systems poses new challenges to the conventional voltage control framework. The intermittency and the uncertainty of renewables cause rapid fluctuations of circuit voltages [2]-[3]. Figure 1.1 presents an example of voltage fluctuation caused by higher penetration of PHEV. Besides, for distribution systems with high penetration of PV, there are potential overvoltage issues at PCC during light-load high-PV conditions. However, there are also researches pointing out that the DERs can mitigate voltage flicker and fast voltage fluctuations, providing benefits to the grid by deploying advanced control systems [4]. The recently released IEEE 1547-2018 [5] standard also specifies the DERs should be capable of providing voltage regulation for the main grid by changing reactive power output.

The advantage of having DERs participate in voltage regulation includes:

- There is a **negligible operation cost** of having power converters generating reactive power into the grid. The inverter-based DERs have inherent reactive power capability and the power electronic interfaces are in some cases sized slightly larger (1.1~1.5 times)

than the rated kW capacity of the DERs;

- The power converters have **faster responses** of changing reactive power output than the conventional voltage control devices, such as OLTCs and SCs, so it is able to handle fast voltage variations due to system transients;
- Unlike the discrete control actions by convention voltage control devices, the reactive power injection and absorption of the power converters can be **controlled continuously at a highly granular level**, which helps stabilize system voltage and achieve the optimal operating point.

Therefore, a new voltage control scheme is called for to take advantage of the DERs in distribution systems as voltage control devices in coordination with other utility control devices like SCs and OLTCs to accommodate a larger number of interconnection of DERs in the future.

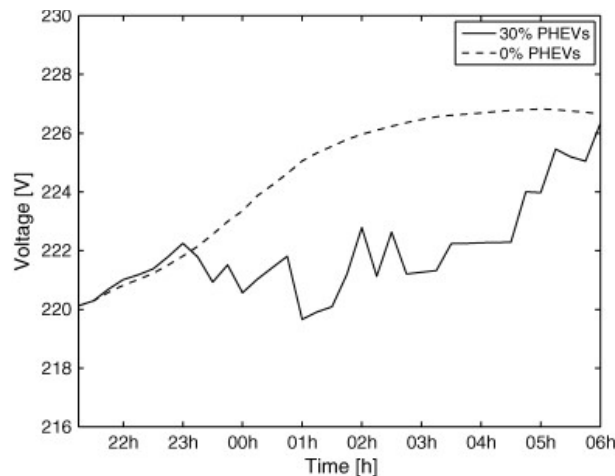


Figure 1.1. An example voltage profile with 30% PHEVs compared to 0% PHEV [2]

The rest of the sections in this chapter are organized as follows. In Section 1.1, the conventional voltage control strategies are summarized, including rule-based control and VVO. In Section 1.2, hierarchical voltage control of microgrids and distribution systems are

discussed with each control level being described. The scope and motivation of the research are discussed in Section 1.3, with the coordinated voltage control framework being proposed.

1.1 Overview of Voltage Control in Distribution Systems

A typical distribution feeder is equipped with SCs and OLTCs for conventional voltage control in distribution systems as shown in Figure 1.2. SCs are usually installed at strategic locations for compensating reactive power consumption along the feeder. The ON/OFF switching control of the SCs are dependent on load variations. As load increases or decreases, the SCs either take action automatically based on the local/remote voltage measurements or are switched in or out by the control from the substation. The voltage regulators are deployed at substation OLTCs, and most of the utilities install line SVRs along the feeder to avoid significant voltage drop at the end of the line. In modern distribution systems, the tap-changing control is determined by either local measurements or remote control the same way as SCs.

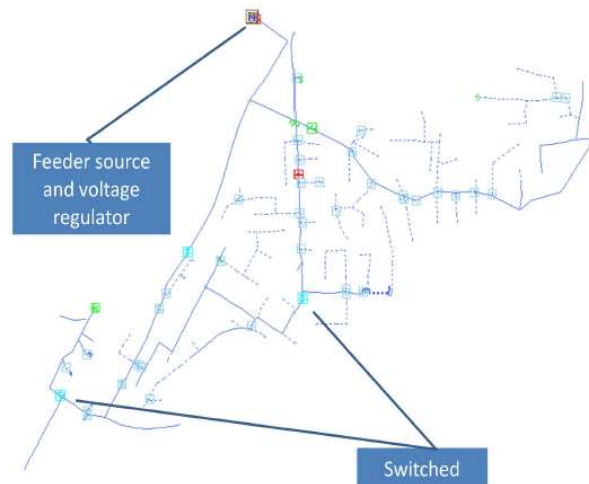


Figure 1.2. An example distribution feeder with SCs and substation OLTCs from Pullman, WA [6]

For a decentralized voltage control strategy, the control of SCs and OLTCs only relies on the local information and control settings. The SCs are set based on certain voltage bandwidth controls: if the measured voltage is beyond the range of the preset bandwidth, the SCs will be

switched in or out depending on whether it's an issue of undervoltage or overvoltage. The temperature-based and time-based control settings are the alternatives for capacitor controls if the loading condition is predictable [7]. For the control of OLTCs, voltage setpoints and bandwidth are also basic settings for voltage regulation and the coordination of multiple OLTCs and SCs are achieved using time-delay settings [7].

The widespread deployment of SCADA and DMS systems in utilities enable distribution system operators to remotely control OLTCs and SCs in a centralized manner. Different rule-based controls were proposed to provide extra benefits while maintaining acceptable voltages at all locations. In [6] and [8], rule-based controls based on load flow analysis are described. The main idea of this centralized voltage control is that (1) the switching of SCs are firstly taking place to make sure the power factor at substation meets the requirements first; (2) after power factor correction, the settings of voltage regulators are adjusted until the voltages are kept acceptable. [9] provides another rule-based control strategy to reduce voltage imbalance due to unbalance loading conditions utilizing single-phase capacitor switching while still keeping voltage and power factor within the desired limits. The rule-based control strategy has several limitations [7]:

- The rule-based control is not flexible and do not adapt to meeting other operation objectives
- The strategy leads to a feasible operating point but not necessarily the optimal solution under all conditions.

The VVO is a more advanced voltage scheme that provides the “optimal” control schedule for all voltage control devices to achieve certain operation objectives. The voltage control, in

this case, is formulated as an optimal reactive power flow problem. The objectives of the optimization problem are listed as follows [7]:

- Minimizing power demand, such as total customer peak demand (CVR) [10]
- Minimizing distribution system power losses [10]-[14], [16] and [17]
- Minimizing the operation and control costs of utility control devices [11], [14] and [15]
- Maximizing power quality, such as flatten voltage profile or maximize power factor [11], [15] and [16]
- Or a combination of the above objectives [11], [14]-[17]

Among different voltage control objectives, CVR is considered as a very important one. CVR refers to full-time operation [18] where the utilities operate at as low voltage as possible without violating voltage limits. The advantage of running CVR on the feeders are threefold: (1) energy reduction (2) demand reduction (3) loss reduction.

The constraints of the VVO problems include both equalities and inequalities constraints. The equality constraints are the power flow equations in distribution systems, which are both non-linear and non-convex. Since the power flow equations are the most computational terms in the optimization problems, many studies on linearization and convex relaxation of power flow equations are proposed [19]-[22]. There are also inequality constraints, including but not limited to:

- Voltage security constraints
- Branch line current limit constraints
- Power factor constraints at substation
- Tap change number limit constraints
- SCs switching number limit constraints

- Tap position limit constraints

In modern distribution systems, high penetration of DERs poses new challenges and opportunities for voltage control in distribution systems. High variability of renewables and fast load changes due to the integration of EVs result in large voltage fluctuations, leading to frequent operation of utility control devices. The wear and tear associated with these additional operations may incur more maintenance costs and fewer life cycles for the equipment [23]. In addition, for the utilities that implement CVR schemes, the DERs may result in voltage rise that has a reverse impact on the performance of energy savings. [23] shows that the Volt-Var control of smart inverters can help mitigate impacts on voltages with high DER penetrations. Therefore, a new voltage control scheme considering reactive power capabilities is called for. A comprehensive literature review on this topic is included in Chapter 3, 4 and 5.

1.2 Hierarchical Voltage Control for Microgrids and Distribution Systems

1.2.1 Primary Control Level

Most of the DERs are the inverter-based generation that connect to distribution systems via power converters although there are also synchronous generators with direct AC connection to the main grid. We focus on inverter-based DERs in this section. First, different types of power converter applications in distribution systems are introduced. Then, because only the grid-supporting converters are relevant to voltage control applications in distribution systems, we focus on modeling of grid-supporting converters with CCM and VCM being discussed. These two control modes of DERs lay the foundation of the proposed hierarchical voltage control framework, that is, the primary control level. Note that the modeling approach is specifically designed for voltage-sourced converter.

Power converters can be classified into three types: grid-feeding converters, grid-forming converters and grid-supporting converters depending on their operation [24]:

grid-forming converters: This type of power converters is controlled as the ideal voltage sources with a given amplitude E^* and frequency ω^* . It is usually used as the voltage reference for an islanded system when grid failure happens.

grid-feeding converters: This type of power converters is controlled as current sources and regulates their output power by adjusting the current injection into the grid. The control needs to synchronize its current output with grid voltage at the connection point to achieve accurate power output regulation. Grid-feeding converters can contribute to grid voltage regulation by adjusting the real/reactive power output, which is usually determined by the real or reactive power setpoints provided by a higher-level control layer. However, it cannot operate in islanded mode except there is the voltage reference in the system, such as a grid-forming converter or a synchronous generator.

grid-supporting converters: This type of power converters is controlled as either voltage sources or current sources depending on their roles in system operation. For grid-supporting converters that are controlled as current sources, the modeling methods are referred to as CCM. Grid-supporting converters under CCM is very similar to grid-feeding converters in a sense that both converters can only operate in the system that already has the voltage reference. But the main difference between two types of converters is power references of grid-supporting converters under CCM are generated by the power controllers instead of higher-layer control. For grid-supporting converters that are controlled as voltage sources, the modeling methods are referred to as VCM. The feature of this modeling method is that the control of this type of converter doesn't rely on synchronizing with the grid voltage. Instead, the reference voltage

amplitude and angle are determined by the V-Q and f-P droop curve. It has several advantages over other types of converters: (1) frequency and voltage regulation in both grid-connected and islanded mode; (2) seamless transition between grid-connected and islanded without any need of connecting grid-forming devices; (3) support power sharing between multiple units without the need of communication.

Figure 1.3 shows the detailed control structure for CCM operation. The idea behind the CCM design is that given the terminal voltage, the converter injects the amount of current such that the real/reactive power output tracks specified power references. The PLL is used to constantly track the phase angle of the terminal grid voltage. The three-phase current is controlled under a static $dq0$ axis which uses the phase angle of terminal voltage as the reference angle. By doing this, we have active/reactive power equations in the $dq0$ axis as

$$\begin{cases} P = \frac{3}{2} [V_d I_d + V_q I_q] \\ Q = \frac{3}{2} [-V_d I_q + V_q I_d] \end{cases} \quad (1.1)$$

where P and Q are DER real/reactive power output, respectively; V_d and V_q are terminal voltages in the d -axis and the q -axis, respectively; I_d and I_q are output currents in the d -axis and the q -axis. Note that (1.1) is valid only in three-phase balancing systems. If we intentionally choose the dq0 rotating frame such that $V_q = 0$, (1.1) yields

$$\begin{cases} P_{ref} = \frac{3}{2} V_d I_{dref} \\ Q_{ref} = -\frac{3}{2} V_d I_{qref} \end{cases} \quad (1.2)$$

where P_{ref} and Q_{ref} are the active/reactive power reference given by the real and reactive power controller, respectively; I_{dref} and I_{qref} are the d -axis and the q -axis current reference for the inner loop current regulator, respectively. It can be seen from (1.2) that active/reactive power can be controlled independently by separately regulating the d -axis and the q -axis

current. The current regulators are achieved using two PI controllers. The Kirchhoff's voltage equations in the $dq0$ axis for the filter inductor L_f are written as

$$\begin{cases} V_{td} = L_f \frac{dI_d}{dt} + V_d - \omega L_f I_q \\ V_{tq} = L_f \frac{dI_q}{dt} + V_q + \omega L_f I_d \end{cases} \quad (1.3)$$

where V_{td} and V_{tq} are output voltage of the converter in the d -axis and the q -axis, respectively.

(1.3) shows that there is still a coupling effect between the d -axis and the q -axis, so the feedforward compensation is added before generating the inverter output voltage reference to cancel out the coupling effect, as shown in Figure 1.3.

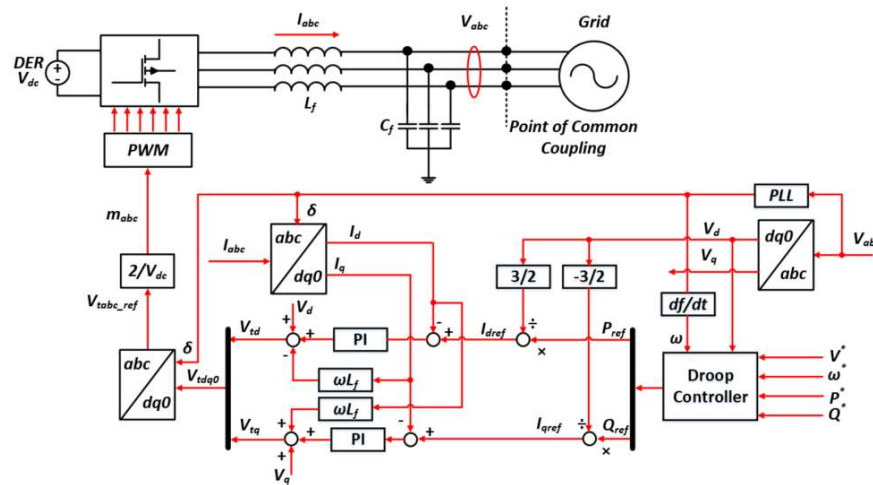


Figure 1.3. The control structure of three-phase grid-supporting power converters under CCM

The real and reactive power controller in CCM is an outer loop control that enables converters to regulate grid voltage and frequency by means of power regulation. The power reference generated by the real and reactive power controllers are sent to inner current control loops. The general expression for the real and reactive power controllers can be expressed as

$$\begin{cases} \omega - \omega^* = -k_P(P - P^*) \\ V - V^* = -k_Q(Q - Q^*) \end{cases} \quad (1.4)$$

where k_P and k_Q are f - P proportional gain and V- Q proportional gain; ω^* and V^* are nominal frequency and voltage magnitude; ω and V are operating frequency and voltage magnitude under current condition; P^* and Q^* are nominal real and reactive power references. Under CCM, the real and reactive power controller takes the ω and V as the feedback and decides how much power should be injected into the grid. The output power reference that are sent to inner current control loops are written as

$$\begin{cases} P_{ref} = -\frac{1}{k_P}(\omega - \omega^*) + P^* \\ Q_{ref} = -\frac{1}{k_Q}(V - V^*) + Q^* \end{cases} \quad (1.5)$$

Note that for grid-connected DERs, such as PV and wind systems, the real power controllers are usually replaced by other types of controllers, such as DC-link voltage regulation and maximum power point tracking [25] and [26], depending on the objective of system operation. Since this work focuses on voltage control in distribution systems, the reactive power controller is maintained, but instead of at the primary control level, the controller is implemented at upper layer control with modifications. The details of the controller design are discussed in Chapter 3.

Figure 1.4 shows the detailed control structure for VCM operation. The VCM design enables DERs to operate like a controlled voltage source, which actively regulates its terminal voltage magnitude and frequency based on its loading condition like a synchronous generator. This design helps stabilize system voltage and frequency and is free from the use of PLL. The idea behind the VCM design is based on the power flow model, which is significantly different from CCM design. Consider a circuit model shown in Figure 1.5, the power flow delivered from power converter to the grid is written as

$$\begin{cases} P = \frac{V_t}{R^2+X^2} [R(V_t - V \cos \delta) + XV \sin \delta] \\ Q = \frac{V_t}{R^2+X^2} [-RV \sin \delta + X(V_t - V \cos \delta)] \end{cases} \quad (1.6)$$

where P and Q are the real/reactive power flowing from power converter to the grid, respectively; V_t and V are voltage magnitude of the power converter and the grid, respectively; δ is the angle difference between these two sources; $R + jX$ is the line impedance between two sources.

When the inductive component is much higher than the resistive one, (1.6) can be rewritten as

$$\begin{cases} P \approx \frac{V_t}{X} (V \sin \delta) \\ Q \approx \frac{V_t}{X} (V_t - V \cos \delta) \end{cases} \quad (1.7)$$

With small-angle approximation $\sin \delta \approx \delta$ and $\cos \delta \approx 1$, (1.7) are further reduced to

$$\begin{cases} \delta \approx \frac{PX}{V_t V} \\ (V_t - V) \approx \frac{QX}{V_t} \end{cases} \quad (1.8)$$

This shows the active/reactive power delivery holds a linear relationship with voltage angle difference and voltage magnitude difference, respectively. Therefore, the droop controller is used to adjust the terminal voltage of the converter until the system reaches steady-state. The voltage references determined by the droop control can be expressed as

$$\begin{cases} \omega_{ref} = \omega^* - k_P (P - P^*) \\ V_{ref} = V^* - k_Q (Q - Q^*) \end{cases} \quad (1.9)$$

As shown in Figure 1.4, the voltage reference is sent to the voltage control loop which regulates the voltage of the capacitor to track the voltage reference. The output of the outer voltage loop is obtained as the current reference for the inner current control loops, which have the same structure as the CCM. The grid-supporting converter under VCM has voltage regulation capability in both grid-connected mode and islanded mode and allows islanded

operation without any other voltage source. However, due to the characteristic of droop control, it has some limitations on accurately tracking reactive power. In grid-connected operation, there are many scenarios when the upper layer control asks for the specified amount of real/reactive power. To address the issues of accurate reactive power tracking, the proportional coefficient in Volt-Var droop control is replaced by a PI controller in grid-connected mode in this study. In cases when frequency and voltage regulation are the priority, such as islanded operation, the Volt-Var control switches back to the proportional controller to guarantee system stability.

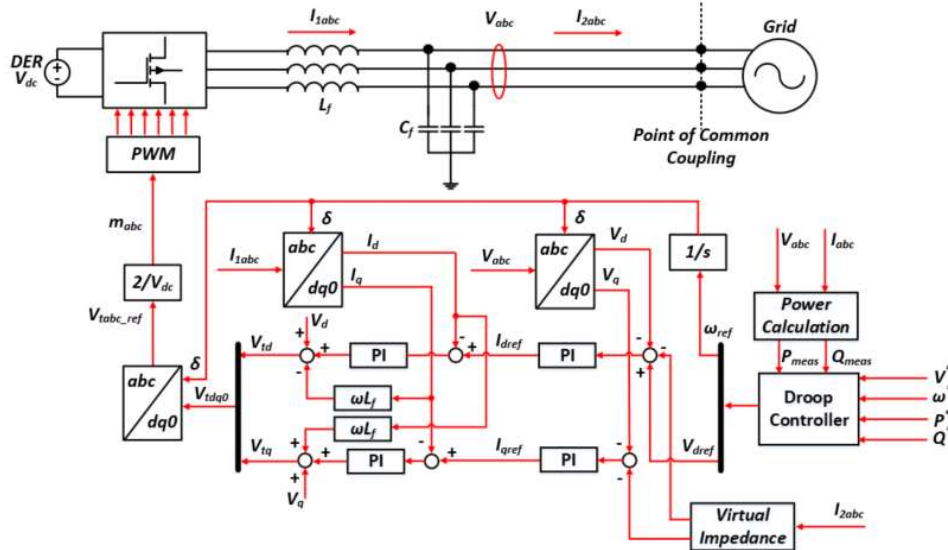


Figure 1.4. The control structure of three-phase grid-supporting power converters under VCM

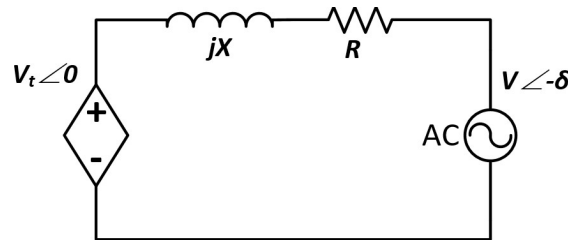


Figure 1.5. Equivalent circuit of power converter connecting to a distribution network

It's worth mentioning that the droop control under VCM assumes that the grid is mainly inductive, which might be not the case for low voltage distribution networks. When the grid

has a large R/X ratio, the approximation in (1.7) doesn't hold any more, indicating the real/reactive power control should not be treated separately. To address this issue, a virtual impedance control is introduced to emulate the voltage response equivalent to the situation when a large output impedance is connected between the PCC and the main grid. Then the new voltage reference for the voltage control loop is modified by subtracting the voltage drop on the virtual impedance from the original voltage reference,

$$\begin{cases} V'_{dref} = V_{dref} - (I_{2d}R_V - I_{2q}X_V) \\ V'_{qref} = 0 - (I_{2d}X_V + I_{2q}R_V) \end{cases} \quad (1.10)$$

where V'_{dref} and V'_{qref} are the modified voltage reference due to virtual impedance control; R_V and X_V are the designed virtual resistance and impedance, respectively; I_{2d} and I_{2q} are the d -axis and the q -axis grid current, respectively.

Although the penetration of grid-connected DERs are rapidly increasing in distribution systems, most of them are only allowed by utilities to operate at unity power factor until recently when they are allowed to provide voltage regulation capability via reactive power support by the IEEE 1547-2018 standard [5]. The new voltage control capabilities for DERs are defined in Table 1.1. For PV or wind systems, the primary level control is mostly implemented using CCM while for large-scale ESS systems, the primary level control is likely to be implemented using VCM.

The reactive power control functions include four operation modes as follows [5]:

constant power factor mode: Under this mode, the DER operates at a constant power factor.

The power factor settings are allowed to be adjusted locally or remotely by the distribution system operator.

voltage-reactive power mode: Under this mode, the DER actively controls its reactive power output as a function of voltage following a Volt-Var piecewise linear characteristic. An example of Volt-Var characteristic is shown in Figure 1.6. The default parameters for this characteristic are found in [5] but the configuration of the parameters is allowable and can be adjustable locally or remotely by the distribution system operator. This mode is also usually referred to as the Volt-Var mode.

active power-reactive power mode: Under this mode, the DER actively controls its reactive power output as a function of active power output following a target piecewise linear active power-reactive power characteristic, as shown in Figure 1.7. The default parameters for this characteristic are found in [5] but the configuration of the parameters is allowable and can be adjustable locally or remotely by the distribution system operator. Note that the left-hand side of Figure 1.7 should only apply to the DER capable of absorbing active power, such as ESS.

constant reactive power mode: Under this mode, the DER maintains a constant reactive power output. The target reactive power level is allowed to be adjusted locally or remotely by distribution system operation.

Table 1.1. Voltage and reactive/active power control function requirements for DER normal operating performance categories [5]

DER category	Category A	Category B
Voltage regulation by reactive power control		
Constant power factor mode	Mandatory	Mandatory
Voltage—reactive power mode ^a	Mandatory	Mandatory
Active power—reactive power mode ^b	Not required	Mandatory
Constant reactive power mode	Mandatory	Mandatory
Voltage and active power control		
Voltage—active power (volt-watt) mode	Not required	Mandatory

^aVoltage-reactive power mode may also be commonly referred to as “volt-var” mode.

^bActive power-reactive power mode may be commonly referred to as “watt-var” mode.

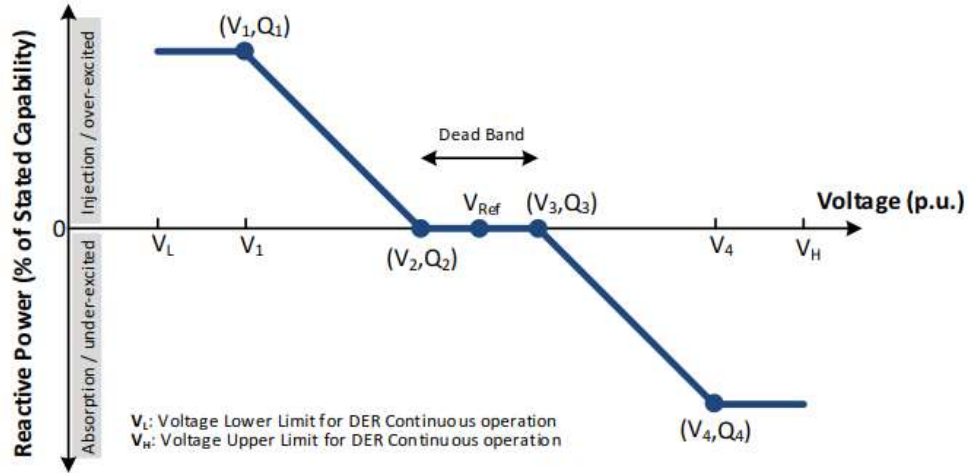


Figure 1.6. An example of Volt-Var characteristics [5]

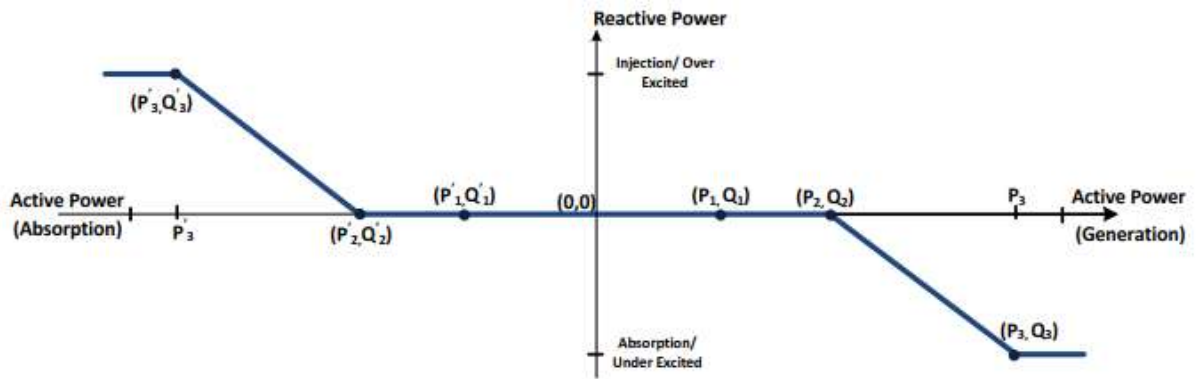


Figure 1.7. An example of active power-reactive power characteristics [5]

Among those advanced voltage control modes, constant power factor mode and Volt-Var mode are already utilized by utilities in California and Hawaii as one of their PV interconnection strategies. Researches are proposing local voltage control strategies based on Volt-Var mode with stability issues being discussed. [27] shows that power system dynamics with local Volt-Var control are equivalent to a distributed optimization problem. Since the stability condition is restrictive for the general Volt-Var control, two incremental control strategies are provided with less strict convergence conditions. In [20], a gradient-projection based local voltage control that generalizes different Volt-Var control methods is proposed. The stability conditions are given for choosing step size parameters of gradient-projection

methods. An adaptive Volt-Var control is proposed in [28]. The control parameters are self-adaptive under changing operating conditions and external disturbances.

1.2.2 Secondary Control Level

Microgrids, as the building blocks of smart grids, are also considered as an important part of distribution systems. By integrating a cluster of DERs and loads, the microgrids control the power flow from/to the main grid while managing the assets inside the footprint optimally. When large disturbances or grid failure happens, the microgrids isolate from the main grid and operate as a standalone island, leading to high reliability and resilience.

The secondary control under the context of the microgrids often refers to the control layer that drives the frequency and voltage magnitude to the nominal levels, as shown in Figure 1.8.

This control is mainly implemented in the islanded operation as follows [29]:

$$\Delta\omega = k_{p\omega}(f^* - f) + k_{i\omega} \int (f^* - f) dt \quad (1.11a)$$

$$\Delta E = k_{pE}(E^* - E) + k_{iE} \int (E^* - E) dt \quad (1.11b)$$

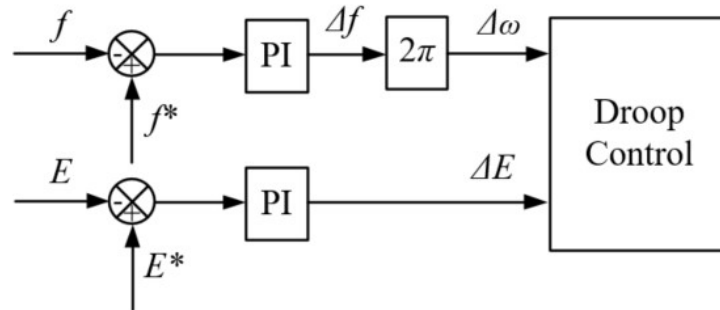


Figure 1.8. An example of secondary control for islanded microgrids

During grid-connected operation, since power flows between microgrids and distribution systems can be controlled, microgrids can provide ancillary services to the main grids. As the IEEE 2030.7 standard [30] specifies, voltage control using reactive power production is one of the ancillary services provided by microgrids. To avoid confusion, the secondary control level in this study refers to the grid-interactive controller that allows microgrid to respond to voltage

disturbances in distribution systems. The detailed literature review on the grid-interactive microgrid controller can be found in Chapter 3.

1.2.3 Tertiary Control Level

The tertiary control level in this study is a system-level voltage management based on primary control and secondary control. The objective of this control level is to achieve optimal operation across the system while respecting system security constraints. A typical approach for the tertiary control is VVO (or optimal power flow). An extensive literature review is found in both Chapter 4 and Chapter 5.

The VVO has been one of the main applications of the ADMS, and many vendors, such as General Electric and ABB, have integrated the VVO into their ADMS software platform [31]-[32]. Figure 1.9 shows an example of a DMS-based VVO solution. Based on the distribution system model updated by GIS information, real-time configuration, and real-time feeder measurements, the online power flow is computed, and the results are sent to the VVO optimizing engine. After the control actions determined by VVO optimizing engine, online power flow is rerun to check whether control actions improve the VVO operating objectives. Once the improvement of operating objectives is confirmed, the VVO sends the requested control to distribution SCADA to execute control actions [33].

The ADMS, as an integrated software platform, supports the full functionality of distribution management and optimization, including FLISR, VVO, CVR, peak demand management and support for DERs, EVs and microgrids. Figure 1.10 shows the architecture of ADMS and the interactions with other enterprise systems. The key building blocks of the ADMS include distribution SCADA, advanced distribution applications, and interfaces to external systems. Distribution SCADA enables the DMS to monitor field equipment in real-

time or near-real-time and to initiate and execute remote control actions for controllable field devices in response to operator commands or control actions from distribution applications [33]. Take VVO for example, control actions include raising/lowering tap settings of SVRs or switching capacitor banks in/out. Another major DMS building blocks are the advanced distribution applications, which are built upon distribution SCADA monitoring and control capabilities to provide decision making and automatic control capabilities for system optimization [33]. Besides distribution SCADA, advanced distribution applications exchange information with other enterprise-level facilities. For example, many advanced distribution applications rely on the distribution system models, which are updated and maintained using the information from GIS. Therefore, the ADMS is integrated with other corporate enterprise facilities, such as GIS, OMS, AMI, etc.

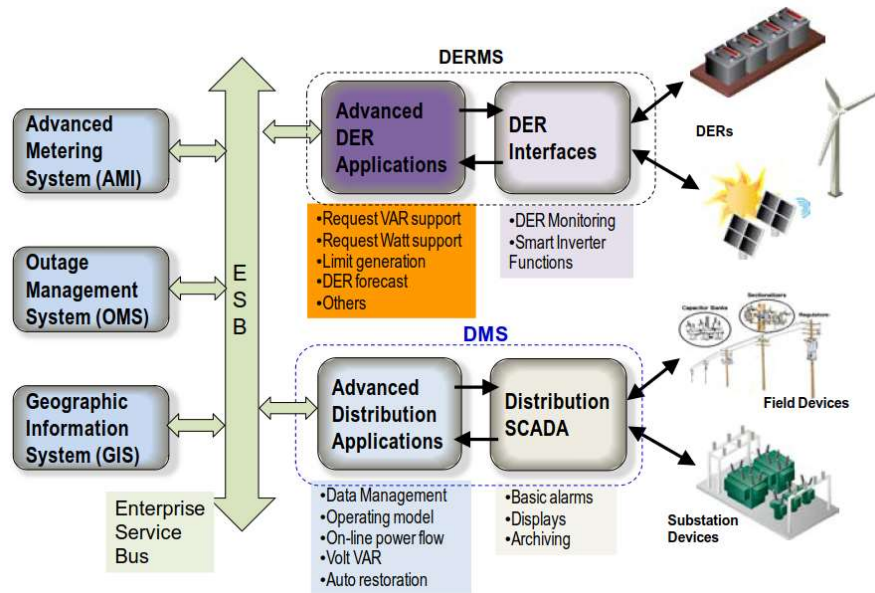


Figure 1.9. An example of ADMS architecture [33]

The DERMS, an important application of ADMS that monitors and controls DERs in distribution systems, is highly relevant to the VVO considering DER integration. As the interfaces to DERs, the DERMS enables the ADMS to have a full view of all grid-connected

DER assets to provide optimal scheduling for both conventional voltage control devices like SCs or OLTCs and the DERs in a coordinated manner. A general architecture of the DERMS is depicted in Figure 1.11. In addition, multi-microgrid control functions can also be added to the DERMS.

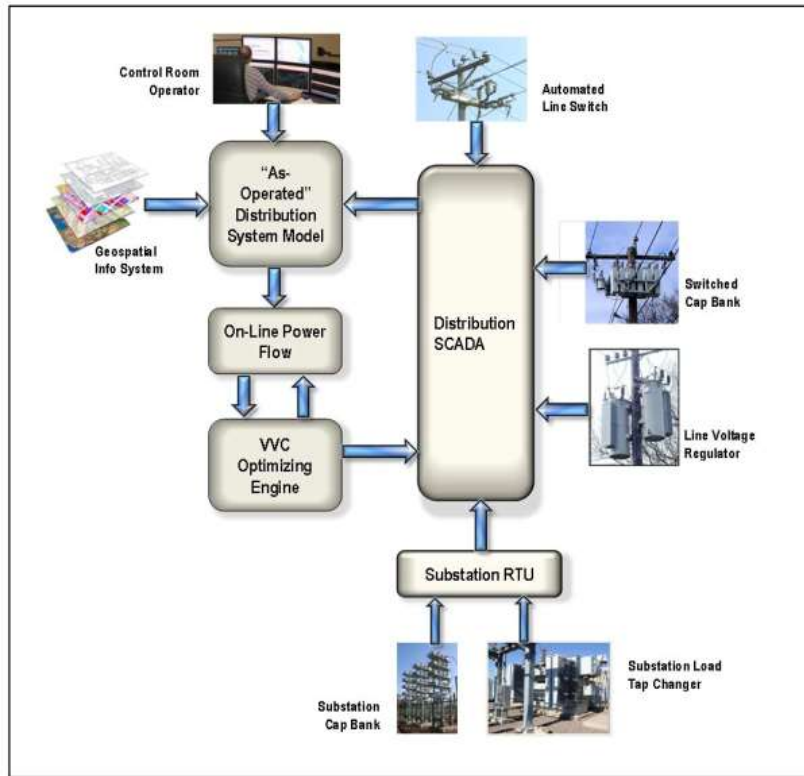


Figure 1.10. An example of a DMS-based model-driven VVO solution [33]

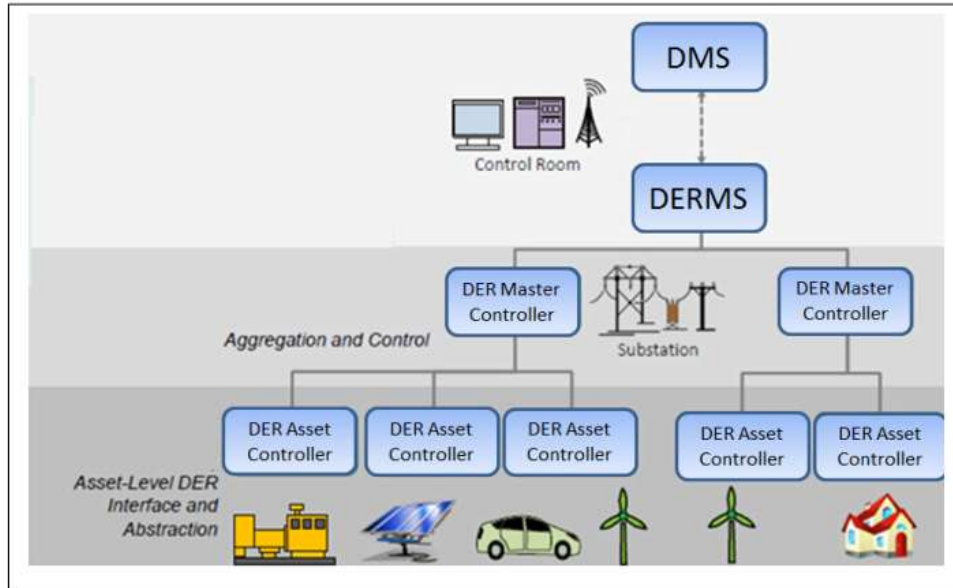


Figure 1.11. A general architecture of DERMS [33]

1.3 Proposed Hierarchical Approaches

Given the fact that distribution systems are experiencing an increasing number of interconnection of DERs and microgrids, a hierarchical voltage control framework is proposed in this work to consider voltage control for coordinating legacy utility control devices with DERs and microgrids. The proposed voltage control framework has the following features:

(1) Multiple control layers are developed and designed from top to bottom, including the primary control layer, the secondary control layer, and the tertiary control layer.

(2) The detailed interactions/coordination among multiple control layers are considered in the design of the control framework.

(3) The tertiary voltage control is aimed at providing coordination between utility control devices, such as SCs and OLTCs and voltage support of microgrids and distribution-connected DERs.

(4) The control design is based on Volt-Var control of DERs, which fits in the new IEEE 1547-2018 standard [5].

The architecture of the proposed voltage control framework is shown in Figure 1.12. Multiple control layers are described in detail as follows:

primary control layer: The primary control refers to the component-level control for each voltage control device. Inverter control is the primary control for distribution-connected DERs or DERs inside the microgrids while capacitor controllers and regulator controllers are the primary level control for SCs and OLTCs, respectively. As described in Section 1.4, depending on the type of the DER, there are two control methods for controlling active and reactive power output of the DERs ---- CCM and VCM. In the proposed voltage control framework, the primary control layer receives control signals directly from tertiary control for utility control devices, such as SC switching in/out and tap position increasing/decreasing. While the primary control level executes control setpoints sent by secondary control for DERs that are inside microgrid zones, such as reactive power commands, the primary control of distribution-connected DERs receives control settings directly from the tertiary control layer.

secondary control layer: In this work, this control layer only refers to secondary control for microgrids. To manage power flow at microgrid PCC, control strategies are required to coordinate multiple DERs in the microgrid footprint and make sure the microgrids operate under the settings that are recommended by tertiary layer control. A secondary voltage control strategy is proposed in Chapter 3 to enable microgrids to provide voltage regulation in the same way smart inverters do. By means of the secondary controller, the microgrids comply with the system-level optimal operation without compromising its internal optimization for active power flows with the utility.

tertiary control layer: This control layer is a centralized VVO that are described in Chapter 4 and Chapter 5. The VVO provides discrete control signals for utility control devices, such as

SCs and OLTCs as well as the recommended Volt-Var control settings for distribution-connected DERs and microgrids. The VVO is a model-based day-ahead solution that relies on load forecast and renewable forecast. In Chapter 4, the decisions are made using the deterministic model where the perfect forecast is assumed. Chapter 5 enhances the work in Chapter 4 by developing the stochastic version of the VVO model considering the irradiance uncertainty. The proposed VVO model can turn into a real-time solution as well and will be included in future work.

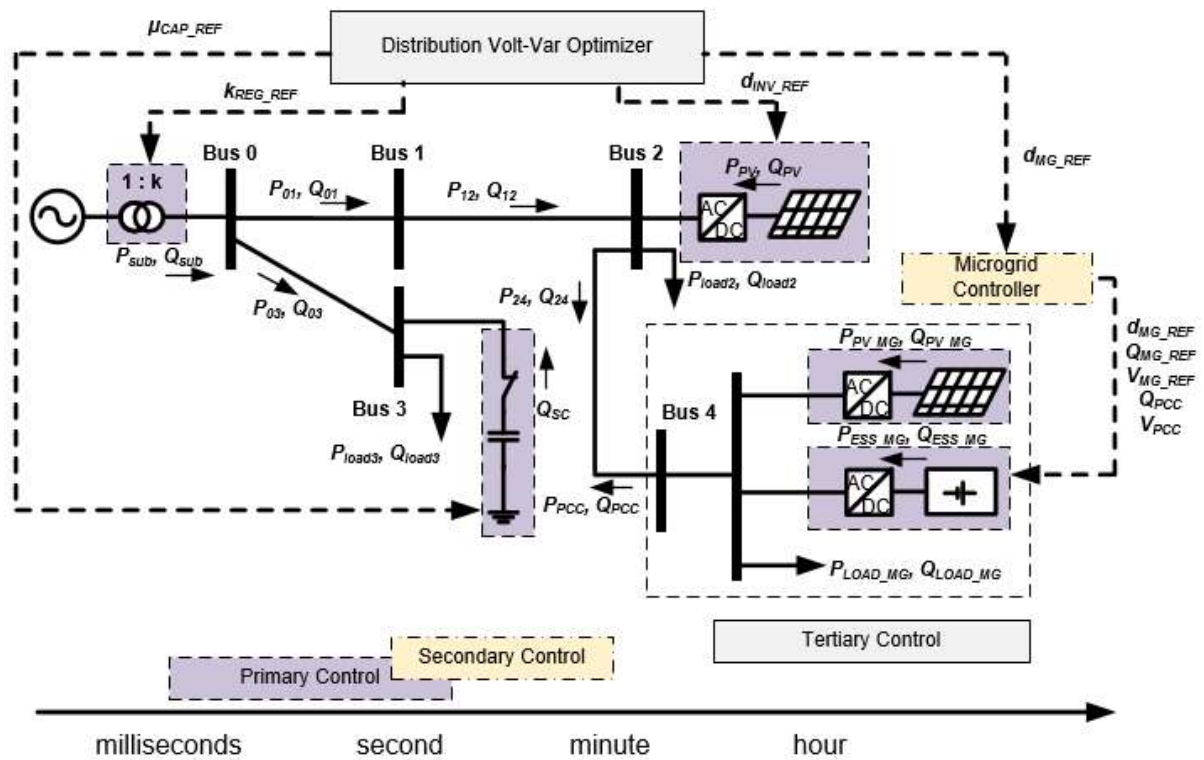


Figure 1.12. The architecture of the proposed hierarchical voltage control framework

CHAPTER 2. MODEL PARAMETERIZATION FOR MICROGRID SIMULATION USING HYBRID BOX-CONSTRAINED LEVENBERG-MARQUARDT ALGORITHM

This chapter proposes a new hybrid algorithm, named hybrid box-constrained Levenberg-Marquardt (H-BCLM) for model parameterization of microgrid components using field measurements. Although the study here focuses on the diesel generator application, the method is applicable to other microgrid components as well, given the field measurements are available. The proposed hybrid algorithm, consisting of a heuristic-based global algorithm and a local search algorithm, proves to be effective in model parameterization only using limited measurements from simple load step tests. The rest of this chapter is organized as follows. Section 2.2 describes the modeling method for diesel generator and the modeling parameters. Section 2.3 discusses the problem formulation as a nonlinear least squares (NLSQ) problem for a dynamic system. Section 2.4 introduces the proposed H-BCLM algorithm. Section 2.5 presents the validation results, and conclusions and future work are provided in Section 2.6.

2.1 Literature Review

Diesel generators are commonly used in hybrid microgrids, in conjunction with inverter-interfaced PV, wind, and energy storage systems [34]-[36]. Therefore, it is critical to understand the dynamic response associated with control interactions between conventional diesel generators and inverter-based DERs. However, in many studies [37]-[38] on control interactions between diesel generators and other DERs, modeling parameters of the diesel generator are arbitrarily obtained from publicly available data sources so it is not guaranteed that the dynamic response of the diesel generator will match field operation results under given operating conditions. In recent years, HIL simulations are increasingly used to replace field testing of microgrid protection and control schemes [39]-[40]. HIL models which are not

sufficiently validated can lead to low-fidelity testing results [41]. Therefore, the model parameterization method is needed for developing high-fidelity microgrid dynamic simulation.

Generator power plant model validation has been well established for power system dynamic studies [42]-[47]. However, the existing generator parameterization methods are mainly applicable to larger-scale steam-turbine generators and there are several technical challenges when applying the existing techniques to diesel generator model parameterization in microgrid applications. First, the existing methods are based on standard testing data or online recording measurements collected from a series of sophisticated testing procedures, such as short-circuit tests, open-circuit tests, load rejection tests, frequency response tests, and so on [43]-[47]. This model validation process requires too large an investment for small microgrid owners. Thus, it is important to limit the scale, duration, and complexity of the field tests. Second, the existing methods heavily rely on information from manufacturer datasheets such as equipment parameters, factory test results, and electromagnetic transient (EMT) benchmark models [42] and [45]. For example, the generator parameters from manufacture datasheets are needed as initial estimates for the model parameters. However, the manufacturer datasheet of the small-scale diesel generators does not contain as much information as multi-MW generator sets. Therefore, it is also desirable that the developed method is free from initial estimate selection. Third, the parameterization process needs to be automated with clearly defined performance metrics, such as accuracy, applicable operation conditions and parameter ranges. Thus, the manual approach from only trial-and-error or expert knowledge [45] is not applicable.

More advanced techniques have been recently proposed for model parametrization. A model parameterization approach using the Gauss-Newton algorithm is applied to solve the

parameter estimation problem for power plant models [48]. However, the Gauss-Newton algorithm can encounter numerical difficulties for ill-conditioned problems. The trust-region-reflective (TRR) based algorithms [49] and [50] are chosen to solve parameter estimation problems with improved numerical robustness, but the performance of these algorithms depends on initial solution selection. There are researchers applying pure heuristic algorithms to parameter estimation. A new model identification method is introduced in [51] using a hybrid Cuckoo search algorithm to parameterize standard gas turbine and exciter models. A Particle-Swarm-Optimization based strategy is applied for key parameter estimation of permanent magnet synchronous machines with the inverter interface considered [52]. Although the authors mention that their methods can work with nonlinear models, it is also noted that these heuristic methods are easily subject to long convergence time and premature convergence when dealing with nonlinear models.

To overcome the limited capability of the above-mentioned techniques, a new parameterization method using the H-BCLM algorithm is proposed to automatically estimate a complete parameter set for diesel generator models. Although a few hybrid algorithms are already proposed for model parameterization [50] and [53], these algorithms are tailored to fit into PV and battery models that only contain algebraic equations. In this study, the diesel generator model parameterization problem is formulated as a NLSQ problem for the dynamic system. Only field measurements from load-step-change tests are used as the inputs of the algorithm. The proposed H-BCLM algorithm consists of two stages. A heuristic algorithm is first applied to find reasonable initial solutions within the predefined bounds, making the algorithm independent of the manufacture datasheet. Because this NLSQ problem is ill-conditioned and rank-deficient, the Levenberg-Marquardt (LM) algorithm is selected in this

study to improve the robustness of the method. As a variant of the LM algorithm, the BCLM algorithm is implemented as a local search strategy to solve the NLSQ problem in consideration of physical bounds of the parameters.

2.2 Modeling Methodologies

2.2.1 Diesel Generator Model

As shown in Figure 2.1-2.3, the diesel generator model consists of multiple subsystems: diesel engine, excitation system, and synchronous generator. The model parameters are listed in Table 2.1.

In this study, the simplified diesel engine model introduced in [38] is used. As shown in Figure 2.1, the model contains two elements: a proportional speed control and a mechanical actuator system. If zero steady-state error is required, the proportional speed control can be replaced by a proportional-integral-derivative controller. The dynamic model of the diesel engine can be expressed as:

$$\begin{cases} \dot{q}_1 = q_2 \\ \dot{q}_2 = -\frac{1}{T_2 T_3} q_1 - \frac{T_2 + T_3}{T_2 T_3} q_2 + P_{ref} + m(\omega_{ref} - \omega) \end{cases} \quad (2.1)$$

$$P_m = \frac{1}{T_2 T_3} q_1 + \frac{T_1}{T_2 T_3} q_2 \quad (2.2)$$

where q_1 and q_2 are state variables in the controllable canonical form of the diesel engine; P_m is the mechanical power; ω is the rotor speed.

As shown in Figure 2.2, the excitation system model [54], consists of an automatic voltage regulator (AVR) and an exciter. The AVR is modeled as a first-order transfer function while the exciter is modeled as a proportional-integral controller. A saturation block is added after the exciter output to avoid the excitation voltage from reaching an infeasible range. The excitation system model is expressed as:

$$\begin{cases} \dot{\xi}_1 = \xi_2 \\ \dot{\xi}_2 = -\frac{1}{T_V}\xi_2 + (V_{tref} - V_t) \end{cases} \quad (2.3)$$

$$V_f = \frac{K_V K_{ie}}{T_V} \xi_1 + \frac{K_V K_{pe}}{T_V} \xi_2 \quad (2.4)$$

where ξ_1 and ξ_2 are state variables in the controllable canonical form of the excitation system; V_t are measured stator voltage magnitude; V_f is the excitation voltage.

The synchronous generator model is built based on the flux decay model in [55], as shown in Figure 2.3. It is derived by eliminating fast damper winding dynamics T'_{qo} when the inequality condition $T'_{qo} \ll T'_{do}$ holds true for the generator. The synchronous generator model includes both field winding dynamics and machine dynamics, and the equations are written as a third-order system as follows:

$$\begin{cases} \frac{2H}{\omega_s} \dot{\omega} = P_m - E'_q I_q - (X_q - X'_d) I_d I_q - D_f \omega \\ T'_{d0} \dot{E}'_q = -E'_q - (X_d - X'_d) I_d + V_f \\ \dot{\delta} = \omega - \omega_s \end{cases} \quad (2.5)$$

where E'_q is the field flux linkage; I_d and I_q are the d -axis and the q -axis stator currents; δ is the rotor angular position.

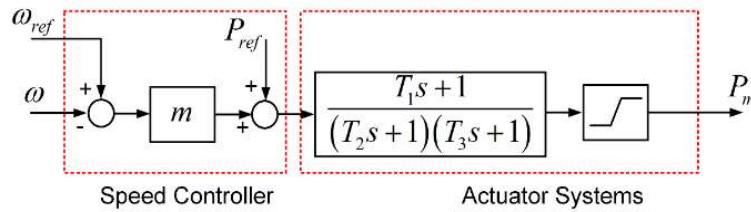


Figure 2.1. Diesel engine model diagram

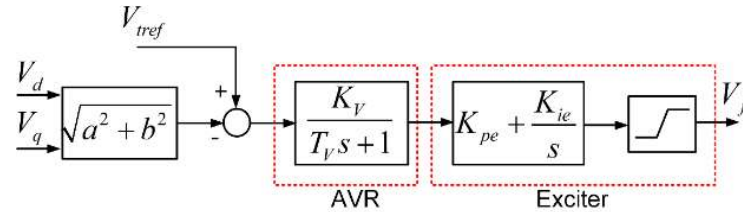


Figure 2.2. Excitation system model diagram

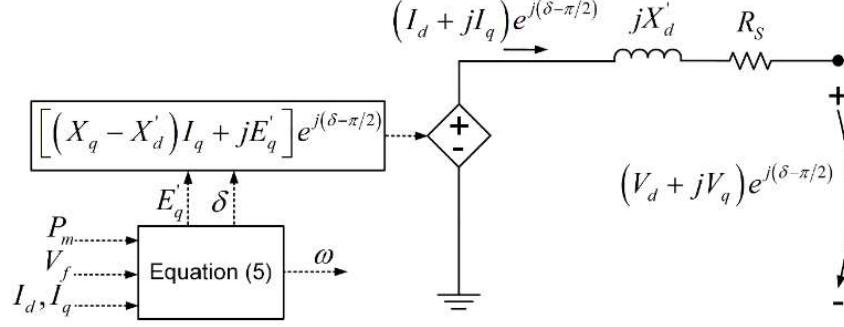


Figure 2.3. Synchronous generator model one-line diagram

The diesel generator model (2.1-2.5) is a seventh-order nonlinear dynamic system. Note that there are also network constraints that are written as algebraic equations. However, all the algebraic equations can be eliminated by substituting them into the differential equations. The form of the algebraic equations depends on the characteristics of the network. In a typical test setup, the network constraints simply represent one component, such as a source, a passive load or an induction motor. Take resistive loads for example, where the algebraic equations are written as follows:

$$\begin{bmatrix} 0 \\ E'_q \end{bmatrix} = \begin{bmatrix} R_s + R_{load} & -X_q \\ X'_d & R_s + R_{load} \end{bmatrix} \begin{bmatrix} I_d \\ I_q \end{bmatrix} \quad (2.6)$$

$$\begin{bmatrix} V_d \\ V_q \end{bmatrix} = \begin{bmatrix} R_{load} & 0 \\ 0 & R_{load} \end{bmatrix} \begin{bmatrix} I_d \\ I_q \end{bmatrix} \quad (2.7)$$

$$V_t = \sqrt{V_d^2 + V_q^2} \quad (2.8)$$

2.2.2 Model Parameters

Table 2.1 lists all the parameters of the diesel generator model proposed in Section 2.2.1. To find proper values for this complete set of parameters is difficult, especially for small-scale diesel generators. It is because the manufacturer datasheet of small-scale diesel generators is likely not to be as informative and reliable as of the MW-level generators. Therefore, the

proposed model parameterization method is useful in this situation to get a decent parameter set for diesel generator modeling given only load-step-change test measurements.

Table 2.1. Diesel generator model parameters

Symbol	Description	Units
m	Speed droop gain	unitless
ω_{ref}	Speed reference	p.u.
P_{ref}	Power reference	p.u.
T_1, T_2, T_3	Diesel engine time constants	sec
V_{tref}	Terminal voltage reference	p.u.
T_V	AVR gain	sec
K_V	AVR time constant	unitless
K_{pe}, K_{ie}	PI gains for the exciter	unitless
H	Inertia coefficient	sec
ω_s	Synchronous speed	p.u.
D_f	Friction factor	p.u.
X_d	d -axis synchronous reactance	p.u.
X'_d	d -axis transient reactance	p.u.
X_q	q -axis synchronous reactance	p.u.
T'_{do}	d -axis transient open-circuit time constant	sec
R_s	Stator resistance	p.u.

A practical aspect of the model parameterization process is to decide initial estimates and parameter bounds. There are cases where certain parameters are provided in the manufacturer datasheets. For example, the data are likely to be available for reactance of the generator, such as the dq -axis synchronous and transient reactance X_d, X_q and X'_d . Then these parameter values are considered the initial estimates with tight bounds while the rest of the parameters are free to vary in a significant range.

2.3 Diesel Generator Model Parameterization Problem Formulation

2.3.1 Problem Formulation

The goal of the model parameterization problem is to find an optimal set of model parameters such that the mismatch between model response and the given field measurements

is minimized. The problem falls into the category of NLSQ problems, whose objective is defined as follows:

$$\min_{\boldsymbol{\theta}} h(\boldsymbol{\theta}) = \min_{\boldsymbol{\theta}} \frac{1}{2} \sum_{k=1}^N \|z(t_k) - \mathbf{y}(\boldsymbol{\theta}, t_k)\|_2^2 \quad (2.9)$$

where $\boldsymbol{\theta}$ is the vector in \mathbb{R}^n containing model parameters to be estimated and n is the length of the system parameter vector; $z(t_k)$ and $\mathbf{y}(\boldsymbol{\theta}, t_k)$ are the measured and simulated output vectors at the time t_k , respectively, and both are in \mathbb{R}^m ; m is the length of the system output vector; N is the number of data points.

The objective function (2.9) is subject to the nonlinear dynamic system equations defined above for the diesel generator model (2.1-2.8), with general representation written as follows:

$$\dot{\mathbf{x}}(t) = \mathbf{f}[\mathbf{x}(t), \mathbf{u}(t), \boldsymbol{\theta}], \mathbf{x}(t_0) = \mathbf{x}_0 \quad (2.10)$$

$$\mathbf{y}(t) = \mathbf{g}[\mathbf{x}(t), \mathbf{u}(t), \boldsymbol{\theta}] \quad (2.11)$$

where $\mathbf{x}(t)$ is the state variable vector; $\mathbf{u}(t)$ is the input disturbance vector; \mathbf{x}_0 is the state variable vector with initial condition; $\mathbf{y}(t)$ is the output vector equivalent to $\mathbf{y}(\boldsymbol{\theta}, t_k)$.

The functions \mathbf{f} and \mathbf{g} are nonlinear and real-valued. The diesel generator parameter bounds are defined in advance as follows:

$$\underline{\theta}_i \leq \theta_i \leq \overline{\theta}_i; i = 1, \dots, n \quad (2.12)$$

where $\underline{\theta}_i$ and $\overline{\theta}_i$ are the lower and upper bounds of θ_i . The parameter bounds should be set to be consistent with the physical meanings of the parameters. For example, time constants should be always greater than zero. Besides, the parameter bounds should be further tightened given any additional information and expert knowledge.

2.3.2 Nonlinear Least Squares for Dynamic Systems

To solve the NLSQ problems (2.9-2.12), the stationary points must satisfy the first-order optimality condition:

$$\frac{\partial \mathbf{h}(\boldsymbol{\theta})}{\partial \boldsymbol{\theta}} = - \sum_{k=1}^N \left(\frac{\partial \mathbf{y}(\boldsymbol{\theta}, t_k)}{\partial \boldsymbol{\theta}} \right)^T (\mathbf{z}(t_k) - \mathbf{y}(\boldsymbol{\theta}, t_k)) = \mathbf{0} \quad (2.13)$$

Starting from an initial estimate $\boldsymbol{\theta}_0$, a Newton iteration is used to solve the above Equation (2.13) and is executed as follows:

$$\boldsymbol{\theta}_{i+1} = \boldsymbol{\theta}_i - \left[\left(\frac{\partial^2 \mathbf{h}(\boldsymbol{\theta})}{\partial \boldsymbol{\theta}^2} \right)_i \right]^{-1} \left(\frac{\partial \mathbf{h}(\boldsymbol{\theta})}{\partial \boldsymbol{\theta}} \right)_i \quad (2.14)$$

where i is the iteration index, and the Hessian matrix of the objective function is given as follows:

$$\frac{\partial^2 \mathbf{h}(\boldsymbol{\theta})}{\partial \boldsymbol{\theta}^2} = \sum_{k=1}^N \left(\frac{\partial \mathbf{y}(\boldsymbol{\theta}, t_k)}{\partial \boldsymbol{\theta}} \right)^T \left(\frac{\partial \mathbf{y}(\boldsymbol{\theta}, t_k)}{\partial \boldsymbol{\theta}} \right) - \sum_{k=1}^N \left(\frac{\partial^2 \mathbf{y}(\boldsymbol{\theta}, t_k)}{\partial \boldsymbol{\theta}^2} \right)^T (\mathbf{z}(t_k) - \mathbf{y}(\boldsymbol{\theta}, t_k)) \quad (2.15)$$

Based on Equation (2.13-2.15), it can be seen that three types of computation are required for each iteration of the parameter update: 1) the system output response $\mathbf{y}(\boldsymbol{\theta}, t_k)$ evaluated at $\boldsymbol{\theta}_i$; 2) the gradient of the system output response $\frac{\partial \mathbf{y}(\boldsymbol{\theta}, t_k)}{\partial \boldsymbol{\theta}}$ evaluated at $\boldsymbol{\theta}_i$; and 3) the Hessian matrix of the system output response $\frac{\partial^2 \mathbf{y}(\boldsymbol{\theta}, t_k)}{\partial \boldsymbol{\theta}^2}$ evaluated at $\boldsymbol{\theta}_i$.

The computation of model response $\mathbf{y}(\boldsymbol{\theta}, t_k)$ only relies on the estimated parameters $\boldsymbol{\theta}_i$ and the state variable vector $\mathbf{x}(t)$. The latter is obtained by simply integrating the state equation (2.10).

The gradient of system output response $\frac{\partial \mathbf{y}(\boldsymbol{\theta}, t_k)}{\partial \boldsymbol{\theta}}$ requires more involved computation, especially for nonlinear systems. The analytical approach to obtain partial derivatives of the system equations (2.10-2.11) is not used in this study for two reasons [56]. First, any model structure change requires the rederivation of partial derivatives. Besides, for a system with

discontinuous nonlinearities, it is intractable to define the derivatives analytically. The approach used in this study is to approximate the derivative of the system output response using the forward difference approximation [56]:

$$\left[\frac{\partial \mathbf{y}(\boldsymbol{\theta}, t_k)}{\partial \boldsymbol{\theta}} \right]_{ij} \approx \frac{\tilde{y}_i(\tilde{\boldsymbol{\theta}}, t_k) - y_i(\boldsymbol{\theta}, t_k)}{\delta \theta_j} \approx \frac{g_i(\tilde{\mathbf{x}}(t), \mathbf{u}(t), \tilde{\boldsymbol{\theta}}) - g_i(\mathbf{x}(t), \mathbf{u}(t), \boldsymbol{\theta}))}{\delta \theta_j}$$

$$i = 1, \dots, m; j = 1, \dots, n \quad (2.16)$$

where $\delta \theta_j$ is a small perturbation of the j th entry of $\boldsymbol{\theta}$; $\tilde{y}_i(\tilde{\boldsymbol{\theta}}, t_k)$ is the i th perturbed output of the response; $\tilde{\mathbf{x}}(t)$ and $\tilde{\boldsymbol{\theta}}$ are the perturbed state variable vector and parameter vector corresponding to $\delta \theta_j$. How $\tilde{y}_i(\tilde{\boldsymbol{\theta}}, t_k)$ is computed is similar to $\mathbf{y}(\boldsymbol{\theta}, t_k)$, as explained previously, except that the parameter vector $\boldsymbol{\theta}$ is replaced by the perturbed parameter vector $\tilde{\boldsymbol{\theta}}$. This is a general method that can be applied to any nonlinear system, thus avoiding the rederivation of partial derivatives.

The Hessian matrix of the system output response is the most computationally expensive term to compute. One common approach is to neglect the second term in (2.15) based on the assumption that the residual $\mathbf{z}(t_k) - \mathbf{y}(\boldsymbol{\theta}, t_k)$ is close to zero in a small-sized neighborhood of the solution $\boldsymbol{\theta}^*$. Therefore, substituting (2.13) and (2.15) into (2.14) yields the parameter update estimate as follows:

$$\Delta \boldsymbol{\theta}_i \approx \left(\sum_{k=1}^N \left(\frac{\partial \mathbf{y}(\boldsymbol{\theta}, t_k)}{\partial \boldsymbol{\theta}} \right)_i^T \left(\frac{\partial \mathbf{y}(\boldsymbol{\theta}, t_k)}{\partial \boldsymbol{\theta}} \right)_i \right)^{-1} \left(\sum_{k=1}^N \left(\frac{\partial \mathbf{y}(\boldsymbol{\theta}, t_k)}{\partial \boldsymbol{\theta}} \right)_i^T \left(\mathbf{z}(t_k) - \mathbf{y}(\boldsymbol{\theta}, t_k) \right)_i \right)$$

$$(2.17)$$

2.4 Hybrid Box-Constrained Levenberg-Marquardt Algorithm

2.4.1 Levenberg-Marquardt Algorithm

The diesel generator model parameterization problem can be an ill-conditioned NLSQ problem. $\frac{\partial \mathbf{y}(\boldsymbol{\theta}, t_k)}{\partial \boldsymbol{\theta}}$ is a $m \times n$ matrix with $m < n$ because the number of measurement points, such as frequency and voltage, are less than the number of the parameters to be estimated. Therefore, an inequality is derived as follows:

$$\begin{aligned} & \text{Rank} \left[\left(\frac{\partial \mathbf{y}(\boldsymbol{\theta}, t_k)}{\partial \boldsymbol{\theta}} \right)_i^T \left(\frac{\partial \mathbf{y}(\boldsymbol{\theta}, t_k)}{\partial \boldsymbol{\theta}} \right)_i \right] \\ & \leq \min \left(\text{Rank} \left(\left(\frac{\partial \mathbf{y}(\boldsymbol{\theta}, t_k)}{\partial \boldsymbol{\theta}} \right)_i^T \right), \text{Rank} \left(\left(\frac{\partial \mathbf{y}(\boldsymbol{\theta}, t_k)}{\partial \boldsymbol{\theta}} \right)_i \right) \right) \\ & \leq m < n \end{aligned}$$

One can see that the $n \times n$ matrix $\left(\frac{\partial \mathbf{y}(\boldsymbol{\theta}, t_k)}{\partial \boldsymbol{\theta}} \right)_i^T \left(\frac{\partial \mathbf{y}(\boldsymbol{\theta}, t_k)}{\partial \boldsymbol{\theta}} \right)_i$ is a rank-deficient matrix. Because the input disturbance $\mathbf{u}(t)$ represents step load change and it lacks input signal richness [57], $\sum_{k=1}^N \left(\frac{\partial \mathbf{y}(\boldsymbol{\theta}, t_k)}{\partial \boldsymbol{\theta}} \right)_i^T \left(\frac{\partial \mathbf{y}(\boldsymbol{\theta}, t_k)}{\partial \boldsymbol{\theta}} \right)_i$ can also be a rank-deficient matrix, which is singular and noninvertible. In this case, the problem is an ill-conditioned NLSQ problem. If conventional algorithms such as Gauss-Newton algorithm are applied to the problem [58], divergence will occur because of the singularity of $\sum_{k=1}^N \left(\frac{\partial \mathbf{y}(\boldsymbol{\theta}, t_k)}{\partial \boldsymbol{\theta}} \right)_i^T \left(\frac{\partial \mathbf{y}(\boldsymbol{\theta}, t_k)}{\partial \boldsymbol{\theta}} \right)_i$. Techniques such as singular value decomposition can be used, but the convergence will generally be very slow [58].

The LM algorithm, however, is robust when addressing ill-conditioned problems [58] by introducing a trust region for $\Delta \boldsymbol{\theta}$. The objective function of the NLSQ problem (2.9) becomes

$$\min_{\Delta \boldsymbol{\theta}} \sum_{k=1}^N \left\| - \left(\frac{\partial \mathbf{y}(\boldsymbol{\theta}, t_k)}{\partial \boldsymbol{\theta}} \right)_i^T \Delta \boldsymbol{\theta} + \left(\mathbf{z}(t_k) - \left(\mathbf{y}(\boldsymbol{\theta}, t_k) \right)_i \right) \right\|_2^2 + \lambda_i \|\Delta \boldsymbol{\theta}\|_2^2 \quad (2.18)$$

where λ_i is the LM parameter that controls both update search direction and step size at the i th iteration. The normal equation of (2.18), which becomes the parameter update formula, is written as follows:

$$\Delta\boldsymbol{\theta}_i = \left(\sum_{k=1}^N \left(\frac{\partial \mathbf{y}(\boldsymbol{\theta}, t_k)}{\partial \boldsymbol{\theta}} \right)_i^T \left(\frac{\partial \mathbf{y}(\boldsymbol{\theta}, t_k)}{\partial \boldsymbol{\theta}} \right)_i + \lambda_i \mathbf{I} \right)^{-1} \left(\sum_{k=1}^N \left(\frac{\partial \mathbf{y}(\boldsymbol{\theta}, t_k)}{\partial \boldsymbol{\theta}} \right)_i^T (\mathbf{z}(t_k) - (\mathbf{y}(\boldsymbol{\theta}, t_k))_i) \right) \quad (2.19)$$

By adding the term $\lambda_i \mathbf{I}$, the LM algorithm is robust to the singularity of $\sum_{k=1}^N \left(\frac{\partial \mathbf{y}(\boldsymbol{\theta}, t_k)}{\partial \boldsymbol{\theta}} \right)_i^T \left(\frac{\partial \mathbf{y}(\boldsymbol{\theta}, t_k)}{\partial \boldsymbol{\theta}} \right)_i$. Note that a Gauss-Newton step is performed for $\Delta\boldsymbol{\theta}_i$ when $\lambda_i = 0$ while a gradient-descent step is performed under a large value of λ_i . For the implementation of choosing λ_i , the objective costs among the original λ_i , $a\lambda_i$ and $\frac{1}{a}\lambda_i$ ($a < 1$) are compared. What leads to the best cost minimization is chosen to be the final λ_i . In this study, a is chosen to be 0.1.

2.4.2 Box-Constrained Levenberg-Marquardt Algorithm

Although the LM algorithm proves effective in solving ill-conditioned NLSQ, it is only applicable to unconstrained problems. Therefore, a variant of the LM algorithm, BCLM, is proposed in this subsection to enable the LM algorithm to handle parameter constraints while maintaining the robustness of the algorithm. The BCLM has two advantages over the LM algorithm. The first advantage is that the BCLM algorithm avoids the estimate which violate the physical meanings of the parameters. For example, time constants are set all greater than zero such that the solution with the negative time constants are eliminated. Second, the flexibility of the algorithm is improved by allowing the integration of expert knowledge to tighten constraints.

Box-constrained transformation is the key technique that distinguishes the BCLM algorithm from the LM algorithm. The idea behind the BCLM algorithm is to transform the bounded variables into unbounded variables. Then, apply the LM parameter update formula to the unbounded variables. After the parameter update, the unbounded variables are transformed back to the bounded variables. To generalize the constraints defined in (2.12), three types of box constraints are redefined elementwise as follows:

Type I: $\underline{\theta}_i \leq \theta_i \leq \overline{\theta}_i$. A transformation from bounded variables to unbounded variables is shown as follows:

$$\theta_i = F_i(\beta_i) = \frac{\overline{\theta}_i - \underline{\theta}_i}{2} \sin \frac{\pi}{2} \beta_i + \frac{\overline{\theta}_i + \underline{\theta}_i}{2} \quad (2.20)$$

where β_i belongs to \mathbb{R} . Since $\sin \frac{\pi}{2} \beta_i \in [-1, 1]$ for any β_i , θ_i will be always bounded by $[\underline{\theta}_i, \overline{\theta}_i]$. The inverse transformation is written as follows:

$$\beta_i = F_i^{-1}(\theta_i) = \frac{2}{\pi} \sin^{-1} \frac{2\theta_i - (\overline{\theta}_i + \underline{\theta}_i)}{\overline{\theta}_i - \underline{\theta}_i} \quad (2.21)$$

Although the inverse transformation leads to an initial β_i bounded by $[-1, 1]$, it can go freely in \mathbb{R} in the parameter update process.

Type II: $\underline{\theta}_i \leq \theta_i$. The transformation and the inverse transformation are written as follows:

$$\theta_i = F_i(\beta_i) = \underline{\theta}_i - 1 + \sqrt{\beta_i^2 + 1} \quad (2.22)$$

$$\beta_i = F_i^{-1}(\theta_i) = \sqrt{(\theta_i + 1 - \underline{\theta}_i)^2 - 1} \quad (2.23)$$

Type III: $\theta_i \leq \overline{\theta}_i$. The transformation and the inverse transformation are written as follows:

$$\theta_i = F_i(\beta_i) = \overline{\theta}_i + 1 - \sqrt{\beta_i^2 + 1} \quad (2.24)$$

$$\beta_i = F_i^{-1}(\theta_i) = \sqrt{(\overline{\theta}_i + 1 - \theta_i)^2 - 1} \quad (2.25)$$

By substituting $\boldsymbol{\theta} = \mathbf{F}(\boldsymbol{\beta})$, the mapping function from $\boldsymbol{\beta}$ to $\boldsymbol{\Theta}$, into the NLSQ problem (2.9-2.12), one gets the following unconstrained NLSQ problem:

$$\min_{\boldsymbol{\beta}} \mathbf{h}(\mathbf{F}(\boldsymbol{\beta}), t_k) = \min_{\boldsymbol{\beta}} \frac{1}{2} \sum_{k=1}^N (\mathbf{z}(t_k) - \mathbf{y}(\mathbf{F}(\boldsymbol{\beta}), t_k))^T (\mathbf{z}(t_k) - \mathbf{y}(\mathbf{F}(\boldsymbol{\beta}), t_k)) \quad (2.26)$$

$$\dot{\mathbf{x}}(t) = \mathbf{f}[\mathbf{x}(t), \mathbf{u}(t), \mathbf{F}(\boldsymbol{\beta})], \mathbf{x}(t_0) = \mathbf{x}_0 \quad (2.27)$$

$$\mathbf{y}(t) = \mathbf{g}[\mathbf{x}(t), \mathbf{u}(t), \mathbf{F}(\boldsymbol{\beta})] \quad (2.28)$$

Without changing the framework of the LM algorithm, the parameter update formula now updates the unconstrained parameter vector $\boldsymbol{\beta}$ instead of the bounded parameter vector $\boldsymbol{\theta}$ using

$$\Delta \boldsymbol{\beta}_i = \left(\sum_{k=1}^N \left(\frac{\partial \mathbf{y}(\mathbf{F}(\boldsymbol{\beta}), t_k)}{\partial \boldsymbol{\beta}} \right)_i^T \left(\frac{\partial \mathbf{y}(\mathbf{F}(\boldsymbol{\beta}), t_k)}{\partial \boldsymbol{\beta}} \right)_i + \lambda_i \mathbf{I} \right)^{-1} \left(\sum_{k=1}^N \left(\frac{\partial \mathbf{y}(\mathbf{F}(\boldsymbol{\beta}), t_k)}{\partial \boldsymbol{\beta}} \right)_i^T (\mathbf{z}(t_k) - (\mathbf{y}(\mathbf{F}(\boldsymbol{\beta}), t_k)))_i \right) \quad (2.29)$$

According to the chain rule, the gradient of system output response in terms of $\boldsymbol{\beta}$ is written as follows:

$$\left(\frac{\partial \mathbf{y}(\mathbf{F}(\boldsymbol{\beta}), t_k)}{\partial \boldsymbol{\beta}} \right)_i = \left(\frac{\partial \mathbf{y}(\boldsymbol{\theta}, t_k)}{\partial \boldsymbol{\theta}} \right)_i \left(\frac{\partial \mathbf{F}(\boldsymbol{\beta})}{\partial \boldsymbol{\beta}} \right)_i \quad (2.30)$$

where $\left(\frac{\partial \mathbf{y}(\boldsymbol{\theta}, t_k)}{\partial \boldsymbol{\theta}} \right)_i$ is evaluated using (2.16) and $\left(\frac{\partial \mathbf{F}(\boldsymbol{\beta})}{\partial \boldsymbol{\beta}} \right)_i$ is evaluated using the analytical derivatives of $\mathbf{F}(\boldsymbol{\beta})$.

2.4.3 Heuristic Algorithm for Initial Solution Search

As introduced in Section 2.3, the convergence of the local search method is subject to the initial solution, which is difficult to obtain from manufacturer datasheet for small-scale diesel generator. Therefore, a heuristic search algorithm Generalized Opposition-based Learning Genetic Algorithm (GOL-GA) is implemented in this study to conduct a global search within parameter bounds and produce initial solutions for the local search method BCLM.

The fitness function for the GOL-GA is defined as follows:

$$\Gamma(\boldsymbol{\theta}_k) = 1/h(\boldsymbol{\theta}_k) \quad (2.31)$$

where $\boldsymbol{\theta}_k$ is the k th set of $\boldsymbol{\theta}$, and is also the k th chromosome in the population. The Selection operation is standard in the GA algorithm and determines based on the fitness level which chromosomes are the parent solutions for the Cross operation. The Crossover operation, which is used to generate new $\boldsymbol{\theta}$ using the parent solutions, is expressed as follows:

$$\theta_{k,i}^{new} = (1 - \lambda)\theta_{k,i} + \lambda\theta_{l,i} \quad (2.32a)$$

$$\theta_{l,i}^{new} = \lambda\theta_{k,i} + (1 - \lambda)\theta_{l,i} \quad (2.33b)$$

where $\theta_{k,i}$ and $\theta_{l,i}$ are the i th parameter of two parent solutions, $\boldsymbol{\theta}_k$ and $\boldsymbol{\theta}_l$, respectively; $\theta_{k,i}^{new}$ and $\theta_{l,i}^{new}$ are the i th parameter of the new solutions, respectively; λ is a random real number within $[0, 1]$. The Mutation operation, which transforms the low-fitness solutions into new solutions using the GOL scheme [52]:

$$\theta_{m,i}^{new} = \begin{cases} \lambda(l_i^d + u_i^d) - \theta_{m,i}, & \text{if } \theta_{m,i}^{new} \in [l_i^d, u_i^d] \\ \text{rand}(l_i^d, u_i^d), & \text{if } \theta_{m,i}^{new} \notin [l_i^d, u_i^d] \end{cases} \quad (2.34)$$

$$l_i^d = \min_{m \in P}(\theta_{m,i}), u_i^d = \max_{m \in P}(\theta_{m,i}) \quad (2.35)$$

where l_i^d and u_i^d are the minimum and maximum of the i th parameter in the population P .

The best solution generated by GOL-GA is used as the initial solution $\boldsymbol{\theta}_0$ for the BCLM algorithm. The BCLM algorithm is then applied to conduct a local search using the parameter update formula (2.29).

2.4.4 Overview of Model Parameterization Method

Figure 2.4 shows the flowchart of the proposed model parameterization method using the H-BCLM algorithm, where the steps in bold mean that they involve running the diesel generator dynamic model. The diesel generator dynamic model consists of two types of

mathematical equations: state equations that include differential equations (2.1), (2.3), and (2.5), and observation equations that relate state variables to output response. The input profile for running the dynamic model is the load step profile, which is consistent with the load-step-change tests conducted in the field. A fourth order Runge-Kutta method is used as the numerical simulation technique. The stopping criteria for both GOL-GA and BCLM consist of: (a) the iteration number reaches the maximum limit and (b) the relative cost difference reaches the threshold, such as $|(h_i - h_{i-1})/h_i| \leq 10^{-6}$.

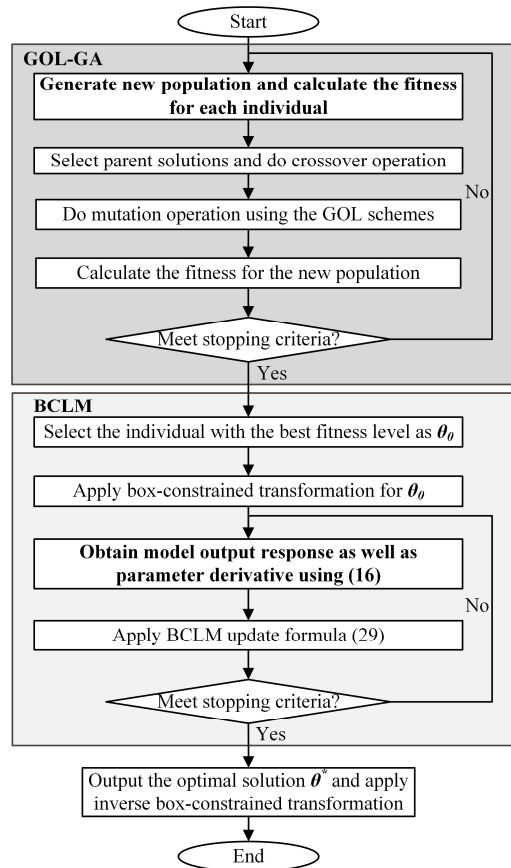


Figure 2.4. Schematic of the proposed model parameterization method

As shown in Figure 2.4, it is noted that transformation and inverse transformation techniques are only applied once before and after the BCLM iteration. The transformation maps all the parameters with box constraints to an unconstrained solution space before the parameter update. The inverse transformation is applied to map the solution from the

unconstrained space back to the original space. By doing so, the BCLM method is able to handle parameters with bounds without changing the LM algorithm structure. The obtained solutions are guaranteed to fulfill the original constrained NLSQ problem [59].

2.5 Case Studies

This section presents two case studies to demonstrate the effectiveness of the proposed model parameterization method. First, the H-BCLM algorithm is tested against a diesel generator model with known parameters. Then, field testing measurements are used to validate the H-BCLM algorithm.

2.5.1 Benchmark Case

The benchmark case tests the effectiveness of the H-BCLM algorithm, along with both LM and BCLM algorithms, against a diesel generator model with known parameters. The 50kVA, 400V diesel generator model is developed in MATLAB/Simulink®. The actual parameter values listed in Table 2.2 are selected based on a combination of online sources and the Simulink® preset model for synchronous machines. The fixed parameters contain all the reference values, which are at 1.0 p.u. All the machine reactances have the initial estimates from manufacturer datasheet with tight bounds, shown in Table 2.2. Two load-step-change tests are conducted: a load step-up test from 30% to 80% of the rated power, and a load step-down test from 80% to 30%. The frequency and voltage measurements at the generator terminal are the input to the H-BCLM algorithm.

Four cases are presented in Table 2.2. From Case 1 to 3, different initial estimates are considered for both LM and BCLM algorithms while in Case 4, the H-BCLM algorithm is applied without initial estimates. Case 1 considers "reasonable" initial estimates, which are set five times as the true values. Case 2 and Case 3 consider "unreasonable" initial estimates,

which are selected to be no less than twice as the true values, and more than half of which are more than ten times of the true values. The prior knowledge is converted into parameter bounds as box constraints that are listed in Table 2.2 considering: 1) all the control gains are larger than 0; 2) the friction factor and the stator resistance are larger than 0; 3) all the time constants are larger than 0; and 4) the constraints for the inertia constant are set based on the generator rated capacity.

The final estimates are also shown in Table 2.2. In Case 1, all the parameters converge to the exact actual values using both the LM algorithm and the BCLM algorithm. With less accurate initial estimates than Case 1, it can be observed in Case 2 that the LM algorithm performs poorly and fails to accurately estimate the parameters. Diesel engine time constants T_1 and T_3 , and friction factor D_f reach infeasible ranges. Unlike the LM method, the estimated parameters converge to the actual values using the BCLM algorithm in Case 2 after the constraints are imposed. In Case 3, diesel engine time constants T_1 and T_2 , friction factor D_f and inertia constant H end with impractical estimates using the LM algorithm. Meanwhile, the BCLM algorithm fails to obtain the global optimal solution, indicating the initial solution is far away from the optimum.

Table 2.2. Diesel generator benchmark model parameters and test results

Symbol	m	T_1	T_2	T_3	T_V	K_V	K_{pe}	K_{ie}	H	D_f	T'_{do}	R_s	
Quantity	40	0.025	0.009	0.038	0.05	2	5	10	0.074	0.020	1.16	0.04	
Lower Bounds	0	0	0	0	0	0	0	0	0.05	0	0	0	
Upper Bounds	Inf	0.5	0.5	0.5	0.5	Inf	Inf	Inf	0.15	Inf	Inf	Inf	
Case 1	Init	120	0.125	0.045	0.19	0.25	10	25	50	0.14	0.1	5	0.2
	LM	40	0.025	0.009	0.038	0.05	2	5	10	0.074	0.020	1.16	0.04
	BCLM	40	0.025	0.009	0.038	0.05	2	5	10	0.074	0.020	1.16	0.04
Case 2	Init	80	0.25	0.09	0.4	0.5	20	50	100	0.14	0.2	2.3	0.4
	LM	104	-5672	0.012	-14689	0.05	3.5	2.9	5.7	0.088	-0.59	1.16	0.04
	BCLM	40	0.025	0.009	0.038	0.05	4.1	2.4	4.8	0.074	0.020	1.16	0.04
Case 3	Init	400	0.25	0.09	0.4	0.5	20	50	100	0.14	0.2	5	0.4
	LM	0.44	0.002	20.01	20.01	0.76	13	17	80.8	0	0	0.56	0.45
	BCLM	300	0.006	0.399	0.490	0.05	2.8	3.6	7.2	0.071	4765	1.16	0.04
Case 4	H-BCLM	40	0.025	0.009	0.038	0.05	2	5	10	0.074	0.020	1.16	0.04

a. Machine reactance initial estimates are: $X_d = 3.79$, $X_q = 2.12$, $X'_d = 0.342$.

The parameter estimation convergence for Case 4 is shown in Figure 2.5, 2.6 and 2.7. Without prior estimates, all the parameters converge to the actual values using the H-BCLM algorithm. The heuristic algorithm GOL-GA and the BCLM algorithm are color-coded to show both global and local search process.

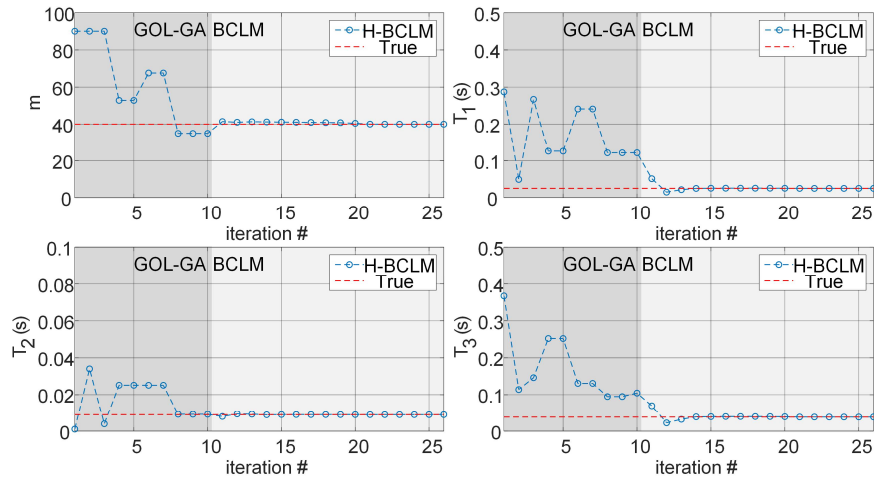


Figure 2.5. Diesel engine parameter convergence in Case 4

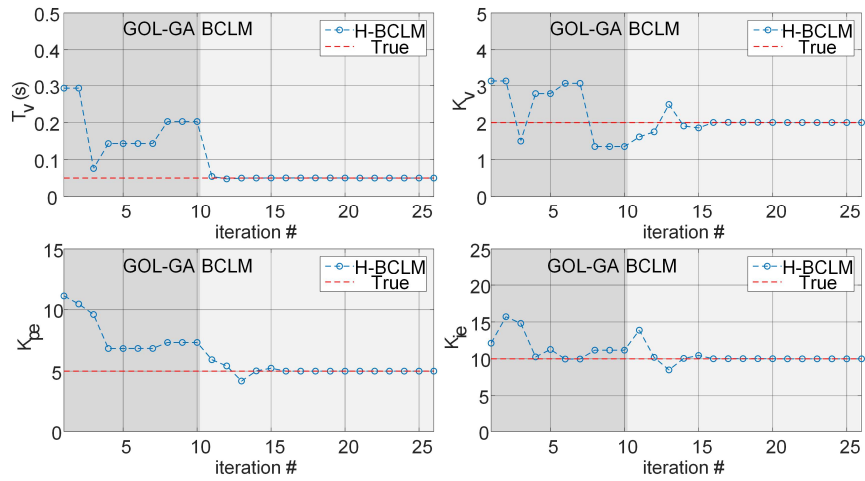


Figure 2.6. Excitation system parameter convergence in Case 4

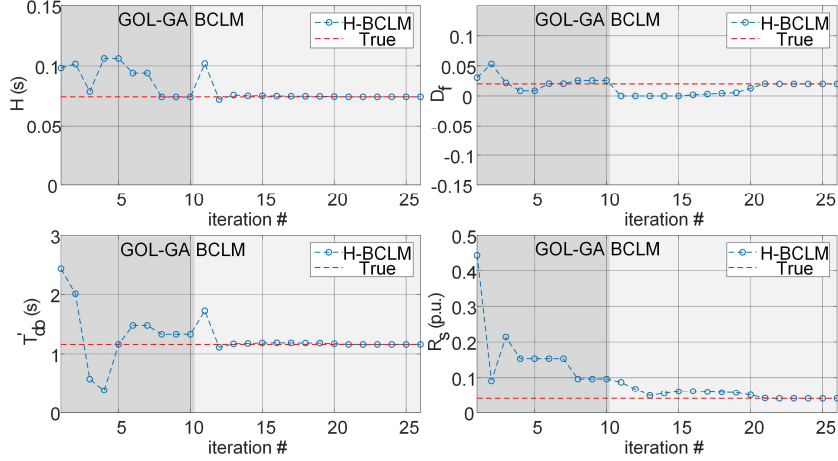


Figure 2.7. Synchronous generator parameter convergence in Case 4

Overall, the BCLM algorithm shows good performance and robustness in accurately estimating the parameters over the LM algorithm. By incorporating the prior knowledge into the BCLM algorithm, the solution space is reduced, and any infeasible estimate is eliminated. However, both algorithms are subject to initial solution selection. The H-BCLM algorithm is successful in obtaining the optimum regardless of initial solutions.

2.5.2 Model Parameterization for a Small Diesel Generator

The second case provides validation results for matching field measurements from an actual 16-kVA diesel generator. The load-step-change tests for the diesel generator are done using an electric load emulator. A high-resolution digital recorder is installed at the terminal of the diesel generator to record the three-phase output voltage and current, with the sampling frequency of 1kHz. The raw data is post-processed using low-pass filters, which are used for filtering out the high-frequency measurement noise, and phase-locked loops, which are applied to extract the dynamics of frequency and voltage magnitude.

The effectiveness of H-BCLM is compared to three algorithms, which were selected from literature review: 1) constrained Gauss-Newton with linear search (CGN-LS) [48] and [56]; 2) state-of-the-art TRR [50]; and 3) state-of-the-art DPSO-LS [52]. Performance comparison is

provided under the same parameter bounds and stopping criteria. Like the benchmark case in Section 2.5.1, the machine reactance is tightly bounded with the initial estimates from the manufacturer datasheet.

The extracted solutions from the field data are provided in Table 2.3 as well as the accuracy in terms of matching the filed measurement. The CGN-LS experiences divergence issues. With the limited measurement points, the diesel generator model parameterization can be an ill-conditioned NLSQ problem, leading to an invalid Gauss-Newton step. The left matrix for the Gauss-Newton step (2.17) is computed in this case and a zero eigenvalue is obtained as follows to validate the rank-deficiency of the matrix:

$$\begin{aligned} & eig \left[\sum_{k=1}^N \left(\frac{\partial \mathbf{y}(\boldsymbol{\theta}, t_k)}{\partial \boldsymbol{\theta}} \right)_i^T \left(\frac{\partial \mathbf{y}(\boldsymbol{\theta}, t_k)}{\partial \boldsymbol{\theta}} \right)_i \right] \\ & = [1.15e^8 \quad 1.81e^7 \quad 4.75e^6 \quad 3.23e^6 \quad 1.06e^6 \quad 2.23e^5 \quad 1.55e^5 \\ & \quad \quad \quad 4.00e^3 \quad 284.81 \quad 2.52 \quad -1.19e^{-12}] \end{aligned}$$

Figure 2.8 and Figure 2.9 show the fitted frequency and voltage responses using H-BCLM and another two algorithms. While all the algorithms capture the steady-state responses correctly, they result in different levels of agreement with the dynamics observed in the field measurements. The TRR shows decent performance in capturing voltage dynamics while performing poorly in matching frequency dynamics. The cause for the poor performance is similar to BCLM in Section 2.5.1, that is, the TRR algorithm itself is a local search algorithm whose performance is highly dependent on the selection of initial solutions. However, the DPSO-LS performs the opposite way, leading to a small deviation in matching frequency dynamics and a large deviation of matching voltage dynamics. The reason why DPSO-LS exhibits degraded performance is that it is still a pure heuristic algorithm that ignores gradient information for the dynamic system even though a similar GOL is utilized.

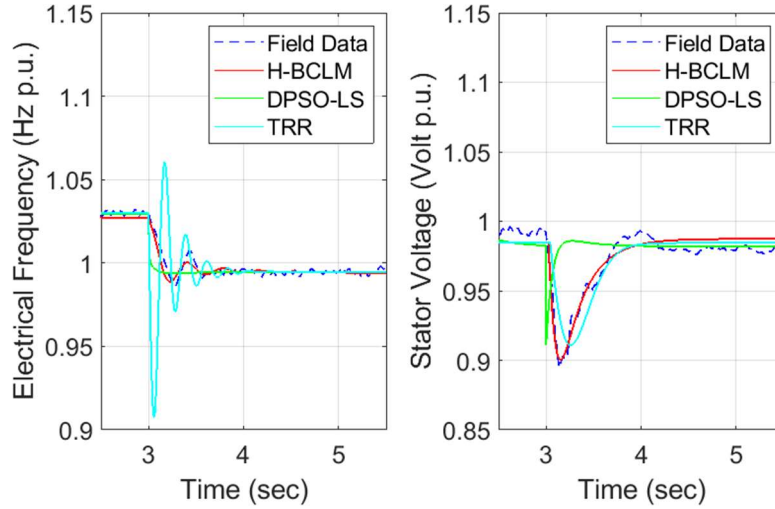


Figure 2.8. Optimal fit for load step-up test

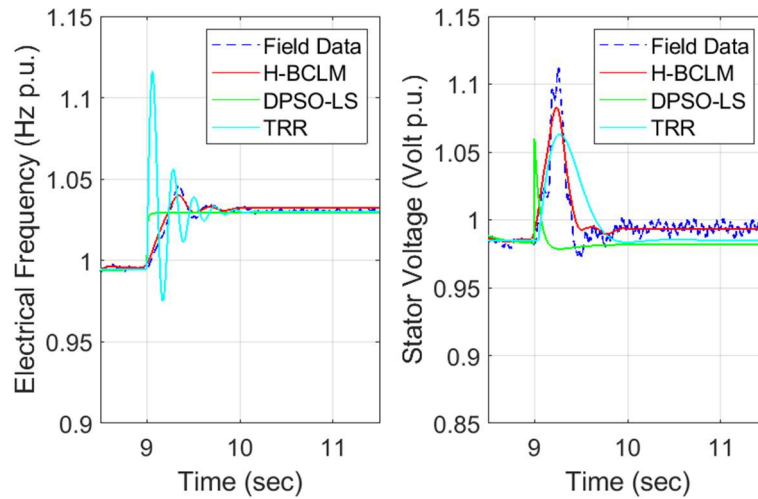


Figure 2.9. Optimal fit for load step-down test

Among all, the H-BCLM algorithm performs the best and generates a high-quality solution that fits both frequency and voltage responses. The small difference between model response and field measurement is mainly due to the simplification of the model structure and the lack of information on the measurement filters.

Table 2.3. Extracted parameters of diesel generator model

Estimated Parameters	CGN-LS	TRR	DPSO-LS	H-BCLM
m		15.838	19.042	15.479
T_1		0.042	0.164	1.494
T_2		0.119	0.0008	0.001
T_3		0.038	0.166	1.486
T_V		0.076	0.0001	0.056
K_V	Solution	0.882	20.201	0.491
K_{pe}	Divergence	7.042	5.165	16.462
K_{ie}		22.437	16.470	56.847
H		0.086	0.057	0.150
D_f		0.019	0.186	0.230
T'_{do}		0.978	4.792	0.837
R_s		0.137	0.354	0.094
RMSE _f	NAN	0.0183	0.0060	0.0025
RMSE _V	NAN	0.0144	0.0268	0.0076

2.6 Conclusion

In this study, a robust H-BCLM algorithm is proposed to parameterize the nonlinear diesel generator model for microgrid dynamic simulation. The uniqueness of the proposed method is three-fold. First, the approach enables one to simultaneously generate a complete set of diesel generator model parameters without the need of knowing any initial estimate. Second, the H-BCLM algorithm improves the quality of the solutions by allowing the integration of expert knowledge and eliminating the solutions with no physical meanings. Last but not least, the H-BCLM algorithm offers a robust approach to address the diesel generator model parameterization problem, which is identified as an ill-conditioned NLSQ problem considering only load-step-change tests with limited measurement points. Compared with three existing state-of-the-art algorithms, the proposed H-BCLM algorithm always converges and reduces the matching errors by 50%. Future work will focus on applying the method to other applications such as solar and battery inverters.

CHAPTER 3. A NEW DISTRIBUTED VOLTAGE CONTROLLER FOR ENABLING VOLT-VAR SUPPORT OF MICROGRIDS IN GRID-CONNECTED OPERATION

This chapter proposes a new proportional voltage controller for microgrids to allow microgrids to provide voltage support for distribution systems with the assumption that the DERs are aggregated in the form of microgrids. In this chapter, Section 3.1 firstly summarizes the existing literature on voltage support provided by microgrids in distribution systems. The design of the controller is proposed in Section 3.2. The small-signal analysis of a closed-loop system model is performed in Section 3.3 to assess the performance of the proposed controller, as regard to stability, steady-state response and transient response. In Section 3.4, the controller is validated in MATLAB/Simulink using single microgrid and multi-microgrid case studies. The conclusion is given in Section 3.5.

3.1 Literature Review

Many researchers have proposed the converter control design for the application of grid voltage support. A droop control design is presented in [60] for a single-phase PV converter, which is operated as the grid-supporting converter with voltage-controlled mode. The proposed converter control can automatically compensate reactive power in case of a grid voltage sag. In [61], an ESS is acting as the main source in the microgrid for mitigating system voltage fluctuations. The power converter of the ESS is controlled as the grid-supporting converter with CCM, and the Volt-Var control is used for generating the reactive power reference for the current control loop of the converter. However, both papers focus on the control design and analysis on single component operation. The parallel operation of multiple DERs is not discussed concerning coordination strategy as well as potential interaction and stability issues.

A coordinated control method for distributed ESSs can be found in [62] for voltage regulation. Among distributed ESSs, a consensus algorithm is applied to determine the utilization ratio for each ESS. Then a local control is implemented to adjust the charging/discharging speed of each ESS based on its SOC. Although the paper considers PV, ESS and load as one control unit, only real power dispatch of ESSs is discussed for regulating voltage. How to utilize reactive power capacity of PV and ESS converter is not mentioned. Besides, this setup is impractical when the real power of ESSs is dispatched only based on economic decisions instead of responding to voltage disturbances. The voltage regulation of microgrids is discussed in [63] under the context of the integration of DC microgrids into the AC grid. A grid-supporting converter is used as the interface between the AC grid and DC microgrid that consists of the DERs and the loads. The Volt-Var droop control is utilized to emulate the excitation system of the synchronous machines, providing voltage regulation to the AC grid. To date, little research has addressed how to enable AC microgrids that consist of multiple DERs to participate in the voltage support of distribution systems. Another two main issues also need to be addressed: 1) how to coordinate reactive power output of multiple DERs in the microgrid zone for grid voltage support; 2) whether there is any potential interaction among multiple DERs in the microgrid under the control.

Inspired by Volt-Var droop control, which is a localized proportional voltage control strategy for inverter-based DERs, a new proportional voltage controller is proposed in this paper to enable grid-connected microgrids to provide voltage regulation at the point of common coupling (PCC) in a similar way as smart inverter local Volt-Var control. The distributed version of the proportional voltage controller is developed using the distributed averaging algorithm such that multiple DERs within a microgrid are coordinated concerning

reactive power capacity. The proposed control is referred to as distributed proportional voltage control (**DPVC**). It is also shown in the paper that the DPVC supports multi-microgrid architecture in a distribution system.

3.2 Secondary Voltage Controller Design

This section firstly introduces a new proportional voltage controller design that enables microgrids to be involved in voltage support of distribution systems. Then a distributed version of the proportional voltage controller called DPVC is proposed based on the continuous-time distributed averaging algorithm.

3.2.1 Proportional Voltage Controller Design

Figure 3.1 shows a typical radial feeder with each microgrid being connected to each bus via a feeder section. Each microgrid consists of a PV system, an ESS and a local load that represents the microgrid customers. There are also conventional loads at each bus that are beyond the microgrid area. Note that the proposed design and analysis still hold in no need of modification when each microgrid has a different microgrid design, such as the number or the capacity of DERs.

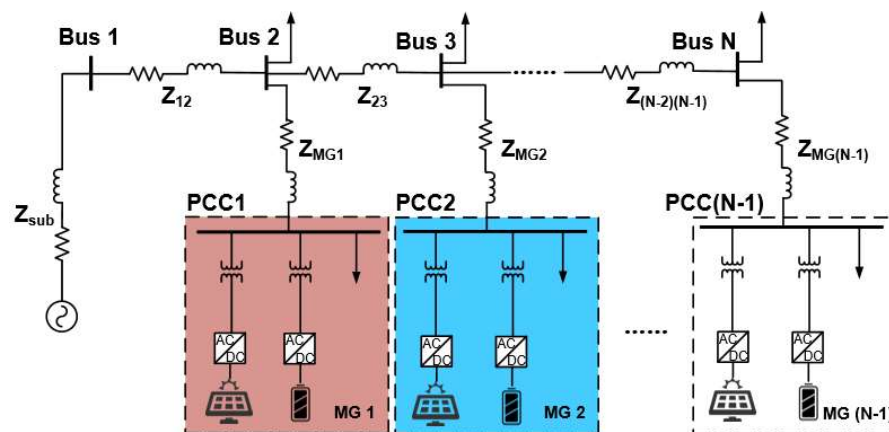


Figure 3.1. Radial distribution feeder with interconnection of microgrids

We now introduce such secondary voltage controllers that are based on the primary control of grid-support converters. As mentioned in Section 1.4, in the grid-connected mode, real and

reactive power control at the primary level are achieved by the PI controllers which drive the error between the reference and the measurement to zero. Therefore, at the secondary level, we assume the DERs eventually follow their power references with some time constant τ . This assumption might simplify the voltage and current control loops of power converters, but it is valid for the secondary level control due to timescale separation between primary and secondary control. A first-order transfer function is used to represent reactive power dynamics of PV and ESS:

$$Q_{PV}(s) = G_{PV}(s)Q_{PV_ref}(s) = \frac{1}{\tau_{PV}s+1}Q_{PV_ref}(s) \quad (3.1)$$

$$Q_{ESS}(s) = G_{ESS}(s)Q_{ESS_ref}(s) = \frac{1}{\tau_{ESS}s+1}Q_{ESS_ref}(s) \quad (3.2)$$

where $Q_{PV}(s)$, $Q_{PV_ref}(s)$ are reactive power output and reference of the PV system in s-domain and $Q_{ESS}(s)$ and $Q_{ESS_ref}(s)$ are reactive power output and reference of the ESS system in s-domain; τ_{PV} and τ_{ESS} are the time constant of reactive power loops for PV and ESS.

The objective of the proportional voltage controller is to enable microgrids to regulate voltage at microgrid PCC based on the proportional setting, which is similar to the Volt-Var setting of smart inverters. To achieve this, the proposed proportional voltage controller is formulated as

$$k \frac{d\Omega}{dt} = -d(V_d - V^*) - (Q - Q^*) \quad (3.3)$$

where k is the voltage controller gain and Ω is the voltage control variable for DER reactive power injection; d is the proportional gain that determines the Volt-Var response at microgrid PCC; V_{PCC} and V^* are microgrid PCC voltage magnitude and microgrid PCC nominal voltage; Q_{PCC} and Q^* are reactive power measurement and nominal reactive power flow in

three phases at microgrid PCC. $Q_{PCC} > 0$ refers to reactive power injection while $Q_{PCC} < 0$ refers to reactive power absorption.

The proposed proportional voltage controller has an equilibrium point when the reactive power flows at microgrid PCC and microgrid PCC voltage follows a proportional relationship defined by the proportional gain d , similar to the one for smart inverter Volt-Var curve slope settings. Therefore, when the microgrid PCC voltage is higher than the nominal point V^* , the right-hand side of (3.3) is less than zero; in this case, the voltage control variable decreases such that reactive power injection at PCC will also decrease until the right-hand-side of (3.3) reaches zero. Another situation is when the microgrid PCC voltage is lower than the nominal point V^* and the right-hand side of (3.3) is greater than zero. Given $d\Omega/dt > 0$, the reactive power injection at microgrid PCC will increase to provide voltage support until the controller reaches steady-state. Note that if $Q^* = 0$, the microgrid will absorb or inject reactive power depending on whether the microgrid PCC voltage is greater or lower than the nominal voltage, respectively.

The voltage control variable is directly applied to the reactive power output of the DERs inside the microgrid. To coordinate reactive power sharing among PV and ESS, the participation factor is used:

$$\begin{cases} Q_{PV_r} &= \sigma_1 \Omega \\ Q_{ESS_r} &= \sigma_2 \Omega \end{cases} \quad (3.4)$$

where $Q_{PV_{ref}}$ and σ_1 are the reactive power reference and the participation factor for PV in the microgrid zone; $Q_{ESS_{ref}}$ and σ_2 are the reactive power reference and the participation factor for ESS in the microgrid zone. Since the secondary voltage controller is assumed to be part of the microgrid centralized controller, the participation factor is calculated centrally based on the available Var capacity of DERs

$$\begin{cases} Q_{PV_avail} = \sqrt{S_{PV}^2 - P_{PV}^2} \\ Q_{ESS_avail} = \sqrt{S_{ESS}^2 - P_{ESS}^2} \end{cases} \quad (3.5)$$

$$\begin{cases} \sigma_1 = \frac{Q_{PV_avail}}{Q_{PV_avail} + Q_{ESS_avail}} \\ \sigma_2 = \frac{Q_{ESS_avail}}{Q_{PV_avail} + Q_{ESS_avail}} \end{cases} \quad (3.6)$$

where Q_{PV_avail} , S_{PV} and P_{PV} are the available Var capacity, the inverter apparent power rating and real power output for PV; Q_{ESS_avail} , S_{ESS} and P_{ESS} are the available Var capacity, the inverter apparent power rating and real power output for ESS. However, since the centralized method is vulnerable to a single point of failure, the next subsection describes a distributed method to achieve the same control objective.

3.2.2 Distributed Implementation of Proportional Voltage Control

In order to increase the flexibility and to distribute the computation of the proportional voltage controller described in Section II-A, the DPVC is implemented at each DER, which receives settings from upper-level control and measurements from microgrid PCC, as shown in Figure 3.2. The reactive power coordination among multiple DERs is achieved within the microgrid using the continuous-time distributed averaging algorithm [64].

Continuous-time distributed averaging is a dynamic process that coordinates networks of agents until certain quantities of interest are agreed upon among the agents [65]. This process can be described using

$$\dot{x}_i = -\sum_{j=1}^n b_{ij}(x_i - x_j) \quad (3.7)$$

where x_i and x_j are the variables for the i th and the j th agents in the network; b_{ij} is the weighted communication link between the i th and the j th agents. A convention is set up that $b_{ij} = b_{ji} > 0$ means the communication between the i th and the j th agents exists and is bidirectional, and $b_{ij} = b_{ji} = 0$ means no direct communication link between the i th and the

j th agents. This dynamic process eventually results in a common value across all the agents, and the common value is the weighted sum of the neighboring variables.

The distributed averaging algorithm is first applied to microgrid control in [64] to achieve reactive power sharing in islanded microgrids. In this study, the algorithm is integrated with the proposed proportional voltage control to achieve reactive power sharing among multiple DERs in a distributed manner. The DPVC is defined as

$$\begin{cases} k_i \frac{d\Omega_i}{dt} = -d(V_{PCC} - V^*) - (Q_{PCC} - Q^*) - \gamma_i \\ \gamma_i = \sum_{j=1}^n b_{ij} \left(\frac{Q_i}{Q_{i_{avail}}} - \frac{Q_j}{Q_{j_{avail}}} \right) \end{cases} \quad (3.8)$$

where k_i and Ω_i are the DPVC control gain and DPVC control variable for DER i ; d is the DPVC proportional gain; b_{ij} is the communication link between DER i and DER j ; Q_i , $Q_{i_{avail}}$, Q_j and $Q_{j_{avail}}$ are the reactive power output and available reactive power capacity for DER i and DER j , respectively. The DPVC achieves a Volt-Var proportional characteristic at microgrid PCC while maintaining reactive power sharing among DERs within the microgrid zone.

The secondary controller gain k determines the convergence speed of the controller. The transient performance and stability analysis associated with this parameter k are introduced in the next section. The secondary proportional control gain d specifies the local Volt-Var characteristic of the microgrid at PCC. The proportional gain of the secondary controller is considered to be coordinated by DSO via tertiary control, such as a VVO algorithm based on load and renewable forecast. The proportional gain selection can be dependent on network information, the location of the microgrids and other voltage control devices in the distribution system. Since the secondary control allows the microgrid to operate like a smart inverter at

microgrid PCC, it can support multi-microgrid architecture. The small-signal stability analysis for multi-microgrid is described in the next section.

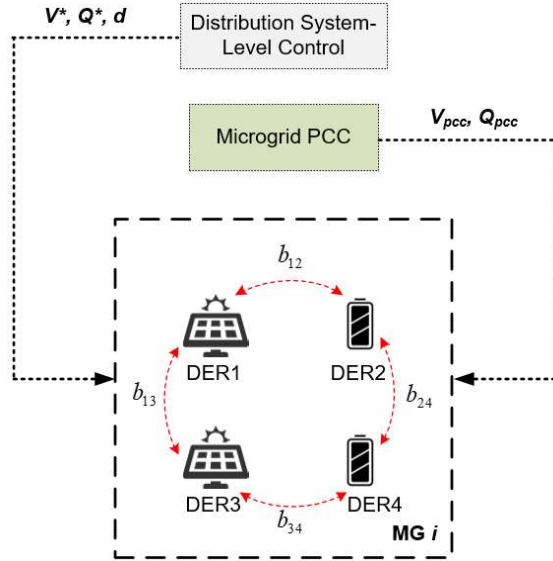


Figure 3.2. Schematic of DPVC control architecture

3.3 Small Signal Analysis

In this section, the large-signal model of the closed-loop system is derived to study the effects of the control parameters on system stability and dynamic performance. To avoid bringing in a complicated power electronics model, a first-order transfer function is introduced to model reactive power control loops of the DER. This assumption is valid in this study for two reasons. First, the reactive power of the DER in the grid-connected operation is regulated by a PI control to eliminate the steady-state reactive power tracking error [66]. Besides, there is timescale separation between primary control level (i.e. within a second) and secondary control level (i.e. seconds to minutes) of the DER [64] and [67].

The vector form of the closed-loop system is written as

$$k\dot{\Omega} = I_{m \times 1}(-dV_{PCC} + dV^* - Q_{PCC} + Q^*) - LQ_{avail}^{-1}Q \quad (3.9)$$

$$\tau\dot{Q} = -Q + \Omega \quad (3.10)$$

$$Q_{PCC} = \mathbf{I}_{1 \times m} \mathbf{Q} - Q_{load} \quad (3.11)$$

$$V_{PCC} = \frac{\partial V_{PCC}}{\partial Q_{PCC}} Q_{PCC} + \bar{V}_{PCC} \quad (3.12)$$

where $\boldsymbol{\Omega}$ and \mathbf{Q} are the vectors of DPVC control variables and DER reactive power output; $\mathbf{I}_{m \times 1}$ is the m-dimensional column vector of one. \mathbf{k} , $\boldsymbol{\tau}$ and \mathbf{Q}_{avail} are diagonal matrices of DPVC control gains, time constants of reactive power control loops and available reactive power capacity; m is the number of DERs inside the microgrid; $\mathbf{L} = \mathbf{diag}(\sum_{j=1}^n b_{ij}) - \mathbf{B}$ and \mathbf{B} is the matrix of b_{ij} ; Q_{load} is a scalar value representing the aggregated microgrid load. $\partial V_{PCC} / \partial Q_{PCC}$ is the sensitivity factor of reactive power flow at microgrid PCC to microgrid PCC voltage magnitude; \bar{V}_{PCC} is microgrid PCC voltage without additional reactive power support from the microgrid. (3.11) is derived by assuming negligible loss inside the microgrid zone. (3.12) describes the relationship between microgrid PCC voltage and real/reactive power injection at any bus in the system. The details of (3.12) are found in [20].

Inserting (3.11) and (3.12) into (3.9), the system equation becomes

$$\begin{bmatrix} \dot{\boldsymbol{\Omega}} \\ \dot{\mathbf{Q}} \end{bmatrix} = \mathbf{A} \begin{bmatrix} \boldsymbol{\Omega} \\ \mathbf{Q} \end{bmatrix} + \mathbf{B}_d \boldsymbol{\epsilon} + \mathbf{C} \quad (3.13)$$

where $\beta = d \frac{\partial V_{PCC}}{\partial Q_{PCC}} + 1$, $\boldsymbol{\epsilon} = [\bar{V}_{PCC} \quad Q_{load}]^T$, and

$$\mathbf{A} = \begin{bmatrix} \mathbf{0}_{m \times m} & -\mathbf{k}^{-1}(\beta \times \mathbf{1}_{m \times m} + \mathbf{L} \mathbf{Q}_{avail}^{-1}) \\ \boldsymbol{\tau}^{-1} & -\boldsymbol{\tau}^{-1} \end{bmatrix},$$

$$\mathbf{B}_d = \begin{bmatrix} -d \times \mathbf{k}^{-1} \mathbf{I}_{m \times 1} & \beta \times \mathbf{k}^{-1} \mathbf{I}_{m \times 1} \\ \mathbf{0}_{m \times 1} & \mathbf{0}_{m \times 1} \end{bmatrix},$$

$$\mathbf{C} = \begin{bmatrix} (dV^* + Q^*) \times \mathbf{k}^{-1} \mathbf{I}_{m \times 1} \\ \mathbf{0}_{m \times 1} \end{bmatrix},$$

where $\mathbf{0}_{m \times m}$ and $\mathbf{1}_{m \times m}$ are the $m \times m$ all-zero matrix and all-one matrix; $\mathbf{0}_{m \times 1}$ is the m -dimensional column vector of zeros. The characteristic equation of the closed-loop system (3.13) is $\det(\lambda \mathbf{I}_{2m \times 2m} - \mathbf{A}) = 0$. Expansion of \mathbf{A} yields

$$\det \left(\begin{bmatrix} \lambda \mathbf{I}_{m \times m} & \mathbf{k}^{-1}(\beta \times \mathbf{1}_{m \times m} + \mathbf{LQ}_{avail}^{-1}) \\ -\boldsymbol{\tau}^{-1} & \lambda \mathbf{I}_{m \times m} + \boldsymbol{\tau}^{-1} \end{bmatrix} \right) = 0 \quad (3.14)$$

Since these two diagonal matrices $-\boldsymbol{\tau}^{-1}$ and $\lambda \mathbf{I}_{m \times m} + \boldsymbol{\tau}^{-1}$ commute and all the block matrices are square matrices of size m , (3.14) is further reduced to the form

$$\det(\lambda^2 \mathbf{I}_{m \times m} + \lambda \boldsymbol{\tau}^{-1} + \mathbf{k}^{-1}(\beta \times \mathbf{1}_{m \times m} + \mathbf{LQ}_{avail}^{-1})\boldsymbol{\tau}^{-1}) = 0 \quad (3.15)$$

The stability of the system is ensured if the solutions of (3.15) are all located in the left-half complex plane.

To study the impact of different control parameters on the dynamic performance of the closed-loop system, a case study with two DERs is considered with the system parameters listed in Table 3.1. The eigenvalues of the closed-loop system are displayed in Figure 3.3 as the black cross, with their changing direction shown as the gains increase. The closed-loop system has two pairs of eigenvalues (four in total). As Figure 3.3 shows, the increase of DPVC control gain k leads to a larger damping ratio and eventually an overdamped response. Increasing DPVC proportional gain d results in an increasingly underdamped response for one pair of eigenvalues which are not affected by the increase of the weight of communication links. Oppositely, the communication link weight does decrease the damping ratio for another pair of eigenvalues which are not impacted as the DPVC proportional gain d increases.

With respect to the settling time of the closed-loop system, Figure 3.3 shows that tuning of other parameters such as the DPVC proportional gain and communication weights hardly leads to a faster control response. However, an inappropriate selection of DPVC control gains k can cause a sufficiently slow control response. Figure 3.4 indicates that the closed-loop system has

the settling time in relation to the time constant of reactive power control loops of the DERs. If the reactive power control loops have smaller time constants and faster response, the response of the closed-loop system converges to a steady-state point more quickly. One will have the same observation in a more general case where there are more than 2 DERs within the microgrid, by plotting the eigenvalues of (3.15).

Table 3.1. Control parameters

Parameter	Symbol	Value
DER1 time constant	τ_1	2 s
DER2 time constant	τ_2	2 s
Initial DPVC control gain for DER1	k_1	0.2
Initial DPVC control gain for DER2	k_2	0.2
Initial DPVC proportional gain	d	10
Weight of communication link between DER1 and DER2	b_{12} (or b_{21})	1
Sensitivity factor	$\frac{\partial V_{PCC}}{\partial Q_{PCC}}$	0.0106 Vp.u./Qp.u.

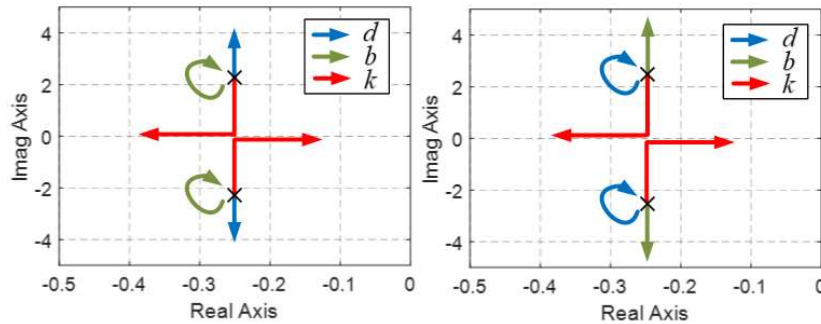


Figure 3.3. Eigenvalue traces of closed-loop systems with the increment of control parameters

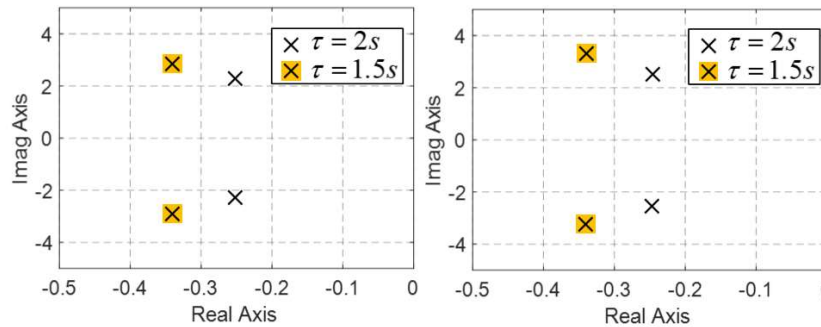


Figure 3.4. Eigenvalues of closed-loop systems with different time constants of reactive power control loops

3.4 Simulation Results

In order to demonstrate the effectiveness of the proposed DPVC, a 5-bus distribution test system is set up, consisting of two grid-connected microgrids MG1 and MG2. Each microgrid is under the operation of its own DPVC. The schematic of the test system is shown in Figure 3.1 with $N = 3$. The control parameters for each microgrid are the same as is in Table 3.1 except that all the DPVC control gains k are selected to be 2.0 to avoid large overshoot. The test system parameters are included in Table 3.2. Two microgrids have the identical configuration: one PV system, one ESS system, and an aggregated load. Each DER within the microgrid footprint is connected to the distribution system via a distribution transformer. Two aggregated non-microgrid loads are included to represent loads at other locations of the distribution system. The line impedance and the source impedance are chosen based on distribution circuit parameters from a real-world utility. The test system is built using Simscape Electrical™ where all the DER models and power converter models are developed with their control design.

Table 3.2. Test system parameters

Parameter	Symbol	Value
Base Voltage	V_{base}	11.0 kV
Base Apparent Power	S_{base}	100 MVA
Base Impedance	Z_{base}	1.21 Ω
Transformer Capacity	S_t	1 MVA
Transformer Impedance	Z_t	0.000575 p.u.
Transformer X/R Ratio	X/R	6
PV System Rated Capacity in MG1 and MG2	P_{PV_MG}	1 MW/1 MVA ^a
ESS System Rated Capacity in MG1 and MG2	P_{ESS_MG}	1 MW/1 MVA
Aggregated Load Peak in MG1 and MG2	P_{LOAD_MG}	1 MW
Non-Microgrid Aggregated Load	P_{LOAD}	0.8 MW
Substation Impedance	Z_{sub}	0.0075 + j0.1851 p.u.
Line Impedance (Bus 1, Bus 2)	Z_{12}	0.4111 + j0.7046 p.u.
Line Impedance (Bus 2, Bus 3)	Z_{23}	0.1351 + j0.1618 p.u.
Line Impedance (Bus 2, PCC 1)	Z_{MG1}	0.0258 + j0.0308 p.u.
Line Impedance (Bus 3, PCC 2)	Z_{MG2}	0.0078 + j0.0095 p.u.

a. 1 MW/1 MVA represents the maximum real power capacity and inverter apparent power capacity

3.4.1 Voltage Regulation and Reactive Power Sharing

The case study in this subsection demonstrates the performance of the DPVC in (3.8) on voltage regulation and reactive power sharing. In this case, the solar irradiance level is set to be 500 W/m² for PV systems in both microgrids. The ESS in MG1 discharges real power at 500 kW while the ESS in MG2 is in standby mode (zero real power output). The proposed controller is activated at $t = 10$ s. Then, a 500 kVar reactive load step up is applied in MG1 at $t = 22$ s, and another reactive load step up happens in MG2 at $t = 37$ s.

As Figure 3.5(a) shows, without proper microgrid control for voltage support, the system has a low voltage operating point and experiences undervoltage issues especially when there is load step up, such as at MG2 PCC. The proposed voltage controller is able to enable microgrids to provide an extra 2% voltage regulation for the distribution system after being

activated. Besides, the PCC voltage dip caused by microgrid reactive load change is eliminated by the proposed control.

Figure 3.5(b) shows the convergence of reactive power sharing among the DERs for each microgrid. After the controller being activated, the reactive power sharing settles within 10 seconds at 73% and 68% of reactive power capacity in MG1 and MG2, respectively. Once the first load step in MG1 is applied, the DERs in MG1 boost up the reactive power output to full reactive power capacity and reach the new reactive power sharing point within 5 seconds. The DERs in MG2 have the same operation, taking up 95% of the available reactive power after the load step in MG2. It also takes around 5 seconds for the controller to converge in reactive power sharing. One can see from Figure 3.5(b) that the reactive power sharing among DERs in each microgrid is very accurate.

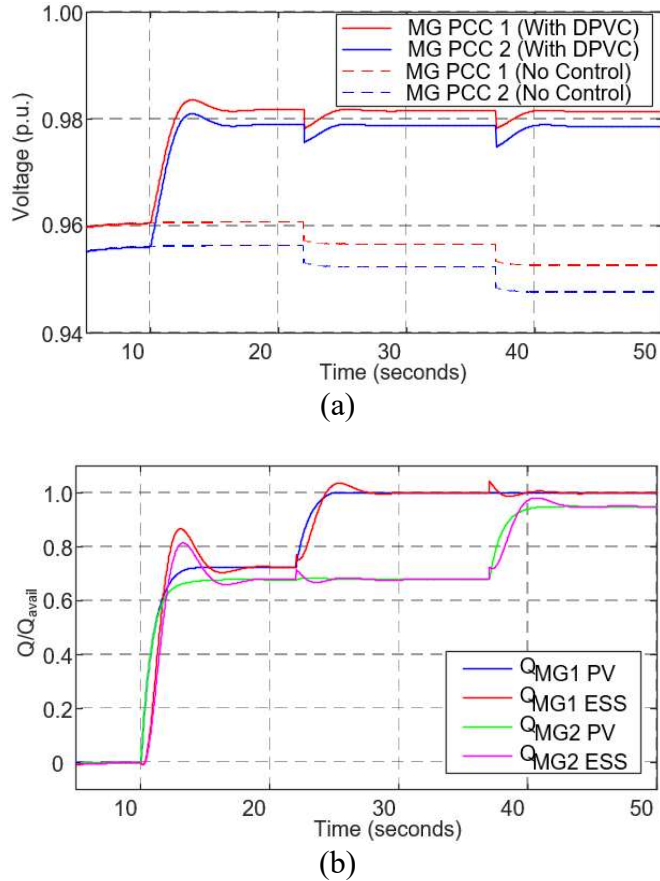


Figure 3.5. (a) Microgrid PCC voltage magnitude with and without control (b) Ratio of reactive power output to available reactive power capacity

3.4.2 Comparison with Unity Power Factor Control

Unity power factor (UPF) is suggested as the default mode for the installed DER in IEEE 1547-2018 [5] and it refers to zero reactive power flow at the point of interconnection for a grid-connected DER. It is considered as an intuitive control strategy for microgrid interconnection. Figure 3.6 compares the voltage profiles between the proposed controller and the UPF control for a cloud cover transient event. The event starts at $t = 22s$ and ends at $t = 37s$. The irradiance level changes from full sun condition to 100 W/m^2 and has an impact on PV systems in both microgrids. Even though UPF control leads to a similar voltage profile during the full sun condition to the proposed control, the proposed control is able to provide a tighter voltage profile during the cloud cover event. The reason behind the improvement of

voltage profile is that, since PCC voltage magnitude is one of the feedback to the proposed control, there is extra reactive power support provided when PCC voltage decreases. However, the UPF control fails to regulate PCC voltage by only guaranteeing zero reactive power flow at microgrid PCC.

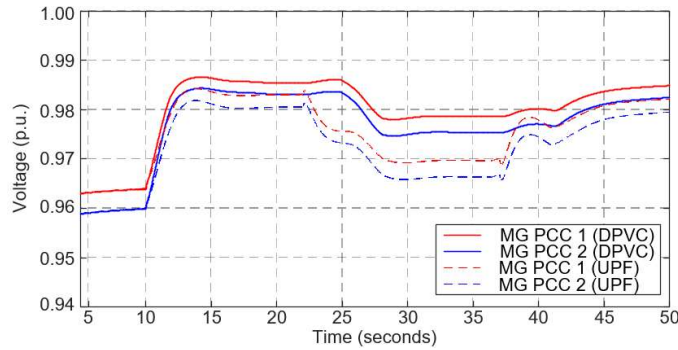


Figure 3.6. Comparison of voltage profiles for a cloud cover transient event

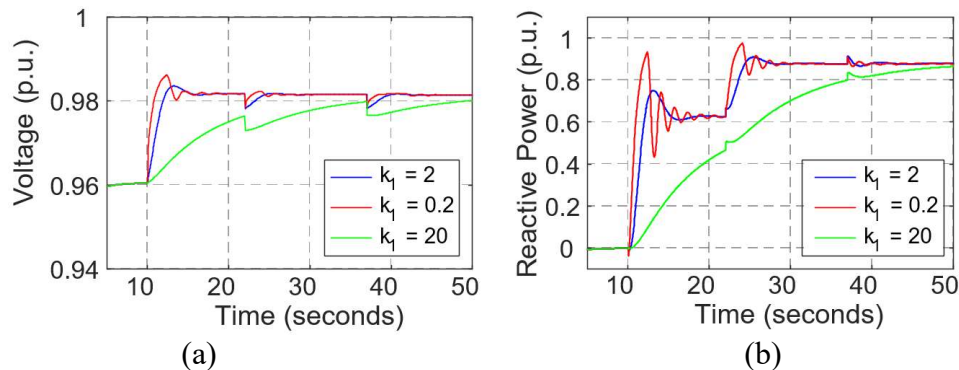


Figure 3.7. (a) MG1 PCC voltage magnitude (b) MG1 ESS reactive power output

3.4.2 The Impact of Control Gains on Dynamic Performance

This case study illustrates different dynamic responses of the DPVC under different parameter settings. As is already mentioned in Section III, decreasing DPVC control gains leads to smaller damping ratio and large overshoots. On the other hand, a sufficiently large DPVC control gain results in a slow overdamped response. Figure 3.7 compares the dynamic response of MG 1 PCC voltage and ESS reactive power output with a different selection of DPVC control gains k . The simulation setup is the same as in Section IV-A. It can be seen that, compared with $k = 20$, both voltage and reactive power responses with $k = 0.2$ exhibit

larger overshoot while the responses with a DPVC control gain of $k = 20$ can't even reach equilibrium point before the next load change due to slow response time. This case study demonstrates the consistency with the analysis in Section 3.3.

3.5 Conclusions

This chapter has proposed a new distributed proportional voltage control method for enabling the voltage support of grid-connected microgrids. The DPVC achieves voltage regulation at microgrid PCC by controlling the reactive power within the microgrid such that the microgrid PCC voltage maintains a proportional relationship with the reactive power flow at PCC, like Volt-Var control functions of smart inverters. The reactive power support to the grid is shared among multiple DERs within the microgrid in a distributed manner. The large-signal model of the closed-loop system is derived to analyze the impact of the control parameters on system stability and dynamic performance. Finally, the case studies validate the effectiveness of the DPVC and show that the DPVC is also friendly to multi-microgrid architecture in distribution systems.

CHAPTER 4. VOLT-VAR OPTIMIZATION OF DISTRIBUTION SYSTEMS FOR COORDINATING UTILITY VOLTAGE CONTROL WITH SMART INVERTERS

This chapter describes a new VVO strategy based on the concept of the VLSM for modeling the potential interaction between smart inverters, OLTCs and SCs. The proposed VVO model allows the coordination between utility voltage control devices and smart inverters in an optimal fashion. The algorithm is straightforward to implement, tolerant of communication loss or delay. The proposed VVO algorithm allows for adaptive Volt-Var curve slope settings that have certain advantages over fixed Volt-Var curve slope settings. The existing literature on VVO with DERs (or smart inverters) is discussed at first. Then, the VLSM model is introduced in Section 4.2. Section 4.3 describes the VVO formulation, as well as a successive linear programming technique for linearizing the model. Simulation results are given in Section 4.4 where the proposed VVO is validated on a 47-bus test distribution feeder using quasi-steady-state simulation. Section 4.5 concludes this chapter.

4.1 Literature Review

Compared to conventional voltage control on distribution systems relying on OLTCs and SCs, the Volt-Var control of smart inverters is an effective mechanism for mitigating the impact of DERs on voltage regulation of distribution systems. The smart inverters have a faster response to grid voltage changes and can continuously adjust their reactive power injection (or absorption). However, the coordination between smart inverters and utility voltage control devices at the primary distribution voltage level still needs to be further addressed.

As described in Section 1.1, the VVO problem for distribution systems is usually formulated as an optimal reactive power flow. There have been many papers proposing the VVO model that considers the reactive power capability of the DERs (smart inverter) where

the control variables for DERs are introduced into the formulation. However, the VVO problem itself is a mixed-integer nonlinear programming problem whose global optimal solution is not guaranteed due to the nonlinearity of the power flow equations. Although papers like [17] apply the heuristic algorithms to the VVO problem to determine the reactive power from DERs and microgrids as well as the settings of SCs and OLTCs, the solution can't be guaranteed to be globally optimal.

Several papers use sensitivity coefficients (or a linearized power flow in essence) to replace the original nonlinear power flow equations to make the VVO problem tractable. A two-stage centralized VVO model based on VLSM is proposed in [15], where the proposed VVO model not only considers the reactive power compensation from DERs and SCs as control variables, but also take into account the control for PV real power curtailment and load curtailment. But the OLTC control is not included. A centralized VVO model is proposed in [16]. By using the sensitivity coefficients of voltage deviations to control variables, the whole VVO problem becomes a mixed-integer linear programming (MILP) problem. The algorithm updates at each step the DER reactive power operation point and OLTC tap positions such that both voltage deviation and network losses are minimized. However, the coordination with SCs is not discussed. [68] derives a linearized three-phase optimal power flow to minimize the unbalance of three-phase distribution systems and to optimize voltage profiles by determining reactive power injection of smart inverters. However, the coordination with utility control devices is not discussed and the algorithm is only validated in a small-scale test system.

Other papers are presenting their VVO models based on convex relaxation of power flow equations. By relaxing the branch flow model [71], the intractable VVO model is transformed into a second-order conic programming model. The main advantage of this type of the VVO

model is that it can guarantee a globally optimal solution without a large demand for computation capability. [69] demonstrates the VVO model focusing on the inverter reactive power injection that achieves voltage regulation and system efficiency. A robust VVO model is described in [70] to handle the uncertainties in load and DERs. The coordination of DERs with SCs and SVRs is also considered. A distributed version of the VVO model is presented in [12] based on the alternating direction method of multipliers (ADMM) algorithm with good convergence performance.

The common feature of these VVO models summarized above is that these papers consider reactive power setpoints as the control variables of DERs. However, the real-time implementation of this type of VVO model leads to the vulnerability of handling fast disturbances such as cloud transients or load startup since the inverters are tracking reactive power setpoints, which won't be updated fast enough due to communication latency or computation speed. Therefore, the local voltage control based on Volt-Var control of the smart inverters is a promising solution. A local-feedback based Volt-Var control scheme has recently been approved as an IEEE 1547 standard [5] and is starting to be used by utilities in California [72] and Hawaii [73] as part of their PV integration strategy. A few existing works propose their VVO models based on Volt-Var control of smart inverters. Authors in [74] present the VVO model using model predictive control to coordinate DERs with OLTCs and SCs. Although the Volt-Var curve is mentioned and expressed using separable functions, how to handle the nonconvexity of the Volt-Var curve is not discussed. [75] proposes a VVO model where the Volt-Var curve is defined as piecewise linear functions such that the mixed-integer nonlinear problem is transformed into a mixed-integer linear problem. However, this piecewise linearization method using special ordered sets can bring in much more auxiliary decision

variables than the original problem. Therefore, the linearized model can be highly computational for large-scale problems.

The proposed VVO model in this study has several advantages compared to the models mentioned above: (1) the VVO model guarantees the global optimal solutions by using VLSPM, which is a linearized form of power flow; (2) the nonconvex term involving Volt-Var curve slope setting is relaxed using successive linearization techniques without introducing many auxiliary variables; (3) the VVO model considers the coordination of DERs with utility control devices such as SCs and OLTCs.

4.2 Voltage-Load Sensitivity Matrix

The VLSPM is originally defined as the sensitivity matrix that contains the sensitivity coefficients of bus voltages to real and reactive power injection (or absorption) in [15] and [76], where authors provide a simulation-based technique to compute VLSPM by running off-line power flow studies of three-phase distribution systems. In essence, the VLSPM is a linearized form of power flow model that can be theoretically derived from the branch flow model [71] and the detailed derivation can be found in [20] and [27]. In [20], authors also point out that the VLSPM is the inverse of the Bbus matrix, which provides an alternative for computing the VLSPM. In this section, we present an innovative form of VLSPM that integrates the Volt-Var control of smart inverters and OLTC control.

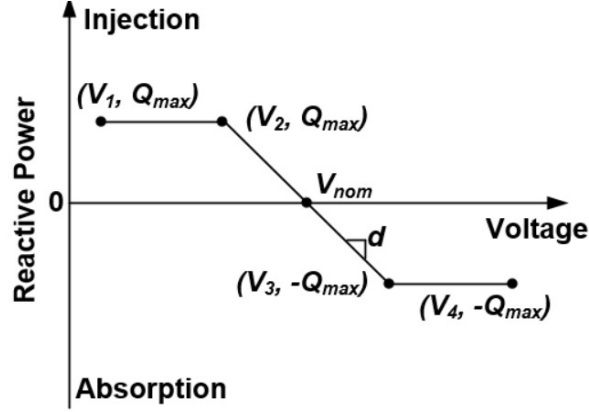


Figure 4.1. A typical Volt-Var curve of a smart inverter

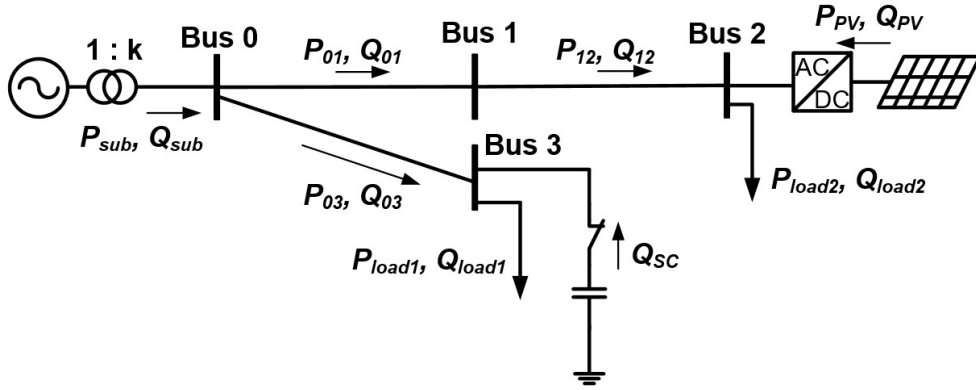


Figure 4.2. A simplified example of a 4-bus distribution system

The linear relationship between the input Q^g and the output V is established as

$$V = XQ^g + \bar{V} \quad (4.1)$$

where V contains all bus voltages; X is the VLSM of reactive power injection to bus voltages; Q^g contains the reactive power injection from PV inverters or SCs; \bar{V} is the voltage vector without additional Var support. Since (4.1) is a linearized form and X is constant, it can be rewritten in terms of the difference of reactive power injection ΔQ^g and bus voltage ΔV as

$$\Delta V = X\Delta Q^g \quad (4.2)$$

In the conventional VVO formulation, reactive power setpoints ΔQ^g tend to be considered as one of the control variables of DERs. However, compared to reactive power setpoints as direct controls, there are several advantages and practical considerations for using Volt-Var

curves as control settings: 1) if PV inverters work under local Volt-Var control, the reactive power setpoints will not be accessible by the utility; 2) given that PV inverters work under local Volt-Var control, they are able to automatically respond to voltage disturbances in the system; 3) if there is communication loss or latency between utility and PV inverters, the inverters can still work under the existing Volt-Var setting. A typical Volt-Var curve is shown in Figure 4.1 and can be mathematically expressed by

$$Q^g = -d(V - V_{nom}) \quad (4.3)$$

where Q^g is the injected reactive power from the PV inverter; d is a nonnegative value representing the Volt-Var slope setting; V_{nom} is the nominal voltage (e.g. 1.0 p.u.).

Figure 4.2 shows an example of a distribution system including one OLTC at substation bus, one PV plant with a smart inverter interface, one SC and two loads. The power solution shown in Figure 4.2 is before a control update. The voltage change at bus 0 after a control update is written as

$$\Delta V_0 = \frac{\partial V_0}{\partial k} \Delta k + \sum_{j=1}^3 \frac{\partial V_0}{\partial Q_j} \Delta Q_j \quad (4.4)$$

where Δk is the change of the OLTC tap; $\frac{\partial V_0}{\partial k}$ is the sensitivity factor of the OLTC tap change to voltage deviation at bus 0; $\frac{\partial V_0}{\partial Q_j}$ is the sensitivity factor of the reactive power injection change at bus j to voltage deviation at bus 0 and is the j th entry of the first row of \mathbf{X} . In this example, $\Delta Q_1 = 0$ because no load or generation is connected to bus 1. ΔQ_2 and ΔQ_3 are reactive power injection changes from the PV inverter at bus 2 and from the SC at bus 3, respectively. Combining (4.4) with (4.3) yields

$$\Delta V_0 = \frac{\partial V_0}{\partial k} \Delta k + \frac{\partial V_0}{\partial Q_2} (-d_2) \Delta V_2 + \frac{\partial V_0}{\partial Q_3} \Delta Q_3 \quad (4.5)$$

Since the rest of the bus voltages follow similar equations to (4.5), the vector form for the 4-bus example system is written as

$$\Delta \mathbf{V} = \frac{\partial \mathbf{V}}{\partial k} \Delta k + \frac{\partial \mathbf{V}}{\partial Q_2} (-d_2) \Delta V_2 + \frac{\partial \mathbf{V}}{\partial Q_3} \Delta Q_3 \quad (4.6)$$

To extend to a general form for an n-bus distribution system, (4.6) is rewritten as

$$\begin{aligned} \Delta \mathbf{V} &= \sum_{i \in OLTC} \frac{\partial \mathbf{V}}{\partial k_i} \Delta k_i + \sum_{j \in PV} \frac{\partial \mathbf{V}}{\partial Q_j} (-d_j) \Delta V_j + \sum_{k \in SC} \frac{\partial \mathbf{V}}{\partial Q_k} \Delta Q_k \\ &= \left[\frac{\partial \mathbf{V}}{\partial k} \right]_{OLTC} \Delta \mathbf{k} - \left[\frac{\partial \mathbf{V}}{\partial Q} \right]_{PV} \mathbf{d} \Delta \mathbf{V} + \left[\frac{\partial \mathbf{V}}{\partial Q} \right]_{SC} \Delta \mathbf{Q}_{SC} \end{aligned} \quad (4.7)$$

where *OLTC*, *PV* and *SC* are the sets of all the OLTCs, PVs and SCs in the system, respectively; $\left[\frac{\partial \mathbf{V}}{\partial k} \right]_{OLTC}$ is an $n \times l$ matrix where l is the number of OLTCs in the system; $\left[\frac{\partial \mathbf{V}}{\partial Q} \right]_{SC}$ is an $n \times m$ matrix where m is the number of SCs in the system; $\left[\frac{\partial \mathbf{V}}{\partial Q} \right]_{PV}$ is an $n \times n$ matrix whose i th column is a zero vector if there is no PV connected to the i th bus and \mathbf{d} is a diagonal matrix of the Volt-Var slope setting for PV inverters whose diagonal entries are nonzero only for buses in the *PV* set. Replacing $\Delta \mathbf{V}$ with $\mathbf{V} - \mathbf{V}^0$ yields

$$\left(\mathbf{I} + \left[\frac{\partial \mathbf{V}}{\partial Q} \right]_{PV} \mathbf{d}_t \right) \mathbf{V}_t = \left[\frac{\partial \mathbf{V}}{\partial k} \right]_{OLTC} \Delta \mathbf{k}_t + \left(\mathbf{I} + \left[\frac{\partial \mathbf{V}}{\partial Q} \right]_{PV} \mathbf{d}_t \right) \mathbf{V}^0 + \left[\frac{\partial \mathbf{V}}{\partial Q} \right]_{SC} \Delta \mathbf{Q}_{SC_t} \quad (4.8)$$

where \mathbf{I} is an $n \times n$ identity matrix; \mathbf{V} and \mathbf{V}^0 are the n-dimensional column vector of bus voltages after and before the control update, respectively.

As mentioned above, both sensitivity matrices $\left[\frac{\partial \mathbf{V}}{\partial Q} \right]_{PV}$ and $\left[\frac{\partial \mathbf{V}}{\partial Q} \right]_{SC}$ can be determined using the existing method. The procedure for computing $\left[\frac{\partial \mathbf{V}}{\partial k} \right]_{OLTC}$ via running off-line distribution power flow studies is shown as Algorithm 1 below.

Algorithm 1 $[\partial V/\partial k]_{OLTC}$ Sensitivity Matrix Calculation

- 1: Reset the taps for all the OLTCs such that $k_i = 1, \forall i \in OLTC$.
- 2: Conduct a time-series power flow study using a typical load profile.
- 3: Obtain the time series solution for all the bus voltages at each time step.
- 4: Choose the i th OLTC when $i = 1$.
- 5: Increment the tap position of the i th OLTC by 1 and $\Delta k_i = k_i - 1$.
- 6: Obtain new time series solutions for all the bus voltages at each time step.
- 7: Calculate the sensitivity factor of tap change to voltage at bus j :

$$\frac{\partial V_j}{\partial k_i} = \frac{\sum_{t=1}^T \Delta V_{j,t}}{\Delta k_i} / T$$

- 8: Repeat steps 5-7 until $k_i = k_{max}$.
 - 9: Repeat step 1.
 - 10: Repeat steps 5-7 but decrement the tap position instead of increment.
Stop until $k_i = k_{min}$.
 - 11: Average all the calculated $\frac{\partial V_j}{\partial k_i}$ and form the $\frac{\partial V}{\partial k_i}$.
 - 12: Repeat steps 5-11 for the rest of the OLTCs ($i = 2, 3, \dots, l$).
 - 13: Form the final $[\partial V/\partial k]_{OLTC} = \begin{bmatrix} \frac{\partial V}{\partial k_1} & \dots & \frac{\partial V}{\partial k_l} \end{bmatrix}$.
 - 14: End the $[\partial V/\partial k]_{OLTC}$ calculation.
-

4.3 Optimization Model

This section presents the proposed VVO model, which is assumed to be implemented in a centralized manner, for example, in a distribution control center. The sensitivity matrices are obtained by running power flow studies on a distribution circuit model. The VVO requires the matrices plus 24-hour load and renewable forecast to produce an optimal schedule for SCs ON/OFF status, OLTC tap controls, and the inverter Volt-Var curve slope settings. The detailed formulation and solution method of the optimization problem are summarized in the following subsection.

4.3.1. Problem Formulation

The VVO problem is formulated as a mixed-integer programming problem that consists of a multi-objective model with operational constraints for voltage control devices such as SCs, OLTCs and smart inverters, plus the constraints of VLSCM.

Objective functions: The objective is to minimize the sum of voltage deviation over each bus from nominal voltage while minimizing OLTC tap operations during the optimization horizon T, as

$$\min_{\boldsymbol{\mu}, \mathbf{d}, \mathbf{k}} \sum_{t \in T} \sum_{i=1}^n |V_{i,t} - V_{nom}| + \beta \sum_{j \in OLTC} n_{j,TO} \quad (4.9)$$

where $\boldsymbol{\mu}$ is the vector of the ON/OFF status for SCs; \mathbf{d} is the vector of Volt-Var slope settings for PV inverters; \mathbf{k} is the vector of the taps for OLTCs; $n_{j,TO}$ is the number of tap operations for the j th OLTC over the period T ; β is the weight factor for the second objective. The absolute value operation can be reformulated by introducing auxiliary variable $\Delta V_{i,t} = |V_{i,t} - V_{nom}|$ with the following constraints

$$\begin{cases} \Delta V_{i,t} \geq V_{i,t} - V_{nom} \\ \Delta V_{i,t} \geq -V_{i,t} + V_{nom} \end{cases} \quad (4.10)$$

SCs operating constraints: SC control variables are discrete, and the number of switching operations for each SC over the period T should be within the allowable limit, as

$$\begin{cases} \mu_{i,t} \in \{0, 1\} \\ \sum_{t \in T} |\mu_{i,t} - \mu_{i,t-1}| \leq a, \quad i \in SC \\ Q_{SCi,t} = \mu_{i,t} \times Q_{SCi}^{rated} \end{cases} \quad (4.11)$$

where a is the maximum number of switching operations for the period T , and Q_{SCi}^{rated} is the rated Var capacity of the i th SC. By adding a new integer variable $y_{i,t} = |\mu_{i,t} - \mu_{i,t-1}|$, (4.11) is rewritten in a linear form as

$$\left\{ \begin{array}{l} y_{i,t} \in \{-1, 0, 1\} \\ \mu_{i,t} \in \{0, 1\} \\ \sum_{t \in T} y_{i,t} \leq a \\ y_{i,t} \geq u_{i,t} - u_{i,t-1} \\ y_{i,t} \geq u_{i,t-1} - u_{i,t} \\ y_{i,t} \leq u_{i,t-1} + u_{i,t} \\ y_{i,t} \leq 2 - (u_{i,t-1} + u_{i,t}) \\ Q_{SCi,t} = \mu_{i,t} \times Q_{SCi}^{rated} \end{array} \right. , \quad \begin{array}{l} i \in SC \\ t \in T \end{array} \quad (4.12)$$

OLTC operating constraints: The tap of the OLTC is a discrete variable and can be represented using the tap position, which is an integer variable, as

$$\left\{ \begin{array}{l} k_i = 1 + p_i \times \delta k_i \\ p_{min} \leq p_i \leq p_{max} \\ p_i \in \mathbf{Z} \end{array} \right. , \quad i \in OLTC \quad (4.13)$$

where p_i is the tap position of the i th OLTC; p_{min} and p_{max} are the minimum and maximum tap position; δk_i is the smallest tap step of the i th OLTC. Besides, the number of OLTC tap operations can be established as

$$\left\{ \begin{array}{l} n_{i,TO} = \sum_{t \in T} \tau_{i,t} \\ \tau_{i,t} \in \{0, 1\} \\ \tau_{i,t} \geq \frac{p_{i,t-1} - p_{i,t}}{p_{max} - p_{min}} \\ \tau_{i,t} \geq \frac{p_{i,t} - p_{i,t-1}}{p_{max} - p_{min}} \end{array} \right. , \quad \begin{array}{l} i \in OLTC \\ t \in T \end{array} \quad (4.14)$$

where $\tau_{i,t}$ is the indicator of tap operation at time step t . If the tap position is changed at time step t , two inequalities will force $\tau_{i,t}$ equal to 1; if the tap position stays unchanged, $\tau_{i,t}$ will become a free variable and two inequalities will be identical. However, since the objective is to minimize the total number of tap operations, $\tau_{i,t}$ will still be zero in the optimal solution.

VLSM equality constraints: The conventional power flow constraints in distribution systems are replaced with (4.8). The voltage at each bus is estimated based on linear approximation over an operating point \mathbf{V}^0 .

The above model (4.8-4.14) is hard to solve because it's a mixed-integer nonconvex problem where (4.8) represents a set of quadratic equality constraints which are nonconvex. Thus, relaxation techniques are needed to transform the model into a convex one so that it can be solved efficiently using the existing solvers.

4.3.2. Successive Linear Programming

Successive linear programming is often used for solving nonlinear optimization problems via a sequence of linear programming problems [77]. The successive linear programming algorithm proves to be effective for large and sparse problems and is based on the idea that any nonlinear, differentiable function $g(x)$ can be expressed in its Taylor series linearization form as

$$\begin{cases} g(x) \approx g(\bar{x}) + J(\bar{x})\delta x \\ \delta x = x - \bar{x} \\ -s \leq \delta x \leq s \end{cases} \quad (4.15)$$

where \bar{x} is the base point, $J(x)$ is the Jacobian matrix of $g(x)$. However, the linearization form is only accurate for a “small” δx so upper and lower bounds are imposed for δx .

In order to transform the original problem into a convex one, auxiliary variables x are introduced to replace the quadratic term on the left-hand side of (4.8). Then (4.8) becomes

$$\begin{cases} V + \left[\frac{\partial V}{\partial Q} \right]_{PV} x = \frac{\partial V}{\partial k} \Delta k + \left(I + \left[\frac{\partial V}{\partial Q} \right]_{PV} d \right) V^0 + \left[\frac{\partial V}{\partial Q} \right]_{SC} \Delta Q_{SC} \\ x = dV \end{cases} \quad (4.16)$$

Since x contains mostly zero elements except for the entries corresponding to the PV inverters, a successive linear programming approach can be applied to linearize $x = dV$, which can be rewritten as

$$\begin{aligned}
x &\approx \bar{d} \bullet \bar{V} + J_x|_{(\bar{d}, \bar{V})} \begin{bmatrix} \delta d \bullet I \\ \delta V \end{bmatrix} \\
\delta d &= d - \bar{d} \\
\delta V &= V - \bar{V} \\
-s_1 &\leq \delta d \leq +s_1 \\
-s_2 &\leq \delta V \leq +s_2
\end{aligned} \tag{4.17}$$

where $\bar{dV} = [\bar{d}_1 \bullet \bar{V}_1, \bar{d}_2 \bullet \bar{V}_2, \dots, \bar{d}_n \bullet \bar{V}_n]^T$ is the vector of the product of the base points of the Volt-Var slope setting and the voltage at bus i ; J_x is the Jacobian matrix of x ; $\Delta = [d - \bar{d} \quad V - \bar{V}]^T$ represents the neighborhood of the base points (\bar{d}, \bar{V}) ; s_1 and s_2 are the bounds for limiting the range of the neighborhood. Therefore, the original VVO problem is transformed into a MILP (4.9-4.14) and (4.16-4.17). The successive linear programming algorithms for solving the problem is described below in Algorithm 2.

Algorithm 2 Successive linear programming algorithms for the VVO model

- 1: Choose the search bounds $(-s_1, s_1)$ and $(-s_2, s_2)$.
 - 2: Choose the initial base points (\bar{d}_0, \bar{V}_0) .
 - 3: Solve the MILP (4.9-4.14) and (4.16-4.17) and obtain the new solution (\bar{d}_1, \bar{V}_1)
 - 4: Check the convergence criteria:

$$\max[(\bar{d}_1 - \bar{d}_0), (\bar{V}_1 - \bar{V}_0)] < \varepsilon.$$
 - 5: If not, use (\bar{d}_1, \bar{V}_1) as new base point and repeat Step 3 and 4 until criteria is met
 - 6: End the successive linear programming algorithms.
-

4.4 Simulation Results

The 47-bus distribution feeder, based on a 12.35 kV industrial feeder, is used in this section to demonstrate the effectiveness of the proposed VVO. The circuit data are provided in detail in [19]. The circuit is integrated with five large PV plants as well as four SCs. A constant power factor of 0.85 is assumed for all the loads in the feeder. Several modifications to the circuit data [19] are summarized as follows: (1) the Var capacity for each capacitor is reduced to one-

tenth of that in the original circuit since the total SC capacity in the original design is 2 times the peak Var consumption assuming the 0.85 power factor; (2) two OLTCs with 32 taps and $\pm 5\%$ voltage regulation are added: one is between bus 4 and bus 5, and the other is at substation transformer (before bus 1); (3) the substation source is modeled as an ideal voltage source with source impedance. The modified circuit diagram is shown in Figure 4.3. Note that the 30 MVA lump load in the original circuit is kept in this study to represent the loads from the neighboring feeders.

Four test cases are considered in the simulation:

- Case 1: only substation OLTC is activated; all the SCs and the line SVR are disabled; no PV inverters are participating in voltage support.
- Case 2: all the SCs and the OLTCs enabled; no PV inverters are participating in voltage support.
- Case 3: all the SCs and the OLTCs enabled; PV inverters in Volt-Var mode with fixed slope settings.
- Case 4: all the SCs and the OLTCs enabled; PV inverters in Volt-Var mode with optimal slope settings.

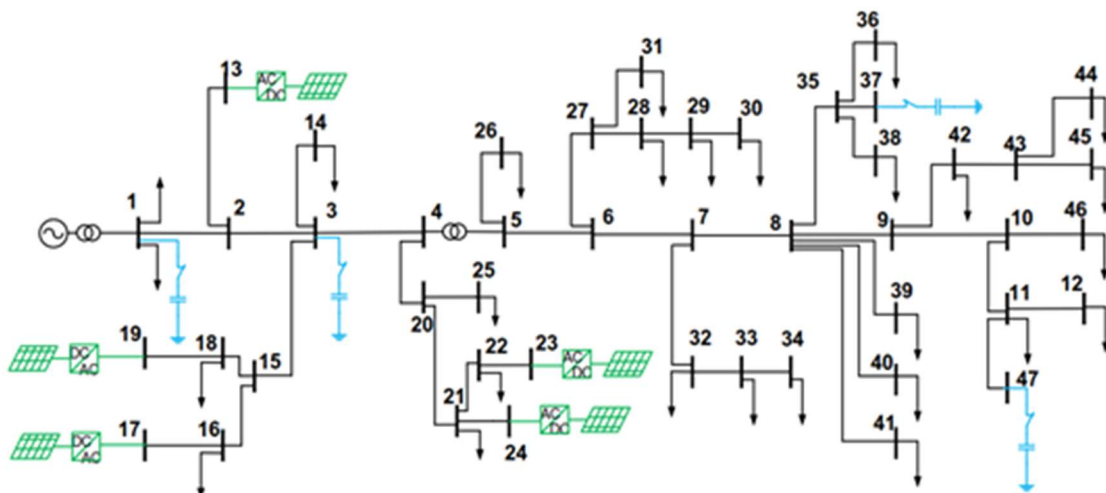


Figure 4.3. Circuit diagram of the 47-bus distribution feeder

The time series data is shown in Figure 4.4 for PV irradiance and load profiles for three consecutive days. Day 1 represents a heavy-load high-PV day, Day 2 represents a heavy-load low-PV day, and Day 3 represents a light-load high-PV day. The Volt-Var slope settings are assumed to be updated once a day.

Simulation of the proposed VVO algorithm for the test cases shows the improvements made possible by coordinating primary voltage control with the inverter settings. Figure 4.5 shows the three-day profile of the highest/lowest bus voltage in the feeder for each case. The feeder in Case 1 experiences undervoltage and overvoltage issues while the VVO model yields the flattest voltage profile among all the cases. There are also overvoltage issues observed in Case 2.

Table 4.1 summarizes the voltage ranges for all the cases. In Case 2, voltage profiles are slightly improved by enabling the line SVR and SCs compared to Case 1 where the only substation OLTC regulates feeder voltage. With the PV inverters participating in voltage support, the feeder voltage profile is tightened, especially for the heavy-load day. With optimal slope settings, the feeder voltage is further tightened to a flatter profile.

The Volt-Var slope settings are summarized in Table 4.2 for Case 3 and Case 4. The slope settings are expressed as per unit based on the base value chosen in [19]. For example, a Volt-Var slope setting of 35 Q p.u./V p.u. means that, reactive power injection/absorption will change by 0.35 p.u. per 0.01 p.u. voltage change. As shown in Table 4.2, the VVO model in Case 4 selects more aggressive slope settings than Case 3 and leads to better voltage regulation. On Day 3, the selected slope settings are extremely high. This is because, in the light load day, the PV inverters can regulate its bus voltage close to the nominal voltage using the available Var capacity. From the perspective of algorithm implementation, it indicates that for the light-

load condition, a PI-based voltage regulation can be used to replace a large Volt-Var slope setting.

The tap position of the OLTCs for all the cases is shown in Figure 4.6 and the number of tap operations is summarized in Table 4.3. Only in Case 1 does substation OLTC tap move while in other cases, substation OLTC is set to a fixed tap for the daily operation. A reduction in the number of line SVR operation is observed when PV inverters contribute to voltage regulation. However, with optimal Volt-Var slope settings (Case 4), the operation of the line SVR is significantly reduced by at least 40% compared to fixed Volt-Var slope settings (Case 3).

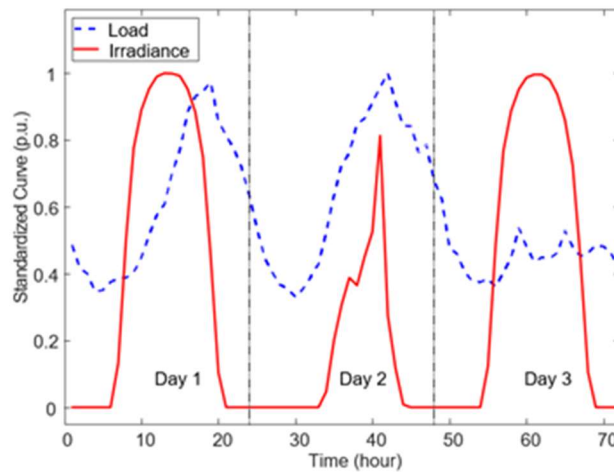


Figure 4.4. Three-day load profile and PV irradiance profile in p.u.

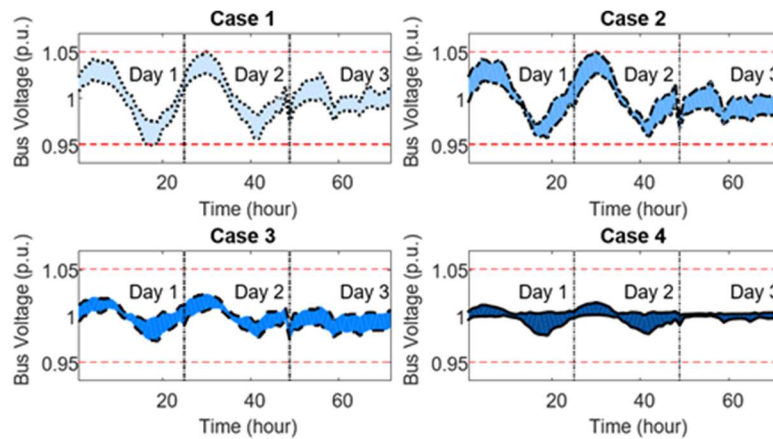


Figure 4.5. Three-day profile of min/max voltage in the system

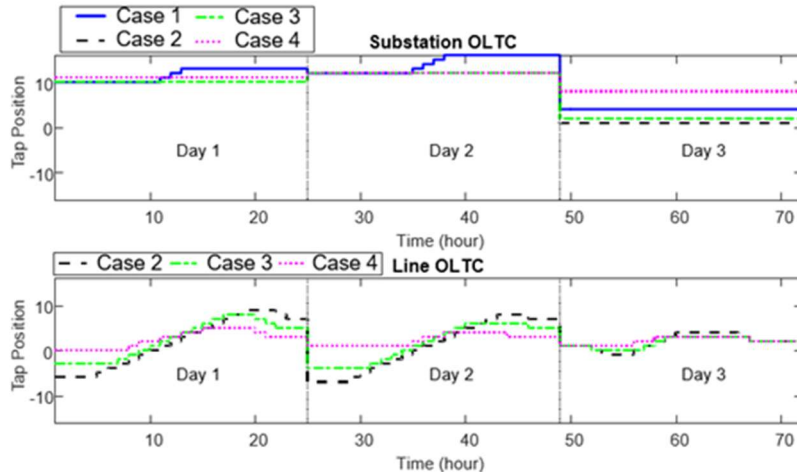


Figure 4.6. Three-day schedule of the OLTC tap position

Table 4.1. Summary of daily voltage ranges

Case #	Day 1	Day 2	Day 3
1	[0.948, 1.042]	[0.956, 1.050]	[0.972, 1.027]
2	[0.957, 1.042]	[0.958, 1.050]	[0.966, 1.018]
3	[0.972, 1.020]	[0.977, 1.024]	[0.973, 1.010]
4	[0.979, 1.012]	[0.980, 1.014]	[0.990, 1.004]

Table 4.2. Volt-Var curve slope settings (unit: Q p.u./V p.u.)

Case #	PV Bus	Day 1	Day 2	Day 3	Case #	PV Bus	Day 1	Day 2	Day 3
3	13	35	35	35	4	13	105	140	465
	17	9.2	9.2	9.2		17	29	37	739
	19	35	35	35		19	112	141	297
	23	23	23	23		23	51	56	187
	24	46	46	46		24	111	125	494

Table 4.3. Number of tap operations

Case #	Device	Day 1	Day 2	Day 3
1	Substation OLTC	3	4	0
	Line SVR	N/A	N/A	N/A
2	Substation OLTC	0	0	0
	Line SVR	17	16	9
3	Substation OLTC	0	0	0
	Line SVR	14	11	5
4	Substation	0	0	0
	Line	7	4	3

4.5 Conclusions

A new VVO model is proposed that determines optimal Volt-Var slope settings for smart PV inverters connected in a distribution system. This allows smart inverters to participate in voltage support in coordination with utility voltage control devices such as the SCs, the OLTCs and the SVRs. Sensitivity matrices are used to estimate bus voltages of the system and a successive linear programming approach is applied to relax the mixed-integer non-convex programming into a MILP problem, which can be efficiently solved. The results show that the proposed VVO is effective in tightening the feeder voltage profile and in reducing the number of tap operations. Future work includes the validation of this method on a large-scale multi-feeder distribution system and the evaluation of dynamic performance in highly-intermittent days.

CHAPTER 5. STOCHASTIC VOLT-VAR OPTIMIZATION FOR COORDINATING DISTRIBUTION-LEVEL CONTROL WITH SMART INVERTERS

This chapter proposes a novel stochastic VVO that optimizes the Q-V settings of smart inverters at PV plants considering the coordination with distribution-level control such as substation OLTCs, line SVRs and SCs. The study is a continued work on the VVO model proposed in Chapter 4 and considers the uncertainty of the irradiance forecast error. The remainder of the chapter is organized as follows. The stochastic model for solar irradiance forecasts is introduced in Section 5.2 as well as the techniques for scenario generation and reduction. Section 5.3 discusses the stochastic VVO model formulation. Section 5.4 compares the performance of stochastic solutions with deterministic solutions. Finally, conclusions are drawn in Section 5.5.

5.1 Literature Review

The distribution-level control, such as SVRs, OLTCs and SCs, plays a major role in conventional Volt-Var control practice in distribution systems. A quick growth of PV power plants in distribution systems leads to overvoltage issues and unexpected voltage fluctuations that are beyond the capabilities of conventional Volt-Var control. However, the smart inverters installed at these plants can provide new control options for mitigating the impacts of PV integration on distribution system voltage regulation. The local feedback based voltage control for smart inverters has been approved in the IEEE 1547-2018 standards [5] and been used by utilities in California and Hawaii as part of the PV integration strategies. However, the coordination between distribution-level control and smart inverters still needs to be further discussed.

Many researchers have investigated the VVO problem in distribution systems as a deterministic optimization problem. Authors in [12] and [69] have based their VVO models on second-order conic relaxation of the branch flow model [71]. A centralized mixed-integer linear programming (MILP) optimization model is proposed in [16] to minimize both voltage deviation and network losses using sensitivity coefficients of voltage deviations to control variables. The common feature of these VVO models is that these papers consider reactive power setpoints as the control variables of DERs. However, the real-time implementation of this type of VVO model leads to the vulnerability of handling fast disturbances. Therefore, some literature has proposed the VVO problem considering optimizing the local control settings of the smart inverters. An optimal voltage reference model is presented in [78] to decide voltage reference for the Q-V and P-V curves of the DERs to achieve loss minimization, but the coordination with distribution-level control is not yet considered. A centralized-based method is proposed in [79] to determine the Q-V and P-V curves in the coordination of SVRs, OLTCs and SCs. An optimization model is described in [80] to coordinate P-V curves for multiple DERs in the distribution network. Instead of optimizing the voltage profile, the model is intended for mitigating overvoltage while minimizing the curtailed power.

However, there are several sources of uncertainty that have impacts on distribution system operation, such as load demand and solar irradiance. Therefore, the VVO problem has been also modeled in a stochastic framework in the recent literature. The scenario-based approach and the chance-constrained programming are the two main stochastic frameworks being used in stochastic VVO. In [81], a scenario-based multi-objective VVO model is proposed to include the uncertainty related to load demand, wind speed and solar irradiance. A similar scenario-based approach is applied in [82] to the control of smart inverters for PV plants in

order to decide the optimal reactive power setpoints. A chance-constrained optimization model is defined in [83] to avoid SVR runaway in the presence of forecast errors in PV generation. The two-stage chanced-constrained VVO is presented in [84] to achieve robust voltage regulation in the face of uncertainty from DG output and consumer loads. The distribution-level control devices are dispatched optimally in the first stage while the reactive power dispatch rule is optimized in the second stage.

The main innovation of the study in this chapter is that all the local control settings for distribution-level control and smart inverters are decided in a coordinated and optimal way under a stochastic framework. A scenario-based approach is used to model the uncertainty of solar irradiance. An effective scenario reduction method is applied to approximate the uncertainty using a small number of scenarios, in order to make the original stochastic programming tractable. Then the stochastic problem is converted to an equivalent deterministic problem that can be efficiently solved using commercial solvers.

5.2 Forecast Error Characterization

5.2.1. Stochastic Modeling for Forecast Errors

The forecast errors for solar irradiance result from the uncertainty of weather conditions, respectively. To develop a stochastic VVO model that takes irradiance uncertainty into account, the variations are modeled by random variables that follow certain probability density functions.

Beta distribution [81] and normal distribution [83] are the two most common probability distribution to characterize the uncertainty of solar irradiance. The normal distribution is selected in this study for fitting the forecast error data in [85] as shown in Figure 5.1. A probability density function of a normal distribution is described as follows:

$$f(x) = \frac{1}{\sigma\sqrt{2\pi}} e^{-(x-\mu)^2/2\sigma^2} \quad (5.1)$$

where x is the irradiance forecast error. To discretize the continuous probability density function, five intervals are chosen to represent different levels of forecast errors. The probability mass function of the irradiance forecast error is written as follows:

$$\rho_x(x_l) = P(x = x_l), l = 1, 2, 3, 4, 5 \quad (5.2)$$

One scenario includes a series of forecast error realizations. For example, for a one-hour resolution daily profile, the scenario is made up of 24 realizations. Each scenario s is shown as follows:

$$s = \{x_{l,t,i} \mid t \in T, i \in PV \} \quad (5.3)$$

where T is the period of interest and PV is the set of PV inverters. The Monte-Carlo simulation is conducted to generate daily scenarios for modeling irradiance uncertainty based on (5.2) and (5.3). A new weight factor P_s is assigned to each scenario s to represent the occurrence in the total sample N . In this case, the total number of samples is selected to be 3000.

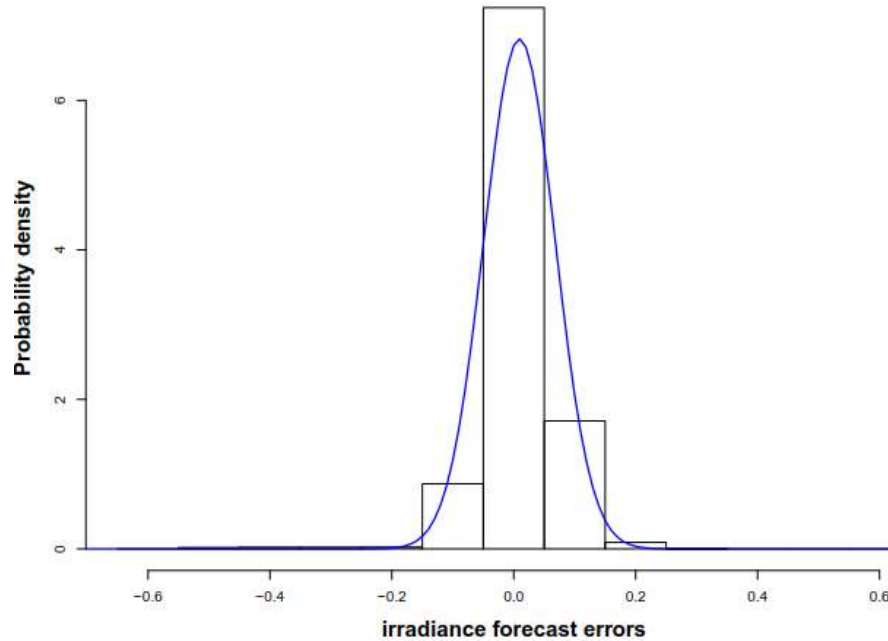


Figure 5.1. Solar irradiance forecast error

5.2.2. Scenario Reduction

It is intractable to solve the stochastic optimization problem considering all the sampled scenarios if the number of samples is significant. A scenario reduction technique is implemented to reduce a large scenario set to a small one while maintaining a good approximation of the uncertainty from the original set. Figure 5.2 shows the scenario set sampled from the Monte-Carlo simulation as well as the reduced scenario set that is integrated into the stochastic VVO model.

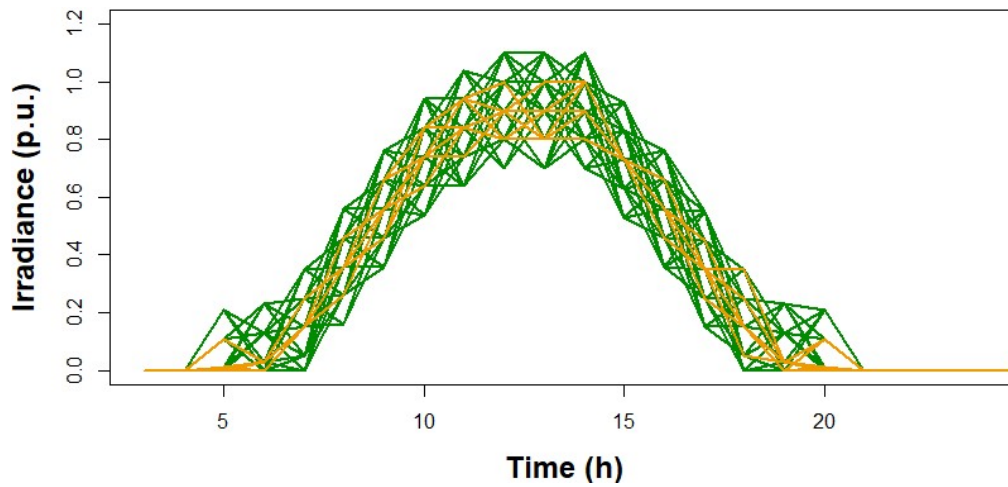


Figure 5.2. Sampled scenario set (green) and reduced scenario set (orange)

To evaluate whether two scenario sets are sufficiently close, the most common probability distance *Kantorovich distance* is used:

$$D(Q, Q') = \sum_{s \in \Omega} P_s \min_{s' \in \Omega_S} c(s, s') \quad (5.4)$$

where Ω is the original scenario set and Q is the probability distribution corresponding to Ω ; Ω_S is the reduced set and Q' is the probability distribution corresponding to Ω_S .

The well-established scenario reduction methods include, but are not limited to, backward reduction [81], forward reduction [86] and fast forward reduction [87]. The fast forward reduction algorithm is selected in this study, and the procedures are described as follows:

Step 1: Set $\Omega^{[0]} = \Omega$ as the initial scenario set. Set $\Omega_S^{[0]} = \emptyset$ as the reduced set that will eventually contain all the selected scenarios. Compute the distance of each pair of scenarios using

$$c(s, s') = \|s - s'\|^r \quad (5.5)$$

Step 2: Obtain the starting scenario s_1 using

$$s_1 = \arg \min_{s' \in \Omega} \sum_{s \in \Omega} P_s c(s, s') \quad (5.6)$$

Then $\Omega^{[1]} = \Omega^{[0]} \setminus \{s_1\}$ and $\Omega_S^{[1]} = \Omega_S^{[0]} \cup \{s_1\}$. The starting scenario s_1 is interpreted as the most representative scenario in Ω , and $\Omega_S^{[1]}$ has the shortest *Kantorovich distance* with the original scenario set Ω .

Step 3: Based on the starting scenario s_1 , a new scenario is added at every step to the reduced scenario set until the number of the selected scenarios reaches the target. The i th selection rule is applied as follows:

$$s_i = \arg \min_{s' \in \Omega^{[i-1]}} \sum_{s \in \Omega^{[i-1]}} P_s \min_{s'' \in \Omega_S^{[i-1]} \cup \{s'\}} c(s, s'') \quad (5.7)$$

where $\Omega^{[i]}$ is the remaining scenario set after i steps of scenario selection, and $\Omega_S^{[i]}$ is the reduced scenario set that contains the scenarios selected after the i steps of selection. Similar to Step 2, it is valid that $\Omega^{[i]} = \Omega^{[i-1]} \setminus \{s_i\}$ and $\Omega_S^{[i]} = \Omega_S^{[i-1]} \cup \{s_i\}$.

Step 4: After reaching the target within N steps, it is obvious that $\Omega^{[N]} = \Omega \setminus \Omega_S$. The new probability for each scenario s in Ω_S is defined by adding the probabilities of the scenarios in $\Omega^{[N]}$ to the ones in Ω_S . The re-assignment of the probabilities in Ω_S is described as follows:

$$P_s^* = P_s + \sum_{s' \in A(s)} P_{s'} \quad (5.8)$$

where

$$A(s) = \{s' \in \Omega^{[N]} \mid c(s, s') = \min_{s'' \in \Omega_s} c(s', s'')\} \quad (5.9)$$

The idea is to assign the probability of the unselected scenario in $\Omega^{[N]}$ to the closest one in $\Omega^{[N]}$ based on (5.5).

5.3 Stochastic Volt-Var Optimization Model

The formulation of the deterministic VVO model is obtained from [88], based on which the stochastic VVO model is built. The main difference between the deterministic VVO and the stochastic VVO is that the latter one makes decisions on voltage control settings considering the uncertainty of irradiance forecast. The objective of the stochastic VVO problem is described as follows:

$$\min \sum_{s=1}^{n_S} P_s \left(\beta \sum_{j=1}^{n_{SVR}} n_{TOs,j} + \sum_{t=1}^T \sum_{i=1}^n |V_{s,t,i} - V_{nom}| \right) \quad (5.10)$$

The objective function (5.10) is composed of the number of tap operations, plus the voltage deviation across the system. The decision variables of the stochastic VVO include tap positions, capacitor switching ON/OFF status and smart inverter Volt-Var curve settings. All the variables are the so-called *first-stage decision variables*, taken before the scenario is known [89]. In this formulation, no *second-stage decision variable* is considered, that is, no decision is made after the scenario is realized.

The constraints for different scenarios are presented as follows. The constraints of capacitor switching operation include:

$$y_{s,t,i} \in \{0,1\} \quad (5.11a)$$

$$\mu_{s,t,i} \in \{0,1\} \quad (5.11b)$$

$$y_{s,t,i} \geq \mu_{s,t,i} - \mu_{s,t-1,i} \quad (5.11c)$$

$$y_{s,t,i} \geq \mu_{s,t-1,i} - \mu_{s,t,i} \quad (5.11d)$$

$$y_{s,t,i} \leq \mu_{s,t,i} + \mu_{s,t-1,i} \quad (5.11e)$$

$$y_{s,t,i} \leq 2 - (\mu_{s,t-1,i} + \mu_{s,t,i}) \quad (5.11f)$$

$$Q_{SCs,t,i} = \mu_{s,t,i} Q_{SCs,t}^{rated} \quad (5.11g)$$

$$n_{COs,i} = \sum_{t=2}^T y_{s,t,i} \quad (5.11h)$$

(5.11a) and (5.11b) define the binary variables for capacitor operation indicator and capacitor ON/OFF status. (5.11c-f) indicate the relationship between capacitor operation indicator and capacitor ON/OFF status. (5.11g) defines the reactive power output from SCs while (5.11h) defines the total number of capacitor operations within a day.

The tap operation constraints include:

$$p_{s,t,j} \in \mathbf{Z} \quad (5.12a)$$

$$p_{min,j} \leq p_{s,t,j} \leq p_{max,j} \quad (5.12b)$$

$$\tau_{s,t,j} \in \{0,1\} \quad (5.12c)$$

$$\tau_{s,t,j} \geq \frac{p_{s,t-1,j} - p_{s,t,j}}{p_{max,j} - p_{min,j}} \quad (5.12d)$$

$$\tau_{s,t,j} \geq \frac{p_{max,j} - p_{min,j}}{p_{s,t,j} - p_{s,t-1,j}} \quad (5.12e)$$

$$k_{s,t,j} = 1 + p_{s,t,j} \delta k_j \quad (5.12f)$$

$$n_{TOs,j} = \sum_{t=2}^T \tau_{s,t,j} \quad (5.12g)$$

(5.12a) and (5.12b) define integer variables and operation bounds for tap positions. (5.12c) defines the binary variables for the tap operation indicator. (5.12d) and (5.12e) indicate the

relationship between tap operation indicator and tap position. (5.12f) defines the voltage ratio while (5.12g) defines the total number of tap operations within a day.

The smart inverter operation constraints include:

$$Q_{PVs,t} = -d_{s,t,i}(V_{s,t,i} - V_{nom}) \quad (5.13a)$$

$$Q_{PVmin,s,t,i} \leq Q_{PVs,t,i} \leq Q_{PVmax,s,t,i}, \quad (5.13b)$$

(5.13a) and (5.13b) describes a linear curve for Volt-Var control. Note that the maximum and minimum reactive power limits are not fixed constant but dependent on the real power output of the PV inverters. The system operation constraints, including voltage security limit and substation power factor limit, are described as follows:

$$V_{min} \leq V_{s,t,i} \leq V_{max} \quad (5.14a)$$

$$\frac{-\sqrt{1-PF_{min}^2}}{PF_{min}} P_{sub,s,t} \leq Q_{sub,s} \leq \frac{\sqrt{1-PF_{min}^2}}{PF_{min}} P_{sub,s,t} \quad (5.14b)$$

The conventional power flow constraints in distribution systems are replaced with equality constraints containing voltage sensitivity matrix [88]. The stochastic version is described as follows:

$$\begin{aligned} V_{s,t,i} = & V_{t,i}^0 + \sum_{j \in PV} \frac{\partial V_i}{\partial Q_j} \left(-d_{s,t,j}(V_{s,t,j} - V_{nom}) \right) + \sum_{j \in PV} \frac{\partial V_i}{\partial P_j} \Delta P_{PVs,t} \\ & + \sum_{j \in SVR} \frac{\partial V_i}{\partial k_j} \Delta k_{s,t,j} + \sum_{j \in SC} \frac{\partial V_i}{\partial Q_j} \Delta Q_{SCs,t,j} \end{aligned} \quad (5.15)$$

where $\Delta P_{PVs,t}$ represents the output power deviation at time t from PV unit j caused by irradiance forecast errors in scenario s .

There are also constraints representing the coupling among scenarios. For all the first-stage decision variables, non-anticipativity constraints should be enforced. In other words, the first-

stage decisions made for any of the two distinct scenarios s and s' must be the same up to time T :

$$\mu_{s,t,i} = \mu_{s',t,i} \quad (5.16a)$$

$$k_{s,t,i} = k_{s',t,i} \quad (5.16b)$$

$$d_{s,t,i} = d_{s',t,i} \quad (5.16c)$$

These equality constraints guarantee that the decisions are made before any uncertainty is realized. Without these constraints, the problem will decompose into independent problems for each scenario s .

Accordingly, the objective function (5.10) combined with constraints (5.11-5.16) forms a stochastic VVO problem, which is a stochastic mixed-integer nonconvex programming. Given a finite number of scenarios, the above stochastic VVO model can be easily written as the extensive form that is solved using deterministic mix-integer programming [90].

5.4 Case Studies

To validate the proposed stochastic VVO model, the modified 47-bus distribution feeder is considered in this section. The circuit diagram is shown in Figure 5.3 and the detailed circuit data is provided in [88]. The discrete distribution for solar irradiance forecast error is shown in Table 5.1. The normalized substation real and reactive power consumption profiles are seen in Figure 5.4. A total of 20 scenarios are selected as the final reduced scenario set. Four cases are included with different parameter settings for tap operation. Case 1 considers $\beta = 0$, indicating that no constraints are imposed for daily tap operation; Case 2 and Case 3 consider weight factors $\beta = 0.01$ and $\beta = 0.1$, respectively; Case 4 considers $\beta = 0$, as well as imposing maximum allowable number of operations on tap operation. In each case, the solutions from the deterministic and the stochastic approach are compared.

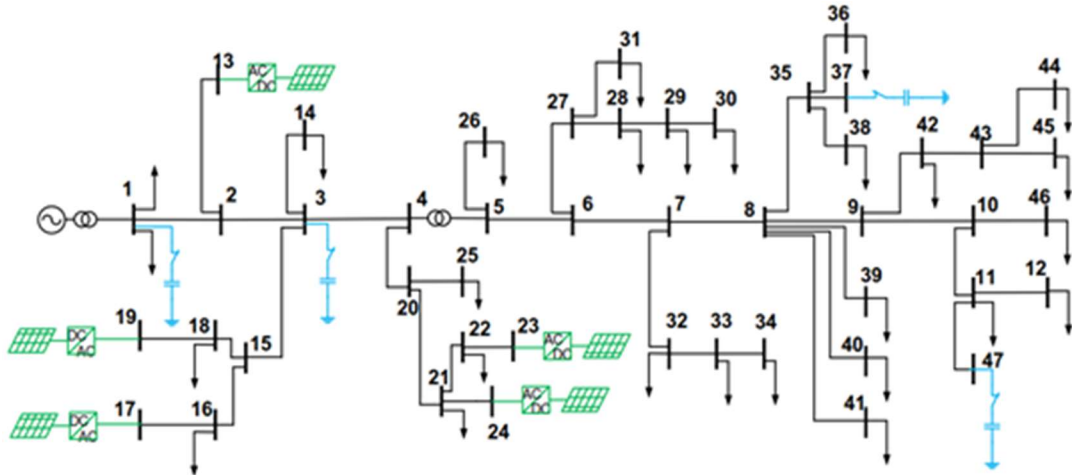


Figure 5.3. Circuit diagram of the 47-bus distribution feeder

Table 5.1. Discrete distribution for solar irradiance forecast error

x_l	-0.2	-0.1	0	0.1	0.2
$P(x = x_l)$	0.003	0.152	0.602	0.235	0.008

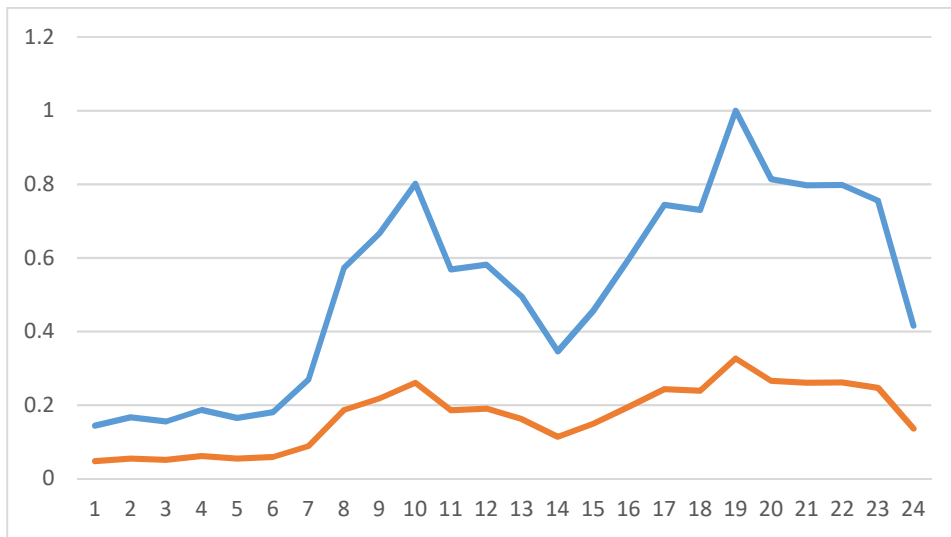


Figure 5.4. Normalized substation load profile: real power (blue) and reactive power (orange)

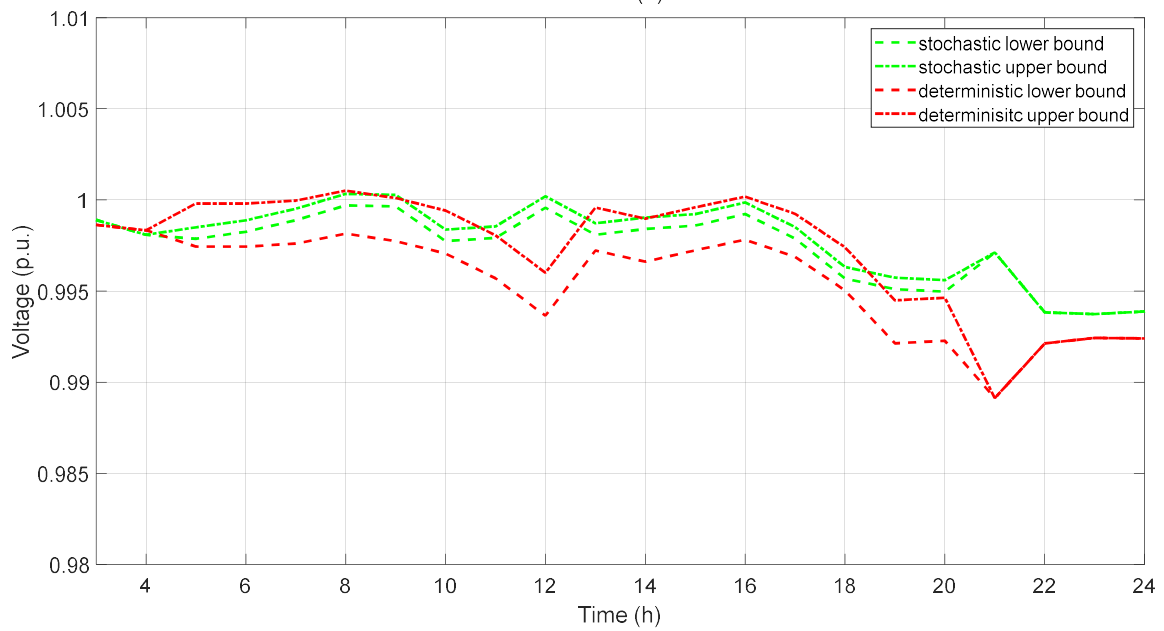
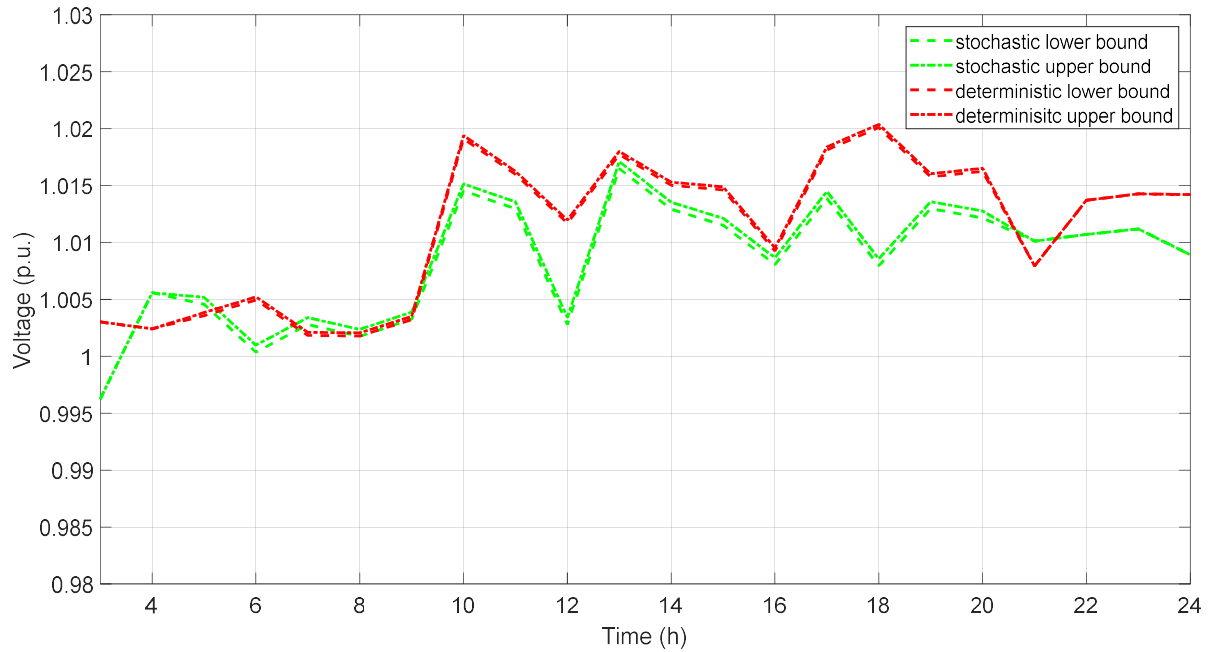


Figure 5.5. Voltage profile at bus 1 and bus 23 in Case 1

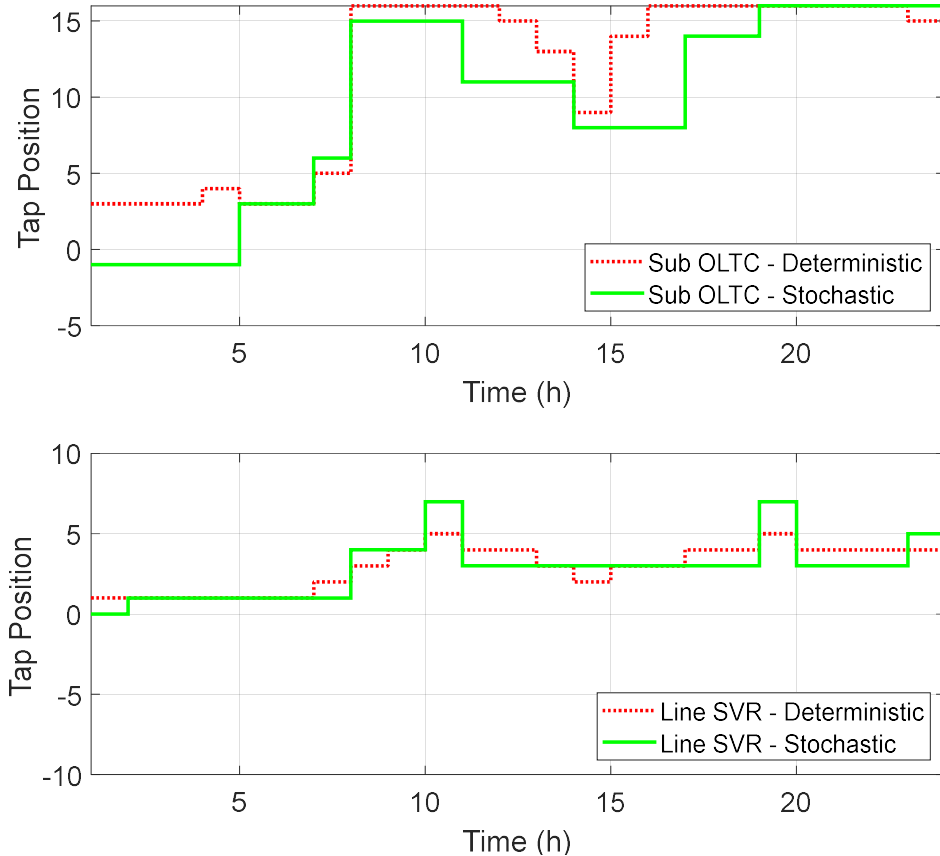


Figure 5.6. Tap operation schedule in Case 1

The 24-hour voltage profile for bus 1 and bus 23 in Case 1 is shown in Figure 5.5. As the highest voltage bus in the circuit, the stochastic approach shows better performance than the deterministic approach in terms of regulating voltage close to nominal voltage. The tight bounds of the voltage profile at bus 1 are caused by the small voltage sensitivity coefficients in terms of bus 1. A similar observation can be made for voltage profile at bus 23 where stochastic solutions provide better voltage regulation.

The tap operation schedules from two approaches in Case 1 are shown in Figure 5.6. As can be seen, the tap operation pattern is aligned with the substation load profile. The capacitor switching number is summarized in Table 5.2, where we can observe a significant number of switching operations of Capacitor 1 and 3 from the stochastic solution. One possible cause is

that the location of Capacitor 1 and 3 is closer to the PV farms and sensitive to the impact of the irradiance forecast errors.

Table 5.2. Capacitor switching number for all cases

Cap #	Model Type	Case 1	Case 2	Case 3	Case 4
Cap 1	Deterministic	8	10	12	10
	Stochastic	18	12	6	18
Cap 3	Deterministic	2	2	6	2
	Stochastic	10	10	8	10
Cap 37	Deterministic	10	8	8	10
	Stochastic	8	10	4	8
Case 47	Deterministic	6	6	8	10
	Stochastic	6	8	6	6

The performance of the deterministic solution and the stochastic solution is compared in Table 5.3. Overall the stochastic VVO leads to a smaller objective cost than the deterministic one in all cases. The first objective cost is related to the number of tap operations. There is no obvious pattern observed on whether the stochastic model leads to a reduced tap operation. However, as the weight factor β increases, the tap operation is reduced. The second objective cost is related to voltage deviation where the stochastic approach always results in better performance.

Table 5.3. Objective cost comparison

Case #	Model Type	Tap operation #	Cap operation #	Voltage deviation	Obj cost
Case 1	Deterministic	11.5 avg.	6.5 avg.	1.343	1.343
	Stochastic	▼8 avg.	▲10.5 avg.	▼0.976	▼0.976
Case 2	Deterministic	6.5 avg.	6.5 avg.	1.219	1.349
	Stochastic	▲11 avg.	▲10 avg.	▼1.077	▼1.297
Case 3	Deterministic	2.5 avg.	8.5 avg.	1.419	1.919
	Stochastic	2.5 avg.	▼6.5 avg.	▼1.102	▼1.602
Case 4	Deterministic	8 avg.	8 avg.	1.205	1.205
	Stochastic	8 avg.	▲10.5 avg.	▼1.126	▼1.126

5.5 Conclusion

In this chapter, a stochastic VVO formulation is proposed to determine optimal control settings for SVRs, OLTCs, SCs and smart inverters considering the uncertainty of solar irradiance forecast. The forecast error is characterized by a normal distribution and then discretized to a probability mass function. Monte-Carlo simulation is applied to generate 24-hour scenarios for the irradiance forecast, and an effective scenario reduction method is used to reduce a huge number of scenarios to the most representative scenario set. The stochastic VVO is developed and solved by converting the stochastic problem into an equivalent deterministic problem. The numerical simulation shows that the proposed stochastic model featuring solar irradiance uncertainty provides more reliable decisions on regulating voltage as well as meeting other operating constraints.

CHAPTER 6. SUMMARY AND FUTURE WORK

6.1 Summary of Current Work

This work focuses on the development of a new hierarchical voltage control framework for coordinating utility control devices, such as SCs, OLTCs and SVRs with the fast-responding DERs and microgrids. The main contributions of the work that is presented in Chapter 2 to 5 are as follows:

- Each control layer is modeled in detailed and the interaction between the control layers are clearly defined;
- The hybrid model parameterization algorithm presented in Chapter 2 is useful to generate a complete list of parameters and validate primary level control given limited field measurements.
- The secondary level control presented in Chapter 3 is able to coordinate multiple DERs in the microgrid footprint and proves to be effective in voltage support for distribution systems. The proposed secondary level control supports the multi-microgrid configuration and the small-signal analysis is also given to show the impact of controller parameters on closed-loop system characteristics.
- The proposed tertiary voltage control presented in Chapter 4 is developed to determine the optimal operating settings for smart inverters with considering an optimal schedule of SCs, OLTCs and SVRs. The simulation results show that under the tertiary control layer, the number of operations of utility control devices can be reduced and the system voltage can be tightly regulated.
- The stochastic framework for tertiary voltage control presented in Chapter 5 is developed to integrate the solar forecast errors into the VVO model. The simulation results show that

the stochastic solution provides more reliable solutions given the uncertainty of solar irradiance.

6.2 Future Work Proposal

There are a few directions that can lead to more in-depth and complete research based on the current work:

Integration of secondary control layer with tertiary control layer:

Currently, the tertiary control layer didn't consider the optimization of Volt-Var curve slope settings for microgrid operation. The key issue is how the dynamic reactive power limitation can be considered since the available reactive power capacity is dominantly decided by the real power operation point of the DERs. Under this framework, the tertiary layer control may require the reactive power limitation of microgrids to be updated by the secondary level controller such that the corresponding constraints are included in the VVO model. How much information should be transferred without incurring the privacy issue should be also considered in this study.

Real-time implementation of the control framework:

Currently, the VVO model is assumed to be executed day-ahead. However, there should be also a real-time version of the VVO model running with the updated system measurement and control status since system states in real-time will deviate from the presumed system states. The real-time VVO model is expected to be executed on a smaller time scale and adjust some control parameters in order to adapt to system operation in a nearer future. Finally, an integrated real-time HIL simulation can be the testing environment to validate this type of hierarchical control framework.

REFERENCES

- [1] National Electrical Manufacturers Association, *American National Standards for Electric Power Systems and Equipment-Voltage Ratings (60 Hertz)*. ANSI C84.1-2016, June 2016.
- [2] K. Clement-Nyns, E. Haesen and J. Driesen, "The Impact of Charging Plug-In Hybrid Electric Vehicles on a Residential Distribution Grid," *IEEE Transactions on Power Systems*, vol. 25, no. 1, pp. 371-380, Feb. 2010.
- [3] T. Aziz and N. Ketjoy, "PV Penetration Limits in Low Voltage Networks and Voltage Variations," *IEEE Access*, vol. 5, pp. 16784-16792, 2017.
- [4] C. Whitaker, J. Newmiller, M. Ropp, and B. Norris, "Renewable Systems Interconnection Study: Distributed Photovoltaic Systems Design and Technology Requirements," Sandia National Laboratories, Albuquerque, NM, Tech. Rep. SAND2008-0946-P, Feb. 2008.
- [5] *IEEE Standard for Interconnection and Interoperability of Distributed Energy Resources with Associated Electric Power Systems Interfaces*. IEEE Std 1547-2018 (Revision of IEEE Std 1547-2003), April 2018.
- [6] M. Daliparthi, M. Jakub-Wood, A. Bose and A. Srivastava, "Analysis of the Volt/VAR Control Scheme for Smart Distribution Feeders," in *2012 North American Power Symposium (NAPS)*, Champaign, IL, 2012.
- [7] Turan Gonen. *Electric Power Distribution Engineering, Third Edition*. Boca Raton: Chapman and Hall/CRC Press, 2014.

- [8] X. Wang, G. Liu, Y. Zeng, Z. Yang and S. Fan, "An Integrated Volt-Var Control Method in Distribution Network based on Distributed Generation," in *2nd IET Renewable Power Generation Conference (RPG 2013)*, Beijing, 2013.
- [9] A. Vukojevic, P. Frey, M. Smith and J. Picarelli, "Integrated Volt/Var Control Using Single-phase Capacitor Bank Switching," in *2013 IEEE PES Innovative Smart Grid Technologies Conference (ISGT)*, Washington DC, 2013.
- [10] H. Ahmadi, J. R. Martí and H. W. Dommel, "A Framework for Volt-VAR Optimization in Distribution Systems," *IEEE Transactions on Smart Grid*, vol. 6, no. 3, pp. 1473-1483, May 2015.
- [11] B. A. de Souza and A. M. F. de Almeida, "Multiobjective Optimization and Fuzzy Logic Applied to Planning of the Volt/Var Problem in Distributions Systems," *IEEE Transactions on Power Systems*, vol. 25, no. 3, pp. 1274-1281, Aug. 2010.
- [12] W. Zheng, W. Wu, B. Zhang, H. Sun and Y. Liu, "A Fully Distributed Reactive Power Optimization and Control Method for Active Distribution Networks," *IEEE Transactions on Smart Grid*, vol. 7, no. 2, pp. 1021-1033, March 2016.
- [13] Y. Shi, *Integrated Volt/Var Control on Smart Distribution Systems*. PhD [Dissertation]. Raleigh, NC: North Carolina State University, 2018.
- [14] Y. J. Kim, J. L. Kirtley and L. K. Norford, "Reactive Power Ancillary Service of Synchronous DGs in Coordination with Voltage Control Devices," *IEEE Transactions on Smart Grid*, vol. 8, no. 2, pp. 515-527, March 2017.
- [15] X. Zhu, J. Wang, N. Lu, N. Samaan, R. Huang and X. Ke, "A Hierarchical VLSM-Based Demand Response Strategy for Coordinative Voltage Control between Transmission and Distribution Systems," *IEEE Transactions on Smart Grid*, in press.

- [16] A. Borghetti, et al., "Short-Term Scheduling and Control of Active Distribution Systems with High Penetration of Renewable Resources," *IEEE Systems Journal*, vol. 4, no. 3, pp. 313-322, Sept. 2010.
- [17] A. G. Madureira and J. A. Pecas Lopes, "Coordinated Voltage Support in Distribution Networks with Distributed Generation and Microgrids," *IET Renewable Power Generation*, vol. 3, no. 4, pp. 439-454, Dec. 2009.
- [18] T. A. Short. *Electric Power Distribution Handbook*. Boca Raton: CRC Press, 2014.
- [19] L. Gan, N. Li, U. Topcu and S. H. Low, "Exact Convex Relaxation of Optimal Power Flow in Radial Networks," *IEEE Transactions on Automatic Control*, vol. 60, no. 1, pp. 72-87, Jan. 2015.
- [20] H. Zhu and H. J. Liu, "Fast Local Voltage Control Under Limited Reactive Power: Optimality and Stability Analysis," *IEEE Transactions on Power Systems*, vol. 31, no. 5, pp. 3794-3803, Sept. 2016.
- [21] J. Yang, N. Zhang, C. Kang and Q. Xia, "A State-Independent Linear Power Flow Model with Accurate Estimation of Voltage Magnitude," *IEEE Transactions on Power Systems*, vol. 32, no. 5, pp. 3607-3617, Sept. 2017.
- [22] H. Yuan, F. Li, Y. Wei and J. Zhu, "Novel Linearized Power Flow and Linearized OPF Models for Active Distribution Networks with Application in Distribution LMP," *IEEE Transactions on Smart Grid*, vol. 9, no. 1, pp. 438-448, Jan. 2018.
- [23] "Impact of IEEE 1547 Standard on Smart Inverters," IEEE PES Industry Technical Support Task Force, Tech. Rep. PES-TR0067, May 2018.

- [24] J. Rocabert, A. Luna, F. Blaabjerg and P. Rodríguez, "Control of Power Converters in AC Microgrids," *IEEE Transactions on Power Electronics*, vol. 27, no. 11, pp. 4734-4749, Nov. 2012.
- [25] Q. Long, et al, "Community Microgrid Controller Evaluation using Hardware-in-the-Loop Testbed," in *2018 North American Power Symposium (NAPS)*, Fargo, ND, 2018.
- [26] R. Esmaili, L. Xu and D. K. Nichols, "A New Control Method of Permanent Magnet Generator for Maximum Power Tracking in Wind Turbine Application," in *IEEE Power Engineering Society General Meeting*, San Francisco, CA, 2005.
- [27] Xinyang Zhou, et al. "Reverse and Forward Engineering of Local Voltage Control in Distribution Networks." arXiv preprint arXiv:1801.02015, 2018.
- [28] A. Singhal, V. Ajjarapu, J. C. Fuller and J. Hansen, "Real-Time Local Volt/VAR Control Under External Disturbances with High PV Penetration," *IEEE Transactions on Smart Grid*, in press.
- [29] J. M. Guerrero, J. C. Vasquez, J. Matas, L. G. de Vicuna and M. Castilla, "Hierarchical Control of Droop-Controlled AC and DC Microgrids—A General Approach Toward Standardization," *IEEE Transactions on Industrial Electronics*, vol. 58, no. 1, pp. 158-172, Jan. 2011.
- [30] *IEEE Standard for the Specification of Microgrid Controllers*. IEEE Std 2030.7-2017, April 2018.
- [31] Advanced Distribution Management Solutions (ADMS). GE Power. Available: <https://www.ge.com/power/software/advanced-distribution-management-solutions>.
[Accessed: Oct. 5, 2018]

- [32] ABB Ability Network Manager ADMS - Network Management. Available: <https://new.abb.com/network-management/network-management/network-manager-adms>. [Accessed: Oct. 5, 2018]
- [33] Jianhui Wang, "Foundational Report Series: Advanced Distribution Management Systems for Grid Modernization," Argonne National Laboratories, Argonne, IL, Tech. Rep. ANL/ESD-15/17, Sep. 2015.
- [34] A. Elmitwally and M. Rashed, "Flexible Operation Strategy for an Isolated PV-Diesel Microgrid Without Energy Storage," *IEEE Transactions on Energy Conversion*, vol. 26, no. 1, pp. 235-244, March 2011.
- [35] J. Sachs and O. Sawodny, "A Two-Stage Model Predictive Control Strategy for Economic Diesel-PV-Battery Island Microgrid Operation in Rural Areas," *IEEE Transactions on Sustainable Energy*, vol. 7, no. 3, pp. 903-913, July 2016.
- [36] G. S. Stavrakakis and G. N. Kariniotakis, "A General Simulation Algorithm for the Accurate Assessment of Isolated Diesel-wind Turbines Systems Interaction. I. A General Multimachine Power System Model," *IEEE Transactions on Energy Conversion*, vol. 10, no. 3, pp. 577-583, Sept. 1995.
- [37] V. Friedel, "Modeling and Simulation of a Hybrid Wind-diesel Microgrid," M.S. Thesis, School of Electrical Engineering, Royal Institute of Technology, Stockholm, Sweden, 2009.
- [38] Z. Miao, A. Domijan and L. Fan, "Investigation of Microgrids with Both Inverter Interfaced and Direct AC-Connected Distributed Energy Resources," *IEEE Transactions on Power Delivery*, vol. 26, no. 3, pp. 1634-1642, July 2011.

- [39] A. S. Vijay, S. Doolla and M. C. Chandorkar, "Real-Time Testing Approaches for Microgrids," *IEEE Journal of Emerging and Selected Topics in Power Electronics*, vol. 5, no. 3, pp. 1356-1376, Sept. 2017.
- [40] R. O. Salcedo, et al., "Development of a Real-time Hardware-in-the-Loop Power Systems Simulation Platform to Evaluate Commercial Microgrid Controllers," Massachusetts Institute of Technology Lincoln Lab, Lexington, MA, Tech. Rep. TR-1203, Feb. 2016.
- [41] A. F. Hoke, A. Nelson, S. Chakraborty, F. Bell and M. McCarty, "An Islanding Detection Test Platform for Multi-Inverter Islands Using Power HIL," *IEEE Transactions on Industrial Electronics*, vol. 65, no. 10, pp. 7944-7953, Oct. 2018.
- [42] M. Asmine et al., "Model Validation for Wind Turbine Generator Models," *IEEE Transactions on Power Systems*, vol. 26, no. 3, pp. 1769-1782, Aug. 2011.
- [43] F. P. De Mello and L. H. Hannett, "Validation of Synchronous Machine Models and Derivation of Model Parameters from Tests," *IEEE Transactions on Power Apparatus and Systems*, vol. PAS-100, no. 2, pp. 662-672, Feb. 1981.
- [44] J. C. Agee and G. K. Girgis, "Validation of Mechanical Governor Performance and Models using an Improved System for Driving Ballhead Motors," *IEEE Transactions on Energy Conversion*, vol. 10, no. 1, pp. 156-161, March 1995.
- [45] L. Hajagos et al., "Guidelines for Generator Stability Model Validation Testing," in *2007 IEEE Power Engineering Society General Meeting*, Tampa, FL, 2007.
- [46] P. Pourbeik, R. Rhinier, S. Hsu, B. Agrawal and R. Bisbee, "Semiautomated Model Validation of Power Plant Equipment Using Online Measurements," *IEEE Transactions on Energy Conversion*, vol. 28, no. 2, pp. 308-316, June 2013.

- [47] P. Pourbeik, "Automated Parameter Derivation for Power Plant Models from System Disturbance Data," in *2009 IEEE Power and Energy Society General Meeting*, Calgary, AB, 2009.
- [48] A. Menon et al., "Towards a Commercial-grade Tool for Disturbance-based Model Validation and Calibration," in *2018 IEEE Power and Energy Society General Meeting, Portland, OR, 2018*.
- [49] W. Chen, Q. Gong, L. Zhang and M. Yang, "Parameters Identification of Twelve-phase Synchronous Generator based on Levenberg-Marquardt Algorithm," in *2008 International Conference on Electrical Machines and Systems*, Wuhan, 2008.
- [50] L. Wu, Z. Chen, C. Long, S. Cheng, P. Lin, Y. Chen, and H. Chen, "Parameter Extraction of Photovoltaic Models from Measured I-V Characteristics Curves using a Hybrid Trust-Region Reflective Algorithm," *Applied Energy*, vol. 232, pp. 36-53, Dec. 2018.
- [51] T. Hosseinalizadeh, S. M. Salamati, S. A. Salamati and G. B. Gharehpetian, "Improvement of Identification Procedure Using Hybrid Cuckoo Search Algorithm for Turbine-Governor and Excitation System," *IEEE Transactions on Energy Conversion*, vol. 34, no. 2, pp. 585-593, June 2019.
- [52] Z. Liu, H. Wei, Q. Zhong, K. Liu, X. Xiao and L. Wu, "Parameter Estimation for VSI-Fed PMSM Based on a Dynamic PSO With Learning Strategies," *IEEE Transactions on Power Electronics*, vol. 32, no. 4, pp. 3154-3165, April 2017.
- [53] F. Xie, H. Yu, Q. Long, W. Zeng and N. Lu, "Battery Model Parameterization using Manufacturer Datasheet and Field Measurement for Real-time HIL Applications," *IEEE Transactions on Smart Grid*.

- [54] M. Torres and L. A. C. Lopes, "Inverter-based Diesel Generator Emulator for the Study of Frequency Variations in a Laboratory-scale Autonomous Power System," *Energy and Power Engineering*, vol. 5, no. 3, pp. 274-283, May 2013.
- [55] P. W. Sauer and M. A. Pai. *Power System Dynamics and Stability*. Upper Saddle River, NJ: Prentice Hall, 1998.
- [56] R. V Jategaonkar. *Flight Vehicle System Identification: A Time-domain Methodology*. American Institute of Aeronautics and Astronautics, Inc., 2015.
- [57] M. Gevers, A. S. Bazanella, X. Bombois and L. Miskovic, "Identification and the Information Matrix: How to Get Just Sufficiently Rich?," *IEEE Transactions on Automatic Control*, vol. 54, no. 12, pp. 2828-2840, Dec. 2009.
- [58] J. Nocedal and S. Wright. *Numerical Optimization*. Springer Science & Business Media, 2006.
- [59] S. K. Park, "A Transformation Method for Constrained-Function Minimization," Langley Research Center, Hampton, VA, NASA TN D-7983, Nov. 1975.
- [60] J. C. Vasquez, R. A. Mastromauro, J. M. Guerrero and M. Liserre, "Voltage Support Provided by a Droop-Controlled Multifunctional Inverter," *IEEE Transactions on Industrial Electronics*, vol. 56, no. 11, pp. 4510-4519, Nov. 2009.
- [61] Y. Lee, J. Jiang, H. Su, Y. Ho and Y. Chang, "Ancillary Voltage Control for a Distribution Feeder by Using Energy Storage System in Microgrid," in *2016 IEEE 7th International Symposium on Power Electronics for Distributed Generation Systems (PEDG)*, Vancouver, BC, 2016.

- [62] Y. Wang, K. T. Tan, X. Y. Peng and P. L. So, "Coordinated Control of Distributed Energy-Storage Systems for Voltage Regulation in Distribution Networks," *IEEE Transactions on Power Delivery*, vol. 31, no. 3, pp. 1132-1141, June 2016.
- [63] D. Chen, Y. Xu and A. Q. Huang, "Integration of DC Microgrids as Virtual Synchronous Machines into the AC Grid," *IEEE Transactions on Industrial Electronics*, vol. 64, no. 9, pp. 7455-7466, Sept. 2017.
- [64] J. W. Simpson-Porco, Q. Shafiee, F. Dörfler, J. C. Vasquez, J. M. Guerrero and F. Bullo, "Secondary Frequency and Voltage Control of Islanded Microgrids via Distributed Averaging," *IEEE Transactions on Industrial Electronics*, vol. 62, no. 11, pp. 7025-7038, Nov. 2015.
- [65] R. Olfati-Saber and R. M. Murray, "Consensus Problems in Networks of Agents With Switching Topology and Time-Delays," *IEEE Transactions on Automatic Control*, vol. 49, no. 9, pp. 1520-1533, Sept. 2004.
- [66] J. He and Y. W. Li, "Analysis, Design, and Implementation of Virtual Impedance for Power Electronics Interfaced Distributed Generation," *IEEE Transactions on Industry Applications*, vol. 47, no. 6, pp. 2525-2538, Nov.-Dec. 2011.
- [67] A. Bidram, A. Davoudi, F. L. Lewis and Z. Qu, "Secondary Control of Microgrids based on Distributed Cooperative Control of Multi-agent systems," *IET Generation, Transmission & Distribution*, vol. 7, no. 8, pp. 822-831, Aug. 2013.
- [68] D. B. Arnold, M. Sankur, R. Dobbe, K. Brady, D. S. Callaway and A. Von Meier, "Optimal Dispatch of Reactive Power for Voltage Regulation and Balancing in Unbalanced Distribution Systems," in *2016 IEEE Power and Energy Society General Meeting (PESGM)*, Boston, MA, 2016.

- [69] M. Farivar, R. Neal, C. Clarke and S. Low, "Optimal Inverter VAR Control in Distribution Systems with High PV Penetration," in *2012 IEEE Power and Energy Society General Meeting*, San Diego, CA, 2012.
- [70] W. Zheng, W. Wu, B. Zhang and Y. Wang, "Robust Reactive Power Optimization and Voltage Control Method for Active Distribution Networks via Dual Time-Scale Coordination," *IET Generation, Transmission & Distribution*, vol. 11, no. 6, pp. 1461-1471, April 2017.
- [71] M. E. Baran and F. F. Wu, "Optimal Capacitor Placement on Radial Distribution Systems," *IEEE Transactions on Power Delivery*, vol. 4, no. 1, pp. 725-734, Jan. 1989.
- [72] "Rule 21 Interconnection," RPS Program Overview. [Online]. Available: <http://www.cpuc.ca.gov/Rule21/>.
- [73] "Hawaiian Electric Rules," Hawaiian Electric, Maui Electric, Hawaii Electric Light. [Online]. Available: <https://www.hawaiianelectric.com/billing-and-payment/rates-and-regulations/hawaiian-electric-rules>.
- [74] ABB Schweiz AG. X. Feng, N. Kang, "Hierarchical Robust Model Predictive Voltage and Var Control with Coordination and Optimization of Autonomous DER Voltage Control," US Patent-2017/0133849-A1, 2017.
- [75] J. Zhao et al., "Local Voltage Control Strategy of Active Distribution Network with PV Reactive Power Optimization," in *2017 IEEE Power & Energy Society General Meeting*, Chicago, IL, 2017.
- [76] X. Zhu et al., "Voltage-load Sensitivity Matrix based Demand Response for Voltage Control in High Solar Penetration Distribution Feeders," in *2017 IEEE Power & Energy Society General Meeting (PESGM)*, Chicago, IL, 2017.

- [77] Palacios-Gomez, F., L. Lasdon, and M. Engquist, "Nonlinear optimization by successive linear programming," *Management Science*, vol. 28, no. 10, pp. 1106-1120, Oct. 1982.
- [78] T. Hong, D. Zhao, Y. Zhang, B. Cui, and Y. Tian, "Optimal Voltage Reference for Droop-based DERs in Distribution Systems," *IEEE Transactions on Smart Grid*, pp. 1-1, 2019.
- [79] H. Ji, C. Wang, P. Li, J. Zhao, G. Song, F. Ding, and J. Wu, "A Centralized-based Method to Determine the Local Voltage Control Strategies of Distributed Generator Operation in Active Distribution Networks," *Applied Energy*, vol. 228, pp. 2024 – 2036, 2018.
- [80] G. C. Kryptonidis, E. O. Kontis, A. I. Chrysochos, C. S. Demoulias and G. K. Papagiannis, "A Coordinated Droop Control Strategy for Overvoltage Mitigation in Active Distribution Networks," *IEEE Transactions on Smart Grid*, vol. 9, no. 5, pp. 5260-5270, Sept. 2018.
- [81] T. Niknam, M. Zare, and J. Aghaei, "Scenario-based Multiobjective Volt/Var control in Distribution Networks Including Renewable Energy Sources," *IEEE Transactions on Power Delivery*, vol. 27, no. 4, pp. 2004–2019, Oct 2012.
- [82] A. Alkuhayli and I. Husain, "Two-level Volt/Var Control Strategy in Distribution Networks with Intermittent Renewables," in *2018 IEEE Power Energy Society General Meeting (PESGM)*, Aug 2018, pp. 1–5.
- [83] Y. P. Agalgaonkar, B. C. Pal, and R. A. Jabr, "Stochastic Distribution System Operation Considering Voltage Regulation Risks in the Presence of PV Generation," *IEEE Transactions on Sustainable Energy*, vol. 6, no. 4, pp. 1315–1324, Oct 2015.

- [84] F. U. Nazir, B. C. Pal, and R. A. Jabr, "A Two-Stage Chance Constrained Volt/Var Control Scheme for Active Distribution Networks with Nodal Power Uncertainties," *IEEE Transactions on Power Systems*, vol. 34, no. 1, pp. 314–325, Jan 2019.
- [85] "Distributed PV Monitoring and Feeder Analysis," EPRI. [Online]. Available: https://dpv.epri.com/measurement_data.html.
- [86] J. M. Morales, S. Pineda, A. J. Conejo, and M. Carrion, "Scenario Reduction for Futures Market Trading in Electricity Markets," *IEEE Transactions on Power Systems*, vol. 24, no. 2, pp. 878–888, May 2009.
- [87] L. Wu, M. Shahidehpour, and T. Li, "Stochastic Security-Constrained Unit Commitment," *IEEE Transactions on Power Systems*, vol. 22, no. 2, pp. 800–811, May 2007.
- [88] Q. Long, J. Wang, D. Lubkeman, N. Lu, and P. Chen, "Volt-Var Optimization of Distribution Systems for Coordinating Utility Voltage Control with Smart Inverters," in *2019 IEEE Power Energy Society Innovative Smart Grid Technologies Conference (ISGT)*, Feb 2019, pp. 1–5.
- [89] J. R. Birge and F. Louveaux, *Introduction to Stochastic Programming*. Springer Science & Business Media, 2011.
- [90] J.-P. Watson, D. L. Woodruff, and W. E. Hart, "PySP: Modeling and Solving Stochastic Programs in Python," *Mathematical Programming Computation*, vol. 4, no. 2, pp. 109–149, 2012.